

Mastering the statistical properties of microcavity polaritons

THÈSE N° 7991 (2017)

PRÉSENTÉE LE 21 SEPTEMBRE 2017
À LA FACULTÉ DES SCIENCES DE BASE
LABORATOIRE D'OPTOÉLECTRONIQUE QUANTIQUE
PROGRAMME DOCTORAL EN PHYSIQUE

ÉCOLE POLYTECHNIQUE FÉDÉRALE DE LAUSANNE

POUR L'OBTENTION DU GRADE DE DOCTEUR ÈS SCIENCES

PAR

Albert ADIYATULLIN

acceptée sur proposition du jury:

Prof. M. Grioni, président du jury
Prof. B. Deveaud, Dr M. Portella Oberli, directeurs de thèse
Prof. A. Bramati, rapporteur
Prof. M. Bayer, rapporteur
Prof. V. Savona, rapporteur



ÉCOLE POLYTECHNIQUE
FÉDÉRALE DE LAUSANNE

Suisse
2017

Abstract

Microcavity polaritons are hybrid quasiparticles emerging from the strong coupling between quantum well excitons and light in the resonator. Their unique half-light half-matter nature brings in specific properties like low effective mass, nonlinearity due to the repulsive interactions, and ability to directly access the polaritonic wavefunction through optical means. Due to their specific features, polaritons can form macroscopic quantum states and even undergo Bose-Einstein condensation, which makes them very interesting system for studying the quantum phenomena occurring on a macroscopic scale.

This thesis is devoted to the investigation of dynamics of the second-order coherence of the microcavity polaritons. The evolution of the coherence of the polariton system occurs on a timescale of few picoseconds only, which required assembly of a new ultrafast photon correlation setup based on the streak-camera. The operation of this setup and requirements for high-quality measurements are discussed in details. After this, the experiments under both nonresonant and resonant excitation of polaritons are reported.

Under nonresonant excitation, the formation of the polariton Bose-Einstein condensate is observed, and the change of the polariton coherence during this phase transition is measured. This indicates the time which is required to form the condensate, and also allows to estimate its propagation velocity. The latter is compared with the measurements of the first-order spatial correlation function.

Finally, polaritons confined in two coupled potential traps are studied. The traps are fabricated using the wet etching of the microcavity. In the resulting Josephson junction, polaritons are excited resonantly and demonstrate clear Josephson oscillations between the two traps. At the same time, the correlation measurements demonstrate strong perturbations of the light statistics in phase with the oscillations. This behavior is well represented with the quantum simulations, which also indicate presence of a significant quadrature squeezing in the system. The origin of the squeezing, the perspective for generating the nonclassical light, and other

features of this phenomenon are discussed.

Key words: light-matter interaction, strong coupling, photons, excitons, exciton-polaritons, coherence, photon statistics, second-order correlation, Bose-Einstein condensation, non-linearity, bosonic Josephson junction, Josephson oscillations, quantum optics, quadrature squeezing



Résumé

Les polaritons de microcavité sont quasi-particules hybrides qui résultant du couplage fort entre les excitons d'un puits quantique et la lumière confinée dans le résonateur. Leur origine unique, mi-lumière mi-matière, permet des caractéristiques spécifiques : une faible masse effective, en même temps qu'une nonlinéarité non négligeable grâce aux interactions répulsives, et enfin la possibilité d'accès à la fonction d'onde polaritonique par des moyens optiques simples. Grâce à leurs caractéristiques spécifiques, les polaritons peuvent produire des états quantiques macroscopiques, comme par exemple démontrer la condensation de Bose-Einstein. Ils sont donc un système très intéressant pour étudier les phénomènes quantiques dans des dimensions macroscopiques.

La présente thèse est dédiée à l'étude de cohérence de deuxième ordre des polaritons. La dynamique de cette cohérence des polaritons se produit sur des intervalles temporels de quelques picosecondes. Nous avons donc besoin d'une expérience ultrarapide pour la mesure des corrélations des polaritons, qui se base sur l'utilisation d'une camera à balayage de fente. Le fonctionnement de cette expérience ainsi que les conditions pour une qualité optimale des mesures sont discutés de manière très détaillée. Ensuite, sont rapportées des expériences sous excitation non-résonante ainsi que sous excitation résonante.

Sous excitation non-résonante, la création d'un condensat de Bose-Einstein est observée, et les changements de la cohérence polaritonique pendant cette transition sont mesurés. Ceci nous permet de déduire le temps de formation du condensat, et, en même temps, quelle est sa vitesse de la propagation. Cette vitesse est comparée avec des mesures de cohérence spatiale du premier ordre.

Enfin, les polaritons confinés dans deux puits de potentiel sont étudiés. Ces pièges ont fabriqués par attaque chimique de la microcavité. Dans la jonction Josephson formée par le couplage des deux pièges, les polaritons sont excités de manière résonante et subissent des oscillations de Josephson entre les deux pièges. En même temps, les mesures des corrélations

démontrent des perturbations fortes de la statistique des photons, en phase avec les oscillations. Ce comportement est bien reproduit par des simulations quantiques, qui peuvent aussi confirmer la présence de squeezing dynamique dans le système. L'origine du squeezing, les perspectives pour la production d'états non-classiques, et les autres caractéristiques du phénomène sont discutés.

Mots clefs : interaction lumière-matière, couplage fort, photons, excitons, polaritons excitoniques, cohérence, statistique des photons, corrélation du deuxième ordre, condensation de Bose-Einstein, nonlinéarité, jonction Josephson bosonique, oscillations de Josephson, optique quantique, squeezing quadratique

Contents

Abstract/Résumé	i
Introduction	1
1 Microcavity polaritons	5
1.1 Excitons in bulk semiconductors	5
1.2 Excitons in quantum wells	8
1.3 Photons in a microcavity	8
1.4 Strong light-matter coupling	11
1.5 Bose-Einstein condensation	14
1.5.1 Nonresonant excitation	15
1.5.2 Resonant excitation	18
1.5.3 Conclusion	18
2 Concepts of quantum optics	21
2.1 Statistics of photocounts	21
2.2 Field quantization	23
2.3 Examples of the light field states	26
2.4 Field correlation functions	31
2.5 Generation of nonclassical light	35
2.6 Second-order correlations of the squeezed coherent state	38
2.7 Conclusion	39
3 Sample fabrication and experimental techniques	41
3.1 Microcavity samples	41
3.1.1 CdTe microcavity	43
3.1.2 InGaAs microcavities	44
3.1.3 Mesa fabrication	45

Contents

3.2	Experimental techniques	50
3.2.1	General excitation and detection scheme	50
3.2.2	Spectral and temporal tomography	52
3.2.3	Interferometry	53
3.2.4	Interferometer stabilization and phase tomography	55
4	Ultrafast second-order correlation measurements	59
4.1	Overview	59
4.2	Ultrafast second-order correlation measurements	61
4.3	Data acquisition	64
4.4	Data processing	66
4.5	Conclusion	68
5	Formation of a polariton BEC	69
5.1	Overview	69
5.2	Spontaneous Bose-Einstein condensation of polaritons	71
5.3	Zero-delay second-order correlation measurements	74
5.4	Comparison with the first-order spatial coherence	77
5.5	Nonzero-delay second-order correlation measurements	80
5.6	Conclusion	82
6	Periodic squeezing in a polariton Josephson junction	85
6.1	Overview	86
6.2	Bosonic Josephson junction in a nutshell	87
6.2.1	Two-mode approximation	87
6.2.2	Mean-field model	88
6.3	Polariton Josephson junction	91
6.4	Second-order correlation measurements	94
6.5	Theoretical description	97
6.6	Discussion	99
6.6.1	Origin of the polariton squeezing	99
6.6.2	Effect of the system occupancy on the polariton statistics	102
6.6.3	Effect of the streak-camera resolution	105
6.6.4	Repeatability of the experiment	106
6.6.5	Two-dimensional correlation map	108
6.7	Conclusion	109

7 Perspectives	111
7.1 Unconventional photon blockade	111
7.2 Correlation measurements in other geometries	113
7.3 Photon blockade with polaritons	114
Bibliography	129
Acknowledgements	131
Curriculum Vitae	133



Introduction

The interactions between light and matter have always been of a high interest for physicists. The reason for this was not only a general curiosity or practical applications. The fundamental laws of conservation of energy or momentum allowed to unveil the features of one of the interacting entities by carefully measuring the parameters of the second one. This led to such bright discoveries like direct measurements of the momentum of light [1] or observation of the photoelectric effect [2]. Non-thermal light emission from semiconductor materials, namely silicon carbide, was first observed years before the quantum theory of semiconductors was invented [3, 4]. The development of the band theory of crystals led to deep understanding of the properties of semiconductors and realization of the nature of their luminescence. This opened the road towards an extensive research and gave rise to new fabrication techniques of semiconductors, thus revolutionizing the world and leading to the emergence of miniaturized electronics and light emitting devices covering an ultrabroad spectral range from near ultraviolet to terahertz region.

The light-matter interaction in semiconductors can be further increased if the electric dipole is coupled only to the light modes with an appropriate energy by, for instance, embedding the dipole into a matched resonator [5]. This regime of *weak coupling* leads to noticeable increase of the intensity of dipole luminescence, and nowadays is routinely used in cavity quantum electrodynamics [6]. If the light-matter interaction strength is increased even more, it does not simply change the emission rate, but renormalizes the light and dipole energy states, leading to the formation of the new mixed light-matter states of the system called *exciton-polaritons*. This *strong coupling* regime was first predicted by J. Hopfield in 1958 [7], and observed only three decades later by C. Weisbuch and coworkers in semiconductor microcavities [8]. The intrinsic light-matter nature of microcavity polaritons turned out to be extremely favorable for the research in term of their low effective mass, high mobility, controllable interactions, and last but not least, ability to easily address the polaritons by standard optical means.

The low effective mass of polaritons is determinant for their very large de Broglie wavelength, which allows them to form a macroscopic quantum state. Together with intrinsic interactions present in the system this finally made it possible to demonstrate that polaritons can undergo spontaneous Bose-Einstein condensation [9]. Since that seminal publication, the research on polaritons led to the observation of numerous quantum phenomena like superfluidity [10], emergence of the topological defects [11, 12], solitons [13], and Bogoliubov dispersion branches [14]. The polariton physics was even further enriched by introducing the means to prevent the polariton in-plane motion by confining them into artificial potentials [15, 16, 17, 18]. First of all, this allowed for the studies of zero- and one-dimensional polaritons, as well as their propagation along the one-dimensional system. Next, tunnel coupling of artificial traps gave rise to bright research first, on photonic molecules [19], and next, on two-dimensional lattices [20], thus opening the way to the simulations of the Hamiltonians [21] and studies on topologically protected states in lattices [22].

In the last few years, an interest arose to studies of the quantum optical properties of polaritons. Indeed, few theoretical works were covering this topic, proposing storage of quantum information [23], or generating nonclassical light from the polaritonic system [24]. From the experimental side, two measurements of the quadrature squeezed light emitted from the microcavity were reported [25, 26]. However, even during the last decade, the precise measurements of the photon statistics were not realizable because the time resolution of the single photon avalanche detectors (~ 100 ps) was much longer than the characteristic time of polariton dynamics (~ 10 ps). This limitation was overcome by introducing the ultrafast photon correlation measurements, the technique that became available thanks to the streak-camera working in a single photon counting mode [27]. The use of this technique led to observations of the photon statistics below and above the polariton condensation threshold [28], studies of the polariton interactions [29], and precession of polarizations in the polariton condensate [30].

This thesis addresses the fundamental properties of polaritons, which regard particularly to their quantum statistics and quantum features of the microcavity field. This is done by studying their second-order coherence by performing ultrafast photon correlation measurements. The manuscript is organized as follows.

First of all, in Chapter 1, the basic concepts of the light-matter interaction are presented. The excitons in semiconductor quantum wells are introduced, and their coupling to the light field in the planar microcavity is described. The properties of microcavity exciton-polaritons,

including physical aspects of their Bose-Einstein condensation, are discussed.

Chapter 2 is devoted to basic concepts of quantum optics. Here, the procedure of quantization of the light field is provided. Several bright examples of the light field states are described in the framework of quantum mechanics. Few ways of generation of different states of light are shortly discussed. Last but not least, the field correlation functions and the experimental techniques for their measurements are introduced.

In Chapter 3 we present the microcavity samples used during this thesis work, and the way in which the potential traps for the polaritons were fabricated. The experimental layout used for optical excitation and detection of the luminescence of the microcavities is also discussed.

Chapter 4 describes the setup assembled for the ultrafast second-order correlation measurements. The use of the streak-camera as a single photon detector, and the improvements required for the reliable and repeatable correlation measurements are discussed. We also describe an original way of acquiring and processing the experimental data.

In Chapter 5, we perform the first- and second-order coherence measurements of the microcavity emission during the spontaneous formation of a polariton Bose-Einstein condensate. The aspects of the dynamics of the condensation process are analyzed. Particularly, we evidence how the thermal statistics of noncondensed polaritons is replaced with a coherent one when the Bose-Einstein condensate is formed. The formation of a large condensate is studied through both second-order temporal coherence and first-order spatial coherence measurements, which allows to access the propagation speed of the condensed polaritons.

Chapter 6 covers the major topic of this thesis work, the measurements of the light statistics in the system of two coupled polaritonic modes. For this, two trapping potentials are fabricated close to each other, thus allowing for a tunnel coupling between them and realizing a polariton Josephson junction. The dynamical Josephson oscillations of polaritons between two modes are accessed, and the results of the measurements are compared with a mean-field theoretical model as well as with previous measurements in similar layouts. Next, the second-order correlation function is measured, and strong change of the light statistics occurring in phase with the Josephson oscillations is unveiled. The measurements are found to strikingly agree with the theoretical simulations performed at a quantum level, which also evidence strong quadrature squeezing of the polariton field. The physics of these observations is analyzed in detail.

Contents

Chapter 7 provides the perspectives of measurements of nonclassical phenomena in polaritonic systems. Some of the results and proposals discussed in the field of polariton physics are reviewed. We also propose several ideas for future experiments, which naturally follow the work reported in this thesis.

1 Microcavity polaritons

In this Chapter, we will give a theoretical background required for understanding of the light-matter interaction in semiconductors. More specifically, this overview will be focused on the excitons in bulk and two-dimensional semiconductors as the elementary matter excitations, and their strong coupling to the light field confined in the microcavity. As a result, new hybrid quasiparticles appear in the system which are called *exciton-polaritons* and inherit particular properties from both their light and matter components. Particularly, their characteristic dispersion features and bosonic statistics favor realization of macroscopic quantum states formed by polariton ensembles, and Bose-Einstein condensation of polaritons.

1.1 Excitons in bulk semiconductors

The term *semiconductors* describes a wide range of materials, the properties of which are lying in between of those of metals and dielectrics. In crystalline semiconductors, the translation symmetry leads to formation of the valence and conduction band with an energy separation E_g , the *band gap*, having a value up to few electronvolts [31]. At zero temperature, all states in the valence band are occupied, and the conduction band is empty. Given a certain amount of energy, an electron from the valence band can be excited to the conduction band. This can for instance occur if a photon with an energy $h\nu \geq E_g$ is *absorbed* in the semiconductor, and its energy is given to the electron. This process also leads to an appearance of an empty state in the valence band, that can allow another valence band electron to move and occupy this empty state. This can be effectively described by motion of the vacant space by itself across the crystal, which in this situation is referred to as a *hole* motion. The hole is therefore a semiconductor quasiparticle that possesses a positive charge. Parabolicity of the dispersion bands near their

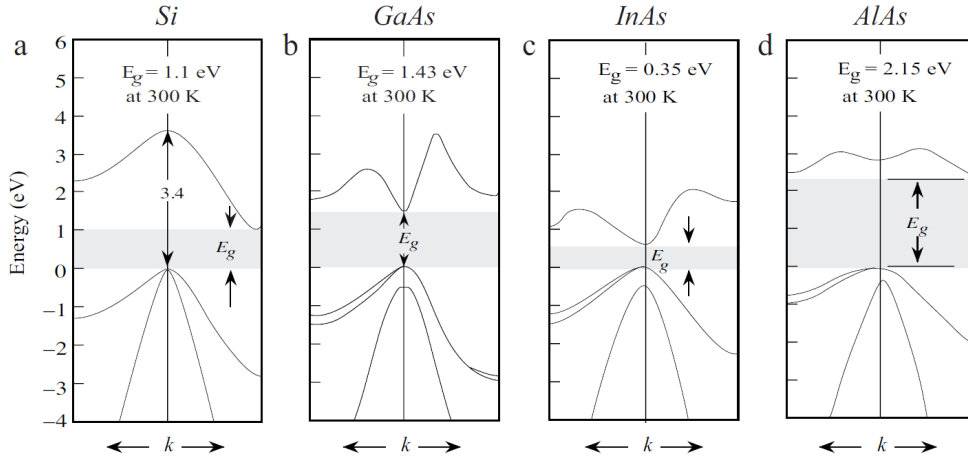


Figure 1.1: The electronic band structures of (a) Si, (b) GaAs, (c) InAs, and (d) AlAs around the Γ -point. GaAs and InAs are prime examples of direct bandgap semiconductors, whereas Si and AlAs have an indirect bandgap. Reproduced from [32].

extrema allows to associate an effective mass with the electrons in the conduction band m_e , and the valence band holes m_h .

A process opposite to the absorption is *emission* or *luminescence*, in which the electron relaxes from the conduction band to the valence band, and its energy is given to the emitted quantum of light. This process can also be considered as a *recombination* of the conduction band electron and valence band hole, in which both particles annihilate and emit a photon. Given the very small wave vector of the optical photons, which are much less than the characteristic values for the electrons, both absorption and emission can only take place if the electron momentum does not change during the recombination or absorption. Therefore the efficient luminescence is allowed only for the semiconductors with a *direct bandgap*, where both the top of the valence band and the bottom of the conduction band have the same wavevector. The opposite case occurs when the two extrema do not share the same wavevector, and is referred to as an *indirect bandgap*. The weak luminescence in this case is due to the fact that it requires the third particle – a phonon – to carry the excess momentum, thus reducing the probability of this decay channel. This leads to trapping of the electrons on the bottom of the conduction band, and very low efficiency of luminescence. Examples of semiconductors with direct and indirect bandgaps are presented in Figure 1.1.

The spectrum of the semiconductors is not limited by the transitions between the valence and conduction bands. The Coulomb interaction between an electron and a hole leads to the formation of a new quasiparticle, called an *exciton*. The energy of such a bound state is

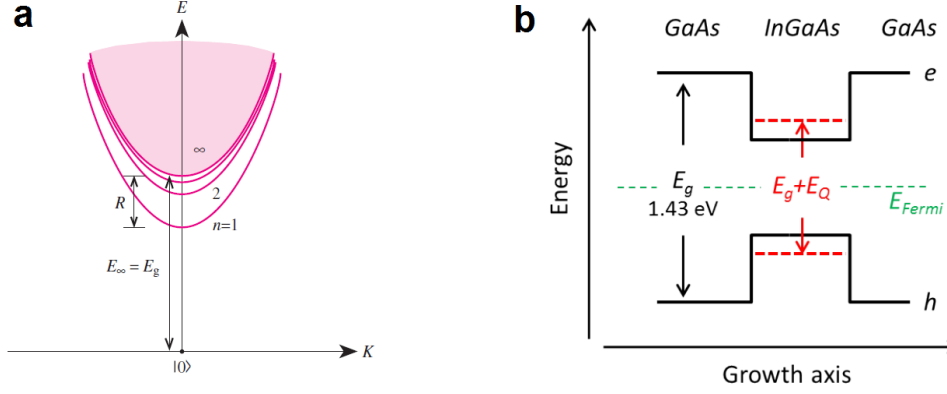


Figure 1.2: (a) The energy spectrum of an exciton showing the energy levels with $n = 1, 2, 3$ and the continuum states. Reproduced from [31]. (b) Confinement of the charge carriers in semiconductor quantum well along the growth axis. Reproduced from [34].

lower than E_g , and therefore should give rise to spectral features in the forbidden bandgap region. In fact, the excitons have the properties very similar to ones of the hydrogen atom. Particularly, excitons possess a quantized hydrogen-like spectrum [31] with the energy levels defined by the mass of the particles and Bohr radius:

$$E_X(\mathbf{K}) = E_g - \frac{1}{n^2}E_b + \frac{\hbar^2 \mathbf{K}^2}{2M_X} \quad (1.1)$$

where E_b is the exciton binding energy, $M_X = m_e + m_h$ is the effective mass of the exciton as a composite particle, \mathbf{K} is the wavevector defined for the center of mass, and n is the number of the energy level, which in particular cases [33] can exceed 20. Here the third term considers the motion of an exciton as a whole, whereas the exciton binding energy in the second term is defined by the relative motion of the electron and the hole:

$$E_b = \frac{\mu R_H}{m_e \epsilon^2} \quad (1.2)$$

with $\mu = m_e m_h / (m_e + m_h)$ being the exciton effective mass, and $R_H = 13.6$ eV the Rydberg constant for the hydrogen atom. An exciton possesses a parabolic dispersion for each of its quantized energy levels, as shown in Figure 1.2a.

1.2 Excitons in quantum wells

In the previous section the excitons in bulk semiconductors were considered. However, if the lateral size of the semiconducting material is decreased along one direction so that it gets comparable to the size of the excitonic wavefunction, we reach the case of the *quantum well*. Consequently, the excitonic energy gets quantized due to the localization of the excitonic motion along one direction. This brings in a quantization energy E_Q , which adds up to the bandgap energy (Figure 1.2b). For an ideal quantum well, the resulting dispersion reads [35]

$$E_X^{2D}(\mathbf{K}_{\parallel}) = E_g + E_Q - \frac{1}{(n - \frac{1}{2})^2} E_b + \frac{\hbar^2 \mathbf{K}_{\parallel}^2}{2M_X} \quad (1.3)$$

with \mathbf{K}_{\parallel} being the in-plane momentum of the exciton. The effective binding energy of the exciton in the quantum well is increased by a factor of four in comparison to the bulk case, thus making the exciton more robust against external perturbations. Qualitatively this change represents the fact that the wavefunctions of an electron and a hole have a stronger overlap since they are more localized in space. Therefore, the excitons in quantum wells form a 2D system, where they are free to propagate in the plane of the quantum well, but are confined in the perpendicular direction.

The semiconductor quantum wells can be routinely fabricated by means of the epitaxial growth with an atomic-level precision. For this, a thin layer of a semiconductor with a bandgap E_{g1} (for instance InGaAs) is grown on top of a thick semiconductor with a larger bandgap $E_{g2} > E_{g1}$ (like GaAs), and then another semiconductor with bandgap E_{g2} is grown on the top of the structure (Figure 1.2b). This results in the formation of a 2D quantum well, where the charge carriers and excitons are confined in a thin layer along the growth direction. The localization also means that the particle wavevector along the growth direction is not a continuous variable anymore, but can only take certain values. Therefore, only the momentum in the plane of the quantum well is conserved.

1.3 Photons in a microcavity

The main idea lying behind confining light in a small area is reflecting it back when it tries to escape. The use of optical resonators allows for creation of well-defined modes of light with various properties [35]. Probably the simplest kind of such a resonator is a planar *Fabry-Perot cavity*, where two flat mirrors facing each other allow for a strong light confinement between

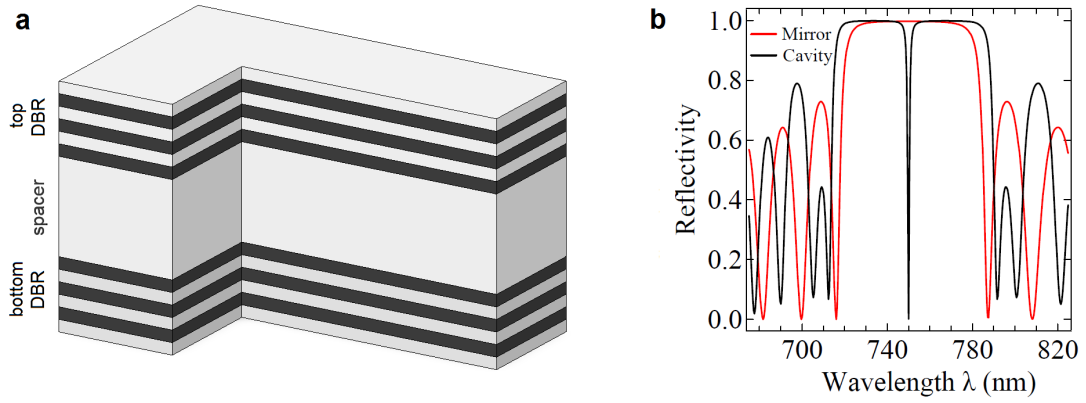


Figure 1.3: (a) Schematic image of a λ -microcavity formed by two DBRs. (b) Reflectivity of a single DBR with 32 pairs of layers (red), and a DBR cavity with DBRs containing 16 and 24 pairs, and a 2λ spacer in between. Represented from [Lag11].

them. The boundary condition that imposes the annulation of the electric field at the interface of the mirrors allows for a formation of standing waves of wavelengths given by

$$\lambda_c = \frac{2n_c L}{m}, \quad m = 1, 2, 3, \dots, \quad (1.4)$$

with n_c being the refractive index of the cavity. The maximal possible wavelength of the electromagnetic wave is therefore twice the length of the resonator.

In an idealized picture the light can be trapped in the resonator for an infinite time. In reality, the mirrors of the microresonator are never perfect, and the light can escape through them. To improve the photon lifetime, one can use high-quality multilayer mirrors, usually referred to as *distributed Bragg reflectors* (DBR). Such mirrors consist of a stack of two materials with two different refraction coefficients n_1 and n_2 , and its principle of operation relies on the destructive interference of light reflected from the interfaces between these materials. Particularly, this condition is met at the wavelength λ if the optical thickness of each layer is equal to $\lambda/4$. The absence of losses for the reflection together with using non-absorptive materials makes it possible to create mirrors with a reflectivity up to $R \approx 0.9999$. The high reflectivity is obtained for all the wavelengths within the *stopband* region centered at λ and having the bandwidth

$$\Delta\lambda = \frac{4\lambda}{\pi} \arcsin\left(\frac{n_2 - n_1}{n_2 + n_1}\right). \quad (1.5)$$

The sketch of a microcavity formed by two DBRs is presented in Figure 1.3a. The reflectivity

of one single mirror, and the two mirrors forming the Fabry-Perot microcavity are shown in Figure 1.3b. For the cavity, a narrow *cavity mode* at $\lambda = 750$ nm appears, for which the resonator is transparent. Outside the stopband region, the reflectivity of the structure exhibits oscillations due to particular interference conditions in the DBRs, but show neither a good reflectivity nor transparency

The width of the cavity mode γ_c is related to the lifetime of the photon in the cavity τ_{ph} [36]:

$$\tau_{ph} = \frac{1}{2\pi\gamma_c}. \quad (1.6)$$

This holds for the high-quality cavities, in which no inhomogeneous broadening of the linewidth due to e.g. fluctuations of the spacer thickness is present. The *quality factor* of the cavity is conventionally defined as

$$Q = \frac{\nu_c}{\gamma_c}, \quad (1.7)$$

where $\nu_c = c/\lambda_c$ is the frequency of the cavity mode. The quality factor increases with the photon lifetime, and the higher it is, the more photons can be simultaneously trapped in the cavity, and the stronger light field can be obtained in the resonator.

Finally, we address the question of the effective mass of the photon in the cavity. The Fabry-Perot cavity confines the light only in the direction perpendicular to its optical axis, and therefore does not lead to the quantization of energy states in this direction. Therefore the wavevector of the photon in the plane parallel to the surface of the mirrors k_{\parallel} is conserved. The dispersion of the lowest energy mode can be found from the decomposition of the total wavevector \mathbf{k} of light into the components parallel and perpendicular to the mirror plane $\mathbf{k} = k_{\parallel}\mathbf{e}_{\parallel} + k_{\perp}\mathbf{e}_{\perp}$:

$$E(k_{\parallel}) = \frac{\hbar c}{n_c} \sqrt{k_{\perp}^2 + k_{\parallel}^2} = \frac{\hbar c}{n_c} k_{\perp} \sqrt{1 + \frac{k_{\parallel}^2}{k_{\perp}^2}} = E_0 + \frac{\hbar c k_{\parallel}^2}{2n_c k_{\perp}}. \quad (1.8)$$

The dispersion of the energy of the photons confined in the resonator is parabolic. By analogy with a kinetic energy expression $E = \frac{\hbar^2 k^2}{2m}$, we can attribute the effective mass to the photon:

$$m_{ph} = \frac{\hbar n_c^2}{2cL} = \frac{\hbar n_c^2}{c\lambda_c}. \quad (1.9)$$

This effective mass is several orders of magnitude lower than the free electron mass. Particu-

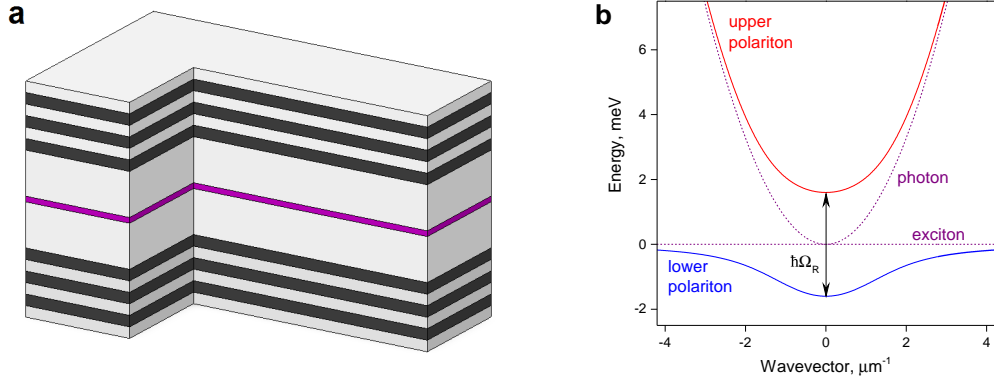


Figure 1.4: (a) Sketch of the semiconductor microcavity with the quantum well embedded at the center of the spacer (shown in purple). (b) Strong coupling between the cavity photon and the exciton gives rise to formation of the lower (blue) and upper (red) polariton modes. The arrow indicates the Rabi splitting $\hbar\Omega_R$.

larly, for the cavity wavelengths λ_c in the range of 700–850 nm, which are close to the exciton energies in CdTe and InGaAs, $m_{ph} \sim 10^{-4} m_e$.

1.4 Strong light-matter coupling

In the previous section it was shown how the excitons and photons can be localized in space and represent a 2D system. For the coupling of these two entities, we consider a single quantum well placed in the cavity at the antinode of the electric field. To maximize the light field at the antinode, we minimize the number of the antinodes in the resonator by making the distance between two mirrors as short as possible and thus realizing a microcavity (Figure 1.4a). Particularly, the strongest light-matter coupling can be realized in a $\lambda/2$ -cavity with the length of $L = \lambda/2n_c$, where only one field antinode is present in the resonator.

Due to the interaction of the electromagnetic field in the cavity to the excitonic dipole, the cavity photon can be absorbed in the quantum well and lead to formation of an exciton, and the latter in turn can emit light at the resonant wavelength of the cavity. In the regime of *weak coupling* the energy of this coupling is comparable to the linewidth, and thus the photons can quickly leak out from the cavity. On the contrary, in the *strong coupling* regime the mutual transformation of photons and excitons into each other can occur multiple times during the lifetime of the system. This leads to renormalization of the energy states and their anticrossing.

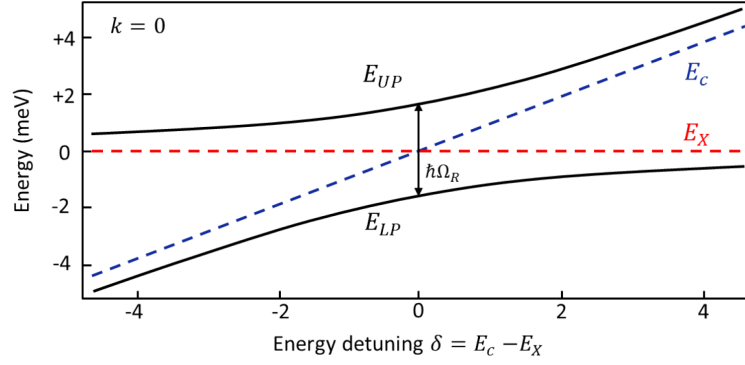


Figure 1.5: Dependence of the splitting between the upper and lower polariton lines at $k = 0$ on the exciton-photon detuning δ . Adapted from [34].

In this case, the system Hamiltonian can be written as [37]

$$\hat{H} = \sum_k E_C(k) \hat{c}_k^\dagger \hat{c}_k + \sum_k E_X(k) \hat{x}_k^\dagger \hat{x}_k + \sum_k \frac{\hbar \Omega_R}{2} (\hat{c}_k^\dagger \hat{x}_k + \hat{x}_k^\dagger \hat{c}_k) \quad (1.10)$$

where \hat{c}_k, \hat{x}_k ($\hat{c}_k^\dagger, \hat{x}_k^\dagger$) are operators of photon and exciton annihilation (creation) at the wavevector k . The term Ω_R is called *Rabi splitting* and represents the strength of the exciton-photon coupling. This Hamiltonian can be rewritten in a 2-by-2 matrix form:

$$\hat{H} = \begin{pmatrix} E_C(k) & \frac{\hbar \Omega_R}{2} \\ \frac{\hbar \Omega_R}{2} & E_X(k) \end{pmatrix} \quad (1.11)$$

Here the diagonal terms $E_X(k)$ and $E_C(k)$ describe the eigenenergies of the exciton and the photon, and the off-diagonal terms correspond to the coupling. The spectrum of this Hamiltonian, i.e. its eigenenergies can be found by diagonalization of equation (1.10). The new eigenstates of the system in this case are mixed states of the exciton and the photon that are called *upper polariton* (UP) and *lower polariton* (LP):

$$\hat{H} = E_{LP}(k) \hat{a}_k^\dagger \hat{a}_k + E_{UP}(k) \hat{b}_k^\dagger \hat{b}_k \quad (1.12)$$

with the energies given by

$$\begin{aligned} E_{LP}(k) &= \frac{1}{2} (E_C(k) + E_X(k)) - \frac{1}{2} \sqrt{\delta^2 + \hbar^2 \Omega_R^2} \\ E_{UP}(k) &= \frac{1}{2} (E_C(k) + E_X(k)) + \frac{1}{2} \sqrt{\delta^2 + \hbar^2 \Omega_R^2} \end{aligned} \quad (1.13)$$

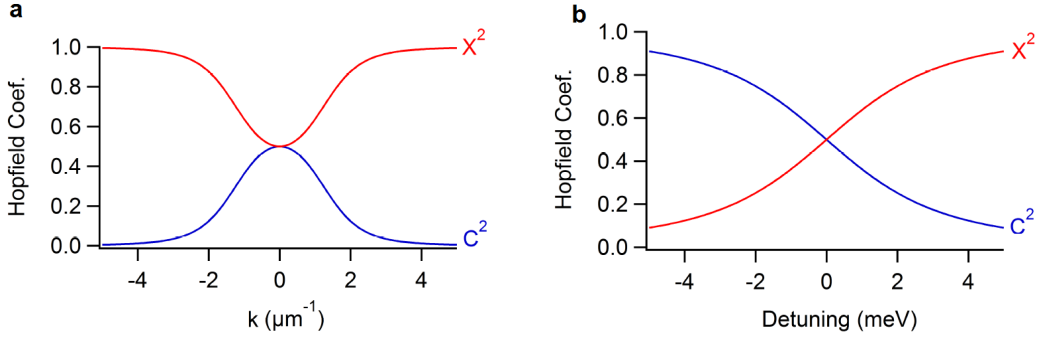


Figure 1.6: (a) Dependence of the Hopfield coefficients for the lower polariton mode on the in-plane momentum k at $\delta = 0$. (d) Dependence of the Hopfield coefficients for the lower polariton mode on the exciton-photon detuning δ at $k = 0$. Represented from [38].

where $\delta = E_C(k) - E_X(k)$ is the *exciton-photon detuning*. The spectrum of the microcavity in the strong coupling regime is shown in Figure 1.4b. The most striking feature of this spectrum is the *anticrossing* of the upper and lower polariton dispersion curves. For zero exciton-photon detuning $\delta = 0$ the splitting between the upper and lower polariton branches at $k = 0$ equals to the Rabi splitting Ω_R . For other detunings, the value of splitting is larger. Dependence of the energy minima of the polariton branches on the detuning δ is presented in Figure 1.5.

The annihilation operators for polaritons are given by linear combination of those for the photon and the exciton:

$$\begin{aligned}\hat{a}_k &= X_k \hat{x}_k + C_k \hat{c}_k \\ \hat{b}_k &= C_k \hat{x}_k - X_k \hat{c}_k\end{aligned}\tag{1.14}$$

where X_k are C_k are *Hopfield coefficients* [7]. They are real values, obey $|X|^2 + |C|^2 = 1$, and are given by

$$\begin{aligned}|X_k|^2 &= \frac{1}{2} \left(1 + \frac{\delta}{\sqrt{\delta^2 + \Omega_R^2}} \right) \\ |C_k|^2 &= \frac{1}{2} \left(1 - \frac{\delta}{\sqrt{\delta^2 + \Omega_R^2}} \right)\end{aligned}\tag{1.15}$$

The Hopfield coefficients quantify the fraction to which the given polaritonic state can be considered as excitonic or photonic. For example, for $k = 0$ and $\delta = 0$ Hopfield coefficients are equal: $X = C = \frac{1}{\sqrt{2}}$. Another important example is the negative detuning equal to the

Rabi splitting: $\delta = -\Omega_R$, for which $|X|^2 \approx 0.15$, and $|C|^2 \approx 0.85$, which implies that the lower polariton branch is highly photonic. Dependence of the Hopfield coefficient on the wavevector and the exciton-photon detuning is presented in Figure 1.6. Operation at negative detunings allow realization of very low effective mass of polaritons, providing high mobility and possible realization of macroscopic coherent states.

Probably the most striking feature of polaritons for experimental implementations is their ability to couple to the light. Particularly, the polaritons can be easily excited with a laser source tuned at the wavelength of the cavity mode. Even more, polaritons can maintain the polarization of the light source due to the fact that the photons with left- or right-circular polarization couple to the excitons with the spin $s = \pm 1$, respectively [31].

On the other hand, polaritons decay through their photonic component due to its low lifetime (~ 10 ps) in comparison to the excitonic one (~ 100 ps), and the photon escaping the cavity inherits most of the polariton properties. By performing standard optical measurements of the light emitted by the microcavity, one can get access to the energy, wavevector, polarization, phase, and statistical properties of the polaritons [39]. Simultaneous access to the intensity and the phase of the coherent ensembles of polaritons gives full information about the wavefunction, thus making the polaritons a remarkable system for the thorough studies of macroscopic coherent states. This is a significant but not the only benefit of the polaritonic system over the atomic Bose-Einstein condensates, where the phase can be accessed only at a cost of complicated experimental layouts. The macroscopic coherence of polaritons and concept of polariton Bose-Einstein condensation will be discussed in the next section.

1.5 Bose-Einstein condensation

Under appropriate conditions the particles obeying the bosonic statistics can occupy the same energy level. Bosons massively occupying the ground energy state of the system and keeping coherence between each other form a *Bose-Einstein condensate* (BEC), a state of matter where the macroscopic population behaves as a single quantum object. The phenomenon of BEC was first noticed by Bose as a feature of the bosonic energy distribution [40], and then extended by Einstein who described the process of bosonic stimulation leading to the massive occupation of the ground energy state [41].

The nature of the phase transition from a thermal distribution to a BEC can be understood in the framework of the thermal de Broglie wavelength. When, for a given density of particles n_p ,

the temperature is high, the wavefunctions of the separated particles do not overlap, and the interactions in the system occur due to the elastic scattering on each other. However, when the temperature goes below a certain threshold, the extent of the wavefunctions of different atoms starts to be larger than the mean distance between the atoms. Overlap of the wavefunctions of the isolated atoms leads to formation of a macroscopic coherent state. From this picture, the phase transition should occur when the system temperature is decreased below a certain threshold value [42]

$$T_C = \frac{2\pi\hbar^2}{m} \left(\frac{n_p}{2.612} \right)^{2/3}, \quad (1.16)$$

where m is the mass of bosons.

Equation (1.16) can explain why the BEC was so hard to achieve in the experimental conditions. Given the mass of the sodium atoms of the order $m \sim 10^5 m_e$, the threshold temperature of their Bose-Einstein condensation is only $T \sim 10^{-6}$ K. Reaching such low temperatures required a lot of experimental challenges including creation of magnetooptic atomic traps and realization of a sub-Doppler cooling of atoms [43, 44]. On the contrary, for the lower polaritons at $k = 0$ with an effective mass $m \sim 10^{-4} m_e$, the threshold temperature can be as high as dozens of Kelvins. Thanks to such low effective mass, polariton condensation was observed at liquid helium temperature in microcavities made of CdTe [45] and GaAs [46], and even at the room temperature in GaN [47], organic semiconductors like anthracene [48], and organic polymers [49, 50].

1.5.1 Nonresonant excitation

The process of Bose-Einstein condensation implies the transition from the Boltzmann to the Bose energy distribution. The convenient way to realize the Boltzmann statistics is to excite the system *nonresonantly* with a laser energy larger than the bandgap of the material E_g . Such excitation creates free charge carriers, which shortly relax to the bottom of the conduction band and top of the valence band, then form excitons, and eventually reach the lower polariton dispersion curve at low values of k . Nevertheless, the low lifetime of the photonic component of polaritons can deplete the ground energy state at $k = 0$ before it will get a significant enough occupancy to form a coherent state. An additional difficulty arises from the steep polariton dispersion at low values of k , which reduces the scattering probability with acoustic phonons since they have low energy. Together with the decreased density of states around these values

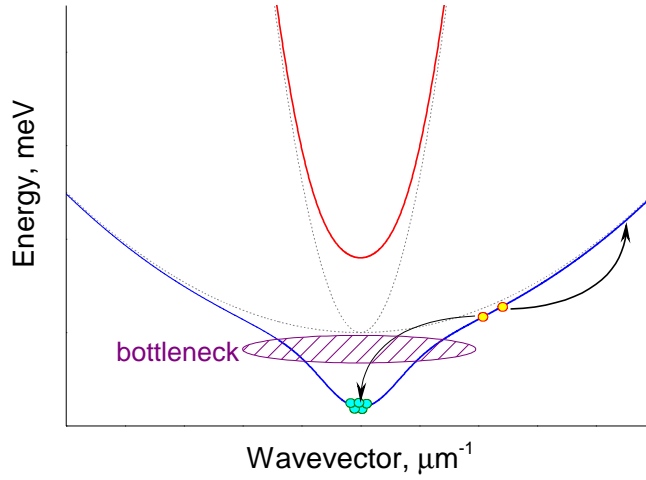


Figure 1.7: Schematic diagram of the upper and lower polariton branches. A large bottleneck due to low probability of exciton-phonon scattering is shown with hatched ellipse. The ground state can be effectively populated through the stimulated scattering process shown with arrows.

of k , this leads to formation of a *bottleneck region* at high k , where the polaritons can get trapped for dozens of picoseconds without relaxing to the ground state and thus without formation of a BEC (Figure 1.7).

The mechanism that allows to overcome the trapping in the bottleneck region is the stimulated scattering of polaritons to the ground state. In fact, the bosonic statistics implies that the probability of transition to the ground state with N particles is proportional to $N + 1$ [41]. Therefore, under appropriate conditions even a small initial population at the bottom of the dispersion can trigger a fast massive transition of the particles to the ground state. In this case the stimulation rate will be faster than the dissipation from the cavity, allowing to get large occupancy of the ground state. A necessary condition for the stimulated scattering is the availability of the states on the dispersion curve that can support the energy and momentum conservation for two particles, one of which relaxes to the ground state, and the second gets excited (Figure 1.7). Although this mechanism is considered to be the main one for the energy relaxation [51], the role of the stimulated scattering mediated by the phonons was also emphasized in several works [52].

Besides the occupation of the ground state, the second necessary condition for claiming the realization of a BEC is the appearance of a macroscopic coherence in the system. This implies that after the occupation of the ground state its phase gets synchronized over the whole BEC region. This property can be accessed by observing the interference pattern from two spatially

separated parts of the BEC, which can be described in the context of the first-order spatial coherence function.

The Bose-Einstein condensation of polaritons was first unambiguously confirmed by the massive occupation of the ground state and appearance of the first-order spatial coherence in 2006 [45]. It has been shown that the transition from the Boltzmann statistics to the BEC is also accompanied by a nonlinear increase of the emission intensity, narrowing of the ground state emission linewidth, and locking of the polarization. In fact, the emission of a single-mode polariton BEC maintains its coherence and is therefore hardly distinguishable from the lasing of a VCSEL with the same geometry [53]. However, the latter appears at much higher densities above the Mott transition, when the density of carriers is so high that the system is described not in terms of excitons, but rather electron-hole plasma. Moreover, multiple effects confirming the BEC nature were observed in following years, including vorticity [11, 12], superfluidity [10], propagation of the condensate away from the excitation spot [54], and Josephson effect between the coupled BECs [55].

An important difference between the atomic and polariton BEC is that the latter does not form a thermalized condensate, but rather a driven-dissipative one. The polaritonic system is subject to a permanent dissipation due to the photonic component leaking out of the resonator, and at the same time it is constantly refilled through the stimulated scattering by the excitonic reservoir. The theoretical description of such system can be done within the framework of the mean-field model, which essentially reduces the full many-body Hamiltonian to mean component of the system wavefunction [42]. Within the mean-field approximation, the evolution of the system is given by *nonlinear Schrodinger equation* or *Gross-Pitaevskii equation* (GPE):

$$i\hbar \frac{\partial}{\partial t} \Psi(\mathbf{r}, t) = \left[-\frac{\hbar^2}{2m} \nabla^2 + V(\mathbf{r}) + \hbar g |\Psi(\mathbf{r}, t)|^2 + \frac{i\hbar}{2} (R_R n(\mathbf{r}, t) - \gamma_c) \right] \Psi(\mathbf{r}, t), \quad (1.17)$$

where $\Psi(\mathbf{r}, t) = |\Psi(\mathbf{r}, t)| e^{i\phi(\mathbf{r}, t)}$ is the system wavefunction, $V(\mathbf{r})$ is the potential landscape, g represents the polariton-polariton interactions, and γ_c is the polariton lifetime. The term $R_R n(\mathbf{r}, t)$ represents the driving of the condensate by the excitons relaxing from the incoherent reservoir. More specifically, R_R is a phenomenological parameter that represents rate of the excitonic scattering into the condensed state, and $n(\mathbf{r}, t)$ is the density of the reservoir obeying

a classical rate equation

$$\frac{\partial}{\partial t} n(\mathbf{r}, t) = P(\mathbf{r}, t) - \gamma_R n(\mathbf{r}, t) - R_R n(\mathbf{r}, t) |\Psi(\mathbf{r}, t)|^2 \quad (1.18)$$

with γ_R being the exciton lifetime, and $P(\mathbf{r}, t)$ representing the spatiotemporal distribution of the optical excitation. This model was developed in the works [56, 57] and was shown to describe remarkably well the behavior of the polariton BEC, including topological defects [11, 58] and finite size of the excitation spot $P(\mathbf{r}, t)$ [57].

1.5.2 Resonant excitation

Given that the polaritons are the eigenstates of the microcavity in the strong coupling regime, they easily couple to the light if the energy of the photon equals the one of the polariton. Therefore one can simply excite the polaritons on the bottom of the lower polariton branch by addressing them with a laser with a corresponding wavelength. In this case, high occupancy of the ground state together with the large de Broglie wavelength of polaritons will lead to formation of a macroscopic coherence. This provides us with a straightforward tool to create the coherent state without a need for any particular conditions to support the Bose-Einstein condensation process. The resonantly excited polariton population should not be mixed with a polariton BEC, since the latter is the dynamical phase transition that occurs due to stimulated scattering. Nevertheless, being a macroscopic coherent state, the resonantly excited polariton population features most of the properties of the BEC and can be well described within the mean-field approximation.

1.5.3 Conclusion

In this Chapter we covered the basics of the strong light-matter coupling in semiconductor microcavities and formation of exciton-polaritons. The microcavity polaritons are bright example of hybrid light-matter quasiparticles that inherits some properties of its ancestors, like repulsive interactions from the excitonic component, or low effective mass from the photonic one. The latter is an important prerequisite for the overlap of the wavefunctions of individual polaritons, allowing them to form a prominent quantum coherent state. More importantly, the polaritons are easily addressable by the external light fields, which makes it possible to excite them with the lasers, and at the same time to measure the amplitude, phase, and spatial distribution of their wavefunction with standard optical detectors. As a

consequence, microcavity emission inherits the coherence properties of the polaritons and therefore allows to study the coherence of their macroscopic quantum state. In the next Chapter we will introduce basic concepts of quantum optics to further address the questions of polariton coherence in more details.

2 Concepts of quantum optics

As it was shown in Chapter 1, the polaritons can form a macroscopic coherent state thanks to their low effective mass and large de Broglie wavelength. The coherence in this context means that the ensemble of polariton will have a long-range order, i.e. the behavior of the polaritonic wavefunction will preserve its features on the large distances. However, at certain conditions, the coherence of the macroscopic state can be perturbed. For instance, this can occur if the density of the polaritons is not high enough, which can be observed at the edges of the polariton condensate. On the other hand, it is well-known [35] that the state with well-defined number of particles cannot maintain the constant phase and therefore cannot keep its coherence.

Understanding of the effects that determine the coherence of the polaritonic system requires an accurate quantum mechanical description of the light field, a brief introduction to which will be given in this Chapter. We will consider the quantization of the electromagnetic field, several important examples of the states of light, and the measurable values of these states. Few possible tools for the generation of these light field states will be presented. Importantly, the light correlation functions of the first and the second order will be introduced, and their physical meaning will be discussed.

2.1 Statistics of photocounts

The discussion can be started by considering a very simplistic setup, a light beam that hits a fast photon detector. We pretend that the dead time of the detector Δt (i.e. the time required by the detector to recover after a photon detection) is negligibly small in comparison to the

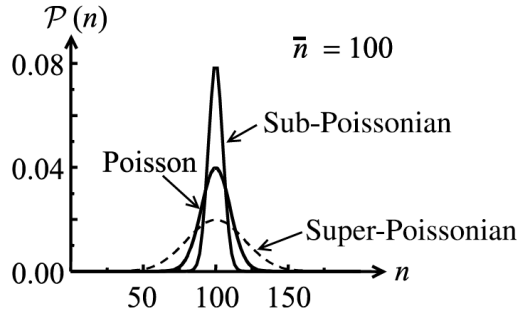


Figure 2.1: Example of the Poissonian, super-Poissonian, and sub-Poissonian photon number distributions $P(n)$ for the mean photon number $\bar{n} = 100$. Represented from [59].

period between the photon arrival times. This means that during any time interval Δt , the light stream contains either zero or one photon.

Let the light beam studied have a fixed mean power that does not change in time. For instance, such light can be simply generated by a laser. In this case, during a randomly chosen time period $T = N\Delta t$, where N is a large integer, the detector will receive a certain *mean number* of photons \bar{n} . Nevertheless, the distribution of photons in the light beam and hence their arrival time on the light detector is still a stochastic process. As a consequence, the exact number of photons detected during the time period T can differ from \bar{n} . The probability to detect n photons is given by a binomial distribution

$$P(n) = \frac{N!}{n!(N-n)!} p^n (1-p)^{N-n}, \quad (2.1)$$

where $p = \bar{n}/N$ is the probability to detect a photon in a time interval Δt . The function $P(n)$ is also called a *photon number distribution*. In the limit of $N \rightarrow \infty$ this expression can be transformed into a Poissonian distribution:

$$P(n) = \frac{\bar{n}^n}{n!} e^{-\bar{n}}. \quad (2.2)$$

The variance of the Poissonian distribution is known to be equal to its mean: $(\Delta n)^2 = \bar{n}$. Therefore, one may state that a coherent beam of light with a fixed power has a *Poissonian statistics* with the standard deviation of the photon number $\Delta n = \sqrt{\bar{n}}$.

A light beam with $\Delta n > \sqrt{\bar{n}}$ is called to have a *super-Poissonian statistics*. An intuitive example of this is the coherent light with fluctuating power, which leads to higher uncertainty of the photon number. On the contrary, the *sub-Poissonian* light with $\Delta n < \sqrt{\bar{n}}$ has a narrower

photon number distribution. Such a state of light is also called *non-classical* because it can neither be realized with coherent electromagnetic waves, nor be understood in the classical framework. This makes the non-classical light and its sources of significant interest for the study of various quantum aspects and certain practical applications. The examples of light with different photon number distributions are presented in Figure 2.1. The general description of the states of light can be done in the framework of quantum optics. Some basic concepts and examples will be considered in this Chapter.

2.2 Field quantization

The quantum mechanical description of the light relies on the quantization of the electromagnetic field. The quantization procedure described below generally follows the one presented in [60, 61]. We start by considering an electromagnetic field of a monochromatic plane wave of frequency ω in a one-dimensional cavity of length L . Without loss of generality, let the polarization direction be along the x-axis, and the direction of propagation be along the z-axis. Then the electric and magnetic components of the field can be expressed in the form

$$\begin{aligned} E_x &= \sqrt{\frac{2\omega^2}{\epsilon_0 V}} q(t) \sin(kz) \\ B_y &= \frac{\epsilon_0 \mu_0}{k} \sqrt{\frac{2\omega^2}{\epsilon_0 V}} p(t) \sin(kz) \end{aligned} \quad (2.3)$$

where $k = \omega/c$ is the wavevector, V is the mode volume, and $p(t)$ and $q(t)$ give the time dependence of the field. Here we assume that L is such that the wave fulfills the boundary conditions $E(0, t) = E(L, t) = 0$. The terms $p(t)$ and $q(t)$ give the time dependence of the field. Such an electromagnetic wave can be treated as an oscillator with $p(t)$ and $q(t)$ playing the role of canonical momentum and displacement. The classical Hamilton's function of such oscillator is given by

$$H = \frac{1}{2} (p^2 + \omega^2 q^2). \quad (2.4)$$

To make a transition to the quantum consideration, we simply replace the canonical variables with quantum operators $p \rightarrow \hat{p}$, $q \rightarrow \hat{q}$, and obtain

$$\hat{H} = \frac{1}{2} (\hat{p}^2 + \omega^2 \hat{q}^2), \quad (2.5)$$

Chapter 2. Concepts of quantum optics

where the operators \hat{p} and \hat{q} obey the commutation rule $[\hat{q}, \hat{p}] = i\hbar$.

Next, we introduce the *annihilation* and *creation* operators

$$\begin{aligned}\hat{a} &= \frac{1}{\sqrt{2\hbar\omega}}(i\hat{p} + \omega\hat{q}) \\ \hat{a}^\dagger &= \frac{1}{\sqrt{2\hbar\omega}}(-i\hat{p} + \omega\hat{q}),\end{aligned}\tag{2.6}$$

which obey the bosonic commutation rule $[\hat{a}, \hat{a}^\dagger] = 1$. Generally speaking, these operators are not Hermitian, and hence do not correspond directly to any observable. Using these operators, we can further rewrite the Hamiltonian in the form

$$\hat{H} = \hbar\omega \left(\hat{a}^\dagger \hat{a} + \frac{1}{2} \right).\tag{2.7}$$

The spectrum of this Hamiltonian is discrete and given by a set of equidistant energy levels $E_n = \hbar\omega(n + 1/2)$, where $n = 0, 1, 2, \dots$. This fact gives insight into the physical meaning of the creation and annihilation operators. If $|n\rangle$ is the eigenstate of the Hamiltonian with the corresponding eigenvalue E_n , then $\hat{a}^\dagger |n\rangle$ will also be the eigenstate:

$$\begin{aligned}\hat{H}\hat{a}^\dagger |n\rangle &= \hbar\omega \left(\hat{a}^\dagger \hat{a} + \frac{1}{2} \right) \hat{a}^\dagger |n\rangle = \hbar\omega \left[\hat{a}^\dagger \left(\hat{a}^\dagger \hat{a} + 1 \right) + \frac{1}{2} \hat{a}^\dagger \right] |n\rangle \\ &= \hbar\omega \left(n + \frac{3}{2} \right) \hat{a}^\dagger |n\rangle = E_{n+1} \hat{a}^\dagger |n\rangle.\end{aligned}\tag{2.8}$$

with the eigenvalue being the energy of the next state E_{n+1} . Therefore, the action of the operator \hat{a}^\dagger can be interpreted as adding of one more energy quantum into the system. Similarly, the operator \hat{a} removes one photon from the system. This explains why these operators are known as operators of photon creation and annihilation. Accounting for the normalization of the states, we can write

$$\begin{aligned}\hat{a}^\dagger |n\rangle &= \sqrt{n+1} |n+1\rangle, \\ \hat{a} |n\rangle &= \sqrt{n} |n-1\rangle.\end{aligned}\tag{2.9}$$

The state $|0\rangle$ containing no photons is called the *vacuum state* and obeys $\hat{a}|0\rangle = 0$.

The electric field operator can be obtained from the classical expression (2.3) by using the definition (2.6):

$$\hat{E}(z, t) = \mathcal{E}_0 \left(\hat{a} e^{-i\omega t} + \hat{a}^\dagger e^{i\omega t} \right).\tag{2.10}$$

In fact, the field can be more illustratively described in terms of the *quadrature operators*:

$$\begin{aligned}\hat{X}_1 &= \frac{1}{2} (\hat{a} + \hat{a}^\dagger) \\ \hat{X}_2 &= \frac{1}{2i} (\hat{a} - \hat{a}^\dagger)\end{aligned}\tag{2.11}$$

In this case, the electric field can be expressed as

$$\hat{E}(z, t) = \mathcal{E}_0 (\hat{X}_1 \cos \omega t + \hat{X}_2 \sin \omega t)\tag{2.12}$$

showing that the quadrature operators represent the electric field amplitudes with a phase shift of $\pi/2$ between them. The quadrature operators obey the standard commutation relation $[\hat{X}_1, \hat{X}_2] = i/2$, and therefore they satisfy the uncertainty relation

$$\langle (\Delta \hat{X}_1)^2 \rangle \langle (\Delta \hat{X}_2)^2 \rangle \geq \frac{1}{16}\tag{2.13}$$

The amplitude of the electric field at an arbitrary angle β can be described by the linear combination of \hat{X}_1 and \hat{X}_2 :

$$\hat{X}_\beta = \hat{X}_1 \cos \beta + \hat{X}_2 \sin \beta = \frac{1}{2} (\hat{a} e^{-i\beta} + \hat{a}^\dagger e^{i\beta}).\tag{2.14}$$

Finally, we introduce a *photon number operator* $\hat{n} = \hat{a}^\dagger \hat{a}$, named after the fact that it is Hermitian, and its observable is the number of photons in the state:

$$\langle n | \hat{n} | n \rangle = \langle n | \hat{a}^\dagger \hat{a} | n \rangle = \langle n | n | n \rangle = n.\tag{2.15}$$

Another observable related to the statistics of photocounts is the variance of the number of photons $\langle (\Delta n)^2 \rangle = \langle n^2 \rangle - \langle n \rangle^2$. In the quantum mechanical notations this operator applied to a state $|\psi\rangle$ reads

$$\langle \psi | (\Delta n)^2 | \psi \rangle = \langle \psi | \hat{a}^\dagger \hat{a} \hat{a}^\dagger \hat{a} | \psi \rangle - \langle \psi | \hat{a}^\dagger \hat{a} | \psi \rangle^2.\tag{2.16}$$

This finishes the introduction of the basic mathematical concepts of quantum optics. In the next section we will consider few important states of the light field and characterize some of their properties.

2.3 Examples of the light field states

Fock states

The eigenstates of the Hamiltonian (2.7)

$$\hat{H}|n\rangle = \hbar\omega\left(n + \frac{1}{2}\right)|n\rangle, \quad n = 0, 1, 2, \dots \quad (2.17)$$

are referred to as *Fock states* or *photon number states* because as was mentioned above, they correspond to the certain number of photons in the field. Consequently, the energy of the state $|n\rangle$ is also well-defined and equals to $E_n = \hbar\omega(n + 1/2)$. The full set of Fock states forms an orthogonal basis. Since Fock states are also the eigenstates of the photon number operator $\hat{a}^\dagger \hat{a}$, the mean photon number of the state $|n\rangle$ is simply n , as shown by equation (2.15). The variance of the photon number is given by

$$(\Delta n)^2 = \langle n | \hat{a}^\dagger \hat{a} \hat{a}^\dagger \hat{a} | n \rangle - \langle n | \hat{a}^\dagger \hat{a} | n \rangle^2 = n \langle n | \hat{a}^\dagger \hat{a} | n \rangle - n^2 = 0, \quad (2.18)$$

which means that Fock states possess well-defined number of photons. On the other hand, the expectation values of the field quadratures for these states is zero:

$$\langle n | \hat{X}_{1,2} | n \rangle = \frac{1}{2} \langle n | \hat{a} | n \rangle \pm \frac{1}{2} \langle n | \hat{a}^\dagger | n \rangle = 0. \quad (2.19)$$

This feature has a clear physical explanation: the electric field (more precisely, the phase of the field) is not defined at any moment of time. Although the Fock states are the eigenstates of the Hamiltonian, they cannot be put into correspondence with an electromagnetic wave with a classical description.

Coherent states

Unlike the Fock state, a plane monochromatic wave described by equation (2.3), like for instance emission of the laser, would exhibit the electric field oscillating with the frequency ω . As seen from equation (2.10), such wave should be eigenvectors of the linear combination of operators \hat{a}^\dagger and \hat{a} . We introduce the eigenstates of the annihilation operator \hat{a} :

$$\hat{a}|\alpha\rangle = \alpha|\alpha\rangle, \quad (2.20)$$

where $\alpha = |\alpha| e^{i\varphi}$ is a complex variable. These states exist and can be expressed in the basis of Fock states as

$$|\alpha\rangle = e^{-\frac{|\alpha|^2}{2}} \sum_{n=0}^{\infty} \frac{\alpha^n}{\sqrt{n!}} |n\rangle. \quad (2.21)$$

Generally speaking, they are not orthogonal and hence do not form a basis. The mean values of the quadratures for these states are

$$\begin{aligned} \langle \alpha | \hat{X}_1 | \alpha \rangle &= \frac{1}{2} \langle \alpha | \hat{a} | \alpha \rangle + \frac{1}{2} \langle \alpha | \hat{a}^\dagger | \alpha \rangle = \frac{1}{2} (\alpha + \alpha^*) = |\alpha| \cos \varphi, \\ \langle \alpha | \hat{X}_2 | \alpha \rangle &= |\alpha| \sin \varphi. \end{aligned} \quad (2.22)$$

Substituting this to equation (2.12), we can see that the electric field oscillates with the optical frequency ω , as expected for a plane monochromatic wave. Therefore, such states of the electromagnetic field are called *coherent states*. Physical meaning of $|\alpha|$ is the amplitude of the plane wave, and φ defines its phase. The variances of the quadratures are

$$\begin{aligned} \langle \alpha | (\Delta \hat{X}_{1,2})^2 | \alpha \rangle &= \frac{1}{4} \langle \alpha | \hat{a} \hat{a} + \hat{a}^\dagger \hat{a}^\dagger \pm \hat{a}^\dagger \hat{a} \pm \hat{a} \hat{a}^\dagger | \alpha \rangle - \frac{1}{2} \langle \alpha | \hat{a} \pm \hat{a}^\dagger | \alpha \rangle^2 \\ &= \frac{1}{4} \langle \alpha | \hat{a} \hat{a} + \hat{a}^\dagger \hat{a}^\dagger \pm 2 \hat{a}^\dagger \hat{a} + 1 | \alpha \rangle - \frac{1}{2} \langle \alpha | \hat{a} \pm \hat{a}^\dagger | \alpha \rangle^2 \\ &= \frac{1}{4} (\alpha^2 + \alpha^{*2} \pm 2|\alpha|^2 + 1) - (\alpha \pm \alpha^*)^2 = \frac{1}{4}. \end{aligned} \quad (2.23)$$

This means that the uncertainty of the field does not depend on its phase. Moreover, the coherent states are *minimum uncertainty states* because they turn the uncertainty relation (2.13) into an equality:

$$\langle (\Delta \hat{X}_1)^2 \rangle \langle (\Delta \hat{X}_2)^2 \rangle = \frac{1}{16}. \quad (2.24)$$

These features can be presented on a *phasor diagram* shown in Figure 2.2, where the mean value and uncertainty of the operators \hat{X}_1 and \hat{X}_2 are depicted. The coherent state (Figure 2.2b) is represented by the circle with diameter $\frac{1}{4}$, showing that the field variance is constant for any direction. The distance from the origin of coordinates to the center of the circle is defined by the mean photon number of the state:

$$\bar{n} = \langle \alpha | \hat{a}^\dagger \hat{a} | \alpha \rangle = |\alpha|^2. \quad (2.25)$$

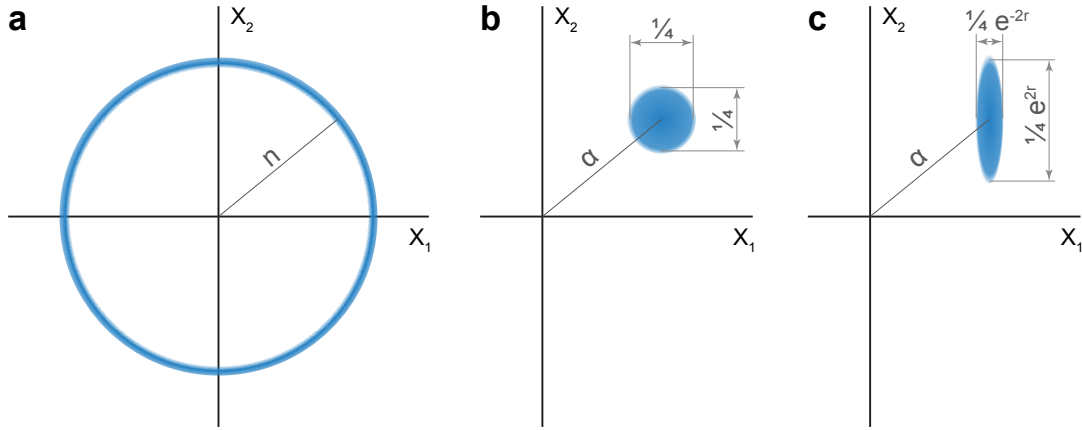


Figure 2.2: Examples of the (a) Fock, (b) coherent, and (c) squeezed states of light containing the same mean number of photons $\langle \hat{n} \rangle$ on the phasor diagram. The axes are the values of quadratures X_1 and X_2 . Shaded regions represent the uncertainty of the field.

The variance of the photon number is

$$(\Delta n)^2 = \langle \alpha | \alpha^* \hat{a} \hat{a}^\dagger \alpha | \alpha \rangle - |\alpha|^4 = |\alpha|^2 \langle \alpha | \hat{a}^\dagger \hat{a} + 1 | \alpha \rangle - |\alpha|^4 = |\alpha|^2, \quad (2.26)$$

which means that $\Delta n = \sqrt{\bar{n}}$, the standard deviation expected for the Poissonian photon number distribution (2.2).

From a mathematical point of view, it is convenient to describe the coherent states as a result of an action of a *displacement operator* $\hat{D}(\alpha)$ on the vacuum state:

$$|\alpha\rangle = \hat{D}(\alpha) |0\rangle, \quad \hat{D}(\alpha) = e^{\alpha \hat{a}^\dagger - \alpha^* \hat{a}}. \quad (2.27)$$

action of which can be illustrated on the phasor diagram (Figure 2.2b): it displaces the vacuum state on the distance $|\alpha|^2$ with a phase angle φ without changing the size of the uncertainty. Clearly, the vacuum state $|0\rangle$ is also an example of a coherent state.

Squeezed states

If for a certain state of light one of the quadratures X_1 or X_2 has an uncertainty less than $\frac{1}{4}$, such a state is called a *squeezed state*. These states correspond to the shaded regions in Figure 2.3, and they can be represented on the phasor diagram with an ellipse, the minor axis of which is aligned along the quadrature with a smaller uncertainty (Figure 2.2c). The squeezed

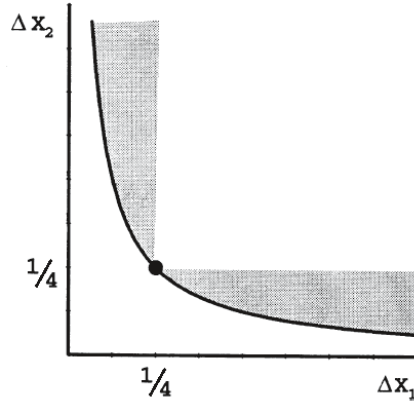


Figure 2.3: Classification of the states on the plot of ΔX_1 vs ΔX_2 . Minimum uncertainty states are situated on the black hyperbolic curve. Black dot marks the coherent state, while the gray shaded regions correspond to squeezed states. Represented from [62].

states can be generated through the action of a *squeezing operator* $\hat{S}(\xi)$:

$$\hat{S}(\xi) = e^{\frac{1}{2}[\xi^* \hat{a}^2 - \xi \hat{a}^{\dagger 2}]} \quad (2.28)$$

of a complex squeezing parameter $\xi = r e^{i\theta}$. A generic *coherent squeezed state* $|\alpha, \xi\rangle$ can be obtained from a vacuum state by acting on it consequently with squeezing and displacement operators (Figure 2.4):

$$|\alpha, \xi\rangle = \hat{D}(\alpha) \hat{S}(\xi) |0\rangle. \quad (2.29)$$

It can further be shown that these states are the eigenstates of the operator \hat{b}

$$\hat{b} = \hat{a} \cosh(r) - \hat{a}^\dagger e^{i\theta} \sinh(r), \quad (2.30)$$

which is a linear combination of \hat{a} and \hat{a}^\dagger . As discussed during the introduction of coherent states, this means that the electric field of squeezed states oscillates at the optical frequency ω . The important difference from the coherent states is that the fluctuations of the electric field are not constant, but is changing along with the field oscillations. This can be shown by expressing the operators \hat{a}, \hat{a}^\dagger through \hat{b}, \hat{b}^\dagger , and substituting it into equation (2.11). After several trivial transformations one can get

$$\langle \alpha, \xi | (\Delta \hat{X}_{1,2})^2 | \alpha, \xi \rangle = \frac{1}{4} (\sinh^2(r) + \cosh^2(r) \mp 2 \sinh(r) \cosh(r) \cos \theta). \quad (2.31)$$

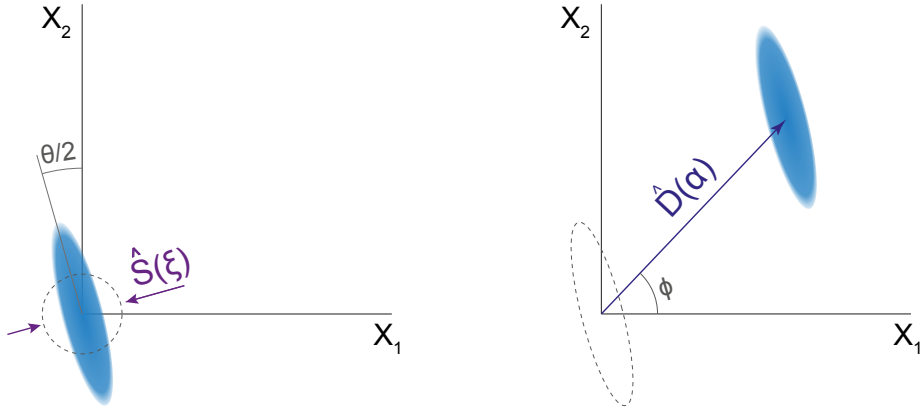


Figure 2.4: Subsequent action of the squeezing and displacement operators $\hat{S}(\xi)$ and $\hat{D}(\alpha)$ on the vacuum state $|0\rangle$ creates a squeezed coherent state $|\alpha, \xi\rangle$.

If for instance $\theta = 0$, this reduces to

$$\begin{aligned} (\Delta \hat{X}_1)^2 &= \frac{1}{4} e^{-2r} \\ (\Delta \hat{X}_2)^2 &= \frac{1}{4} e^{2r} \end{aligned} \quad (2.32)$$

clearly showing the squeezing in the first quadrature, and the increased fluctuations in the second. The squeezing magnitude $r = |\xi|$ determines by how much the fluctuations in the squeezed component are reduced. The phase θ is related to the phase of the electromagnetic wave at which the fluctuations will be reduced. For example $\theta = \pi$ will change the squeezing direction so that the second quadrature \hat{X}_2 will be squeezed. For an arbitrary θ , the squeezing can appear along certain direction \hat{X}_θ on the phasor diagram. Consequently, at certain squeezing angle one should expect a change in the fluctuations of the photon numbers. It can be shown [62] that

$$\begin{aligned} (\Delta n)^2 &= |\alpha|^2 [\sinh^2(r) + \cosh^2(r) + 2 \sinh(r) \cosh(r) \cos(\theta - 2\varphi)] \\ &\quad + 2 \sinh^2(r) \cosh^2(r). \end{aligned} \quad (2.33)$$

Depending on the phases of coherent state φ and squeezed state θ , the photon number fluctuation can achieve different values in the range between $(\Delta n)_{\max}^2$ and $(\Delta n)_{\min}^2$:

$$\begin{aligned} (\Delta n)_{\max}^2 &= |\alpha|^2 e^{2r} + 2 \sinh^2(r) \cosh^2(r), \\ (\Delta n)_{\min}^2 &= |\alpha|^2 e^{-2r} + 2 \sinh^2(r) \cosh^2(r). \end{aligned} \quad (2.34)$$

While maximal fluctuations of the photon number are always super-Poissonian, this is not always the case for the minimal ones. As a consequence, squeezed states can possess an arbitrary photon statistics, and even demonstrate a nonclassical behavior. This question will be addressed in more details in section 2.6.

2.4 Field correlation functions

The description of the electromagnetic field naturally raises a question about the limits of validity of the wave approximation. For instance, the features of an ideal plane monochromatic wave in vacuum do not change when it propagates over infinitely large distances. Clearly, this is not the case for realistic fields. The concept of *coherence* answers the question at which distances (no matter in space or in time) the electromagnetic field will resemble its initial properties. The measurements of coherence are, by definition, related to the comparison of the field at two spatially (or temporally) separated points. Therefore, the description of coherence should start with the description of the measurement of the field. In the case of a single-mode field, the detection intensity at space and time coordinates $x = (r, t)$ is given by

$$\begin{aligned} I(x) &= \sum_f |\langle \psi_f | E^+(x) | \psi_i \rangle|^2 = \sum_f \langle \psi_i | E^-(x) | \psi_f \rangle \langle \psi_f | E^+(x) | \psi_i \rangle \\ &= \langle \psi_i | E^-(x) E^+(x) | \psi_i \rangle, \end{aligned} \quad (2.35)$$

where $E^+(x)$ and $E^-(x)$ denote positive and negative frequency components of the field following Glauber's definition [63], $|\langle \psi_f | E^+(x) | \psi_i \rangle|^2$ gives the probability of the transition from the initial field state $|\psi_i\rangle$ to the final one $|\psi_f\rangle$, and the sum is calculated over all possible final states of the system. The last equality holds due to completeness of the final states: $\sum_f |\psi_f\rangle \langle \psi_f| = 1$. Remarkably, the resulting expression shows no dependence on the final states of the system.

In equation (2.35), $E^\pm(x)$ describe the field for the same point of space at the same time. However, in general one can introduce the *first order coherence function* defined for different points:

$$G^{(1)}(x_1, x_2) = \langle \psi_i | E^-(x_1) E^+(x_2) | \psi_i \rangle. \quad (2.36)$$

Chapter 2. Concepts of quantum optics

The coherence functions of higher orders can be introduced in a similar way:¹

$$G^{(n)}(x_1, \dots, x_n, x_{n+1}, \dots, x_{2n}) = \langle \psi_i | E^-(x_1) \dots E^-(x_n) E^+(x_{n+1}) \dots E^+(x_{2n}) | \psi_i \rangle. \quad (2.37)$$

The meaning of the first-order coherence can be revealed if one considers an experiment with two interfering waves $E_1(x_1)$ and $E_2(x_2)$ defined at certain points x_1 and x_2 . If the interference is observed on the screen at a position given by x_0 , then $E^+(x_0) = E_1^+(x_0) + E_2^+(x_0)$, and the intensity on the screen can be given by

$$I(x_0) = G^{(1)}(x_1, x_1) + G^{(1)}(x_2, x_2) + 2 |G^{(1)}(x_1, x_2)| \cos \phi \quad (2.38)$$

where ϕ is defined by the phase difference between two paths. By introducing the normalized *first-order coherence function*

$$g^{(1)}(x_1, x_2) = \frac{G^{(1)}(x_1, x_2)}{\sqrt{G^{(1)}(x_1, x_1) G^{(1)}(x_2, x_2)}} \quad (2.39)$$

equation (2.38) can be rewritten in a form

$$I(x_0) = I_1(x_0) + I_2(x_0) + 2g^{(1)}(x_1, x_2) \sqrt{I_1(x_0) I_2(x_0)} \cos \phi. \quad (2.40)$$

Here $I_{1,2}(x_0)$ are intensities of each of the two interfering waves on the screen, in the absence of the second wave. From equation (2.40) it is evident that $g^{(1)}$ characterizes the contrast of the interference achievable at different ϕ , and therefore defines the coherence of the amplitudes of two electromagnetic waves. For the maximal achievable value of $g^{(1)} = 1$, the destructive interference can lead to complete suppression of the light. For $g^{(1)} < 1$, the light intensity never goes to zero due to the presence of non-coherent components of light.

Next, we consider the *second-order coherence function*, which can be defined from equation (2.37) as

$$G^{(2)}(x_1, x_2) = \langle \psi_i | E^-(x_1) E^-(x_2) E^+(x_2) E^+(x_1) | \psi_i \rangle. \quad (2.41)$$

¹The definition of coherence functions can be generalized to the non-pure states that can be described with the density matrix $\rho = \sum_i |i\rangle \langle i|$. In this case, $G^{(n)}(x_1, \dots, x_n, x_{n+1}, \dots, x_{2n}) = \text{Tr} \{ \rho E^-(x_1) \dots E^-(x_n) E^+(x_{n+1}) \dots E^+(x_{2n}) \}$. However, for sake of simplicity only the pure states are considered in this thesis, and therefore the general definition can be reduced to equation (2.37).

Neglecting the spatial degree of freedom that will be of no interest for us, a normalized *second-order correlation function* can be defined as

$$g^{(2)}(t_1, t_2) = \frac{\langle \psi_i | E^-(t_1) E^-(t_2) E^+(t_2) E^+(t_1) | \psi_i \rangle}{\langle E^-(t_1) E^+(t_1) \rangle \langle E^-(t_2) E^+(t_2) \rangle} = \frac{\langle I(t_1) I(t_2) \rangle}{\langle I(t_1) \rangle \langle I(t_2) \rangle}. \quad (2.42)$$

This expression is also true for a single mode field. In this case, the correlation between the different moments of time is measured. An important case is the *zero-delay second-order correlation function* $g^{(2)}(0) = g^{(2)}(t, t)$, which defines the properties of the field at a given moment of time.

For the quantum description of the system, the functions $E^\pm(x)$ should be replaced with their quantum analogs, creation and annihilation operators \hat{a}, \hat{a}^\dagger :

$$g^{(2)}(0) = \frac{\langle \hat{a}^\dagger \hat{a}^\dagger \hat{a} \hat{a} \rangle}{\langle \hat{a}^\dagger \hat{a} \rangle^2} \quad (2.43)$$

or with a photon number operator

$$g^{(2)}(0) = \frac{\langle \hat{a}^\dagger (\hat{a} \hat{a}^\dagger + 1) \hat{a} \rangle}{\langle \hat{a}^\dagger \hat{a} \rangle^2} = \frac{\langle \hat{n}^2 \rangle - \langle \hat{n} \rangle}{\langle \hat{n} \rangle^2} = 1 + \frac{\langle (\Delta \hat{n})^2 \rangle - \langle \hat{n} \rangle}{\langle \hat{n} \rangle^2}. \quad (2.44)$$

The last expression provides an important link between $g^{(2)}(0)$ and the photon number distribution. The sign of the term $\langle (\Delta \hat{n})^2 \rangle - \langle \hat{n} \rangle$ depends on the width of the photon number variance: it will be positive for super-Poissonian statistics and negative for the sub-Poissonian one. As a consequence, we can classify the nature of light from the value of $g^{(2)}(0)$:

- $g^{(2)}(0) < 1$: nonclassical (sub-Poissonian)
- $g^{(2)}(0) = 1$: Poissonian
- $g^{(2)}(0) > 1$: super-Poissonian

The classical equation (2.42) provides a simple way to measure $g^{(2)}(0)$. If the field can be simultaneously detected by two receivers that record the field intensity dynamics $I_1(t)$ and $I_2(t)$, then the second-order correlation function can be calculated as

$$g^{(2)}(0) = \frac{\langle I_1(t) I_2(t) \rangle_t}{\langle I_1(t) \rangle \langle I_2(t) \rangle_t}, \quad (2.45)$$

where the expressions in brackets are averaged over time.

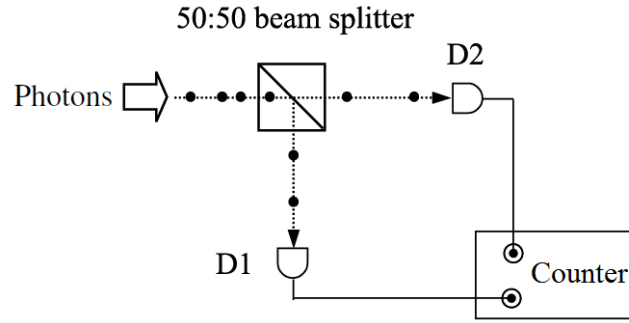


Figure 2.5: Scheme of the Hanbury Brown and Twiss experiment. The photon stream is split into two and detected by two receivers. The counter calculates the correlations defined by equation (2.46). Represented from [59].

This approach was first used by R. Hanbury Brown and R. Twiss at radiowave frequencies to measure the size of cosmic radio sources [64]. For the study of a collimated beam of light, Hanbury Brown and Twiss proposed to use a beamsplitter to split the photon stream into two and measure the coincidences between the photons arriving on two detectors (Figure 2.5).² In the quantum limit, when the detectors measure not the mean intensity of light but number of photons $n_{1,2}(t)$ detected during a short time interval Δt , equation (2.45) can be rewritten:

$$g^{(2)}(0) = \frac{\langle n_1(t) n_2(t) \rangle_t}{\langle n_1(t) \rangle \langle n_2(t) \rangle_t}. \quad (2.46)$$

It is illustrative to calculate the second-order correlation function for some states of light that have been considered in section 2.3. For the Fock states

$$g^{(2)}(0) = \frac{\langle n | \hat{a}^\dagger \hat{a}^\dagger \hat{a} \hat{a} | n \rangle}{\langle n | \hat{a}^\dagger \hat{a} | n \rangle^2} = \frac{n^2 - n}{n^2} = 1 - \frac{1}{n}. \quad (2.47)$$

The most interesting case is the single photon state $|1\rangle$, for which $g^{(2)}(0) = 0$. An easy way to understand this is a direct look on the HBT measurement scheme: if a single photon is sent to the beamsplitter, it will pass either on one or on the other detector, but never on both. Therefore, the numerator in equation (2.46) will always be zero.

²The beamsplitter can be considered as a device splitting the input beam into two output ones only at high beam intensities. Generally speaking, the beamsplitter has two inputs and mixes them to produce two output modes, and the signal in the second input is the vacuum field $|0\rangle$. Some particular effects of the vacuum field can be observed at low number of photons in the input signal [60].

For the coherent state $|\alpha\rangle$

$$g^{(2)}(0) = \frac{\langle \alpha | \hat{a}^\dagger \hat{a}^\dagger \hat{a} \hat{a} | \alpha \rangle}{\langle \alpha | \hat{a}^\dagger \hat{a} | \alpha \rangle^2} = \frac{|\alpha|^2 \langle \alpha | \hat{a}^\dagger \hat{a} | \alpha \rangle^2}{|\alpha|^4} = 1, \quad (2.48)$$

which corresponds with the fact that the coherent (laser) light has a Poissonian photon number distribution. It can be shown in a similar way that, for a coherent state, the coherence function of any order is unity.

The light with a super-Poissonian statistics will give rise to $g^{(2)}(0) > 1$. For instance, the light emitted by a thermal source (which was not considered here) gives $g^{(2)}(0) = 2$. The super-Poissonian light is also called *bunched*, because values of $g^{(2)}(0) > 1$ require simultaneous detections of photons by both detectors of the HBT setup. This effectively means that the photons reach the detectors in bunches. On the contrary, light with a sub-Poissonian statistics is referred to as *antibunched*, emphasizing that the photons have a tendency to propagate separately.

Considering the squeezed coherent light, it was shown in equation (2.34) that the statistics of photocounts can be both sub- and super-Poissonian, and therefore might lead to both bunching and antibunching. The expression for $g^{(2)}(0)$ will be derived in section 2.6.

2.5 Generation of nonclassical light

The states of light with reduced quadrature or photon number fluctuations are of high interest for quantum cryptography [65], quantum computing [66], and sub-shot noise interferometry [67]. At the same time, they cannot be described in a classical framework, and therefore cannot be generated with classical light sources. In fact, most ways of producing the nonclassical light utilize a coherent light source and a medium capable to affect the light statistics and field fluctuations. Below we provide some bright examples of such systems.

Single emitters. An evident way to generate a single photon Fock state $|1\rangle$ is to consider a two-level transition in an isolated atom (or atom-like system). After the emission of a photon, the system requires some time to return into the excited state to emit the second one. In this sense, the single emitter works as a quantum filter capable to absorb exactly one photon from the external field (in other words, project the external field on a single-photon basis), and then re-emit it. This approach is widely implemented with artificial atoms, for example, NV-centers [68]. One of the drawbacks is that the arrival time of the photon cannot be known in advance.

Photon blockade. Another way to absorb a single photon can be realized in media with very strong single-particle nonlinearity. If the nonlinear interaction is so strong that the energy shift $E_2 - E_1$ between the single photon state E_1 and two-photon state E_2 gets larger than the linewidth, then the resonant excitation will not be able to add the second photon into the system. This concept is very similar to the Coulomb blockade for quantum well electrons, but requires a very strong nonlinearity in case of photons [69]. Practically, it has been first achieved in 2005 [70] in a cavity containing a single atom.

Heralding. The photonic nonlinearity provides another tool for generation of single-photon Fock states due to parametric down-conversion process. The nonlinear susceptibility $\chi^{(2)}$ leads to nonlinear dependence of the medium polarization P on the electric field E :

$$P = \epsilon_0 (\chi^{(1)} E + \chi^{(2)} E^2). \quad (2.49)$$

Under certain condition the quadratic term gives rise to the generation of electromagnetic waves with frequencies differing from the initial one, and satisfying $\hbar\omega_{in} = \hbar\omega_{out,1} + \hbar\omega_{out,2}$. On a quantum level this corresponds to splitting of one input photon into two. Therefore, for two certain output modes a and b , the quantum state can be described in the Fock basis as

$$|\Psi\rangle = c_0 |0\rangle_a |0\rangle_b + c_1 |1\rangle_a |1\rangle_b + c_2 |2\rangle_a |2\rangle_b + \dots \quad (2.50)$$

If the down-conversion rate is low, then c_2 and higher-order terms will be negligibly small. To select the Fock state $|1\rangle$ in one of the modes, one can project Ψ on the single-photon state in the single mode:

$$\langle 1|_b |\Psi\rangle = \langle 1|_b (c_0 |0\rangle_a |0\rangle_b + c_1 |1\rangle_a |1\rangle_b) = c_1 |1\rangle_a. \quad (2.51)$$

Practically this can be done using a single-photon detector, click of which will mean that there is a single photon Fock state in the second output arm [71].

Squeezing in the parametric processes. In a degenerate parametric process with $\omega_{out,1} = \omega_{out,2}$ the input and output fields are coupled to each other by the terms $g\hat{a}_{in}\hat{a}_{out}^{\dagger 2} + g^*\hat{a}_{in}^{\dagger}\hat{a}_{out}^2$. When substituted in the unitary evolution operator, they naturally lead to quadratic terms $\exp(\xi^*\hat{a}^2 - \xi\hat{a}^{\dagger 2})$ in the squeezing operator (2.28). The reversed process, the second harmonic generation, can be described in a similar way and is used for squeezed light generation in gravitational wave detectors [72].

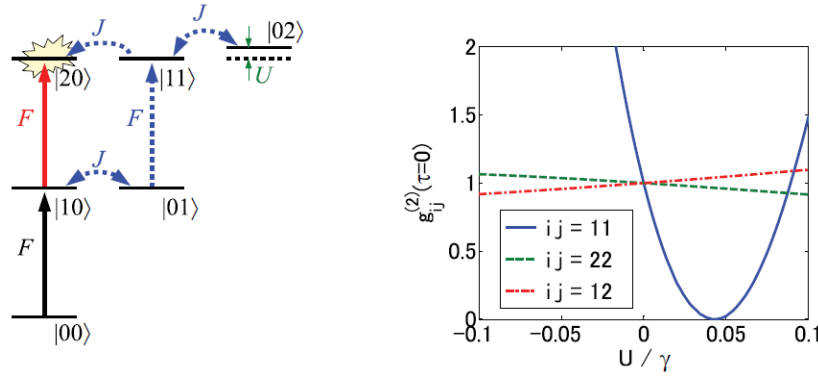


Figure 2.6: Left: destructive quantum interference of two quantum paths (red and blue) cancels the probability of having two photons in the first mode. Right: the strongest antibunching (blue curve) is obtained for a certain value of nonlinearity. Reproduced from [74].

Squeezing due to Kerr nonlinearity. The third-order nonlinear susceptibility $\chi^{(3)}$ gives rise to the Kerr effect, implying that the refractive coefficient of the media is dependent on the light intensity I as $n = n_0 + n_2 I$. If one enters such medium with a coherent light, the quantum fluctuation of the field will modulate the refractive index, which, in turn, will affect the phase of light. The combination of these effect can affect the fluctuations of a coherent state along some direction, leading to its squeezing [73].

Unconventional photon blockade. The abovementioned photon blockade mechanism relies on the strong single-particle nonlinearity. Surprisingly enough, if one considers a system of two coupled modes, then even a moderate nonlinearity can lead to noticeable quantum features. The concept of *unconventional photon blockade* introduced in [24, 74] utilizes a destructive quantum interference between two paths, which cancels the probability of having two photons in one of the modes (Figure 2.6). This proposal became recently the focus of multiple theoretical studies [75, 76, 77], including consideration of polarizations [78], coupling to optomechanical systems [79], and ability to build a photonic circuit implementing this mechanism [80]. Nevertheless, no nonclassical statistics generated due to this concept has been reported so far.

Squeezing in coupled nonlinear modes. Further research of the unconventional blockade [81] has shown that the antibunching is a manifestation of a more general phenomenon, the squeezing of Gaussian states. This implies that the destructive interference does not create a Fock state, but leads to the squeezing of the external coherent field. Surprisingly enough, for properly adjusted parameters of the system one can achieve very strong antibunching.

This is exactly what was predicted to occur for the unconventional blockade mechanism. To get a deeper understanding on how does the quadrature squeezing affect the second-order coherence, we derive a generic expression for $g^{(2)}(0)$ of squeezed coherent light.

2.6 Second-order correlations of the squeezed coherent state

A general squeezed coherent state can be obtained by applying consequently the squeezing and displacement operators on the vacuum state:

$$|\alpha, \xi\rangle = \hat{D}(\alpha) \hat{S}(\xi) |0\rangle \quad (2.52)$$

The expectation values for the creation and annihilation operators and their combinations can be calculated by substituting them with the eigenoperators \hat{b} and \hat{b}^\dagger :

$$\begin{aligned} \langle \alpha, \xi | \hat{a} | \alpha, \xi \rangle &= \alpha \\ \langle \alpha, \xi | \hat{a}^\dagger \hat{a} | \alpha, \xi \rangle &= |\alpha|^2 + \sinh^2(r) \end{aligned} \quad (2.53)$$

The last line is the expectation value for the number of photons. Surprisingly, the mean number of photons is not zero for a squeezed vacuum state. Consequently, the variance of the photon number is given by

$$\begin{aligned} (\Delta \hat{n})^2 &= |\alpha|^2 [\sinh^2(r) + \cosh^2(r) + 2 \sinh(r) \cosh(r) \cos(\theta - 2\varphi)] \\ &\quad + 2 \sinh^2(r) \cosh^2(r). \end{aligned} \quad (2.54)$$

and depends on the phases of the displacement and squeezing operator. A general expression for the zero-delay second-order correlation function is

$$\begin{aligned} g^{(2)}(0) &= 1 + \frac{\langle (\Delta \hat{n})^2 \rangle - \langle \hat{n} \rangle^2}{\langle \hat{n} \rangle^2} \\ &= 1 + \frac{2|\alpha|^2 [\sinh^2(r) - \sinh(r) \cosh(r) \cos(2\varphi)] + \sinh^2(r) \cosh^2(2r)}{(|\alpha|^2 + \sinh^2(r))^2}. \end{aligned} \quad (2.55)$$

This expression can be further simplified by introducing $p = \sinh^2(r)$, $s = \sinh(r) \cosh(r)$:

$$g^{(2)}(0) = 1 + \frac{2|\alpha|^2 [p - s \cos(\theta - 2\varphi)] + s^2 + p^2}{(|\alpha|^2 + p)^2}. \quad (2.56)$$

Having that the mean number of photons in the system can be expressed through the displacement and squeezing operators as given by equation (2.53):

$$n_{\text{tot}} = |\alpha|^2 + \sinh^2(r), \quad (2.57)$$

the expression for the second-order correlation function can finally be rewritten as

$$g^{(2)}(0) = 1 + \frac{2(n_{\text{tot}} - p)[p - s \cos(\theta - 2\varphi)] + s^2 + p^2}{n_{\text{tot}}^2}. \quad (2.58)$$

2.7 Conclusion

In this Chapter, we introduced several examples of the light field states. Probably the most common example in the optical research are the coherent states, which can be routinely generated by lasers. Much more effort is required to create the states with the field fluctuations surpassing the quantum noise limit. This makes generation and manipulation of squeezed and Fock states of the major interest for the quantum optics. The properties of these states of light can be accessed via the first- and second-order correlation measurements. The main aim of this thesis is to study the features of the light field emitted by microcavity polaritons via correlation measurements.

3 Sample fabrication and experimental techniques

As emphasized in Chapter 1, the research on the strong light-matter coupling of quantum well excitons to light relies on high-quality semiconductor microcavities. These can be fabricated by using the molecular beam epitaxy (MBE), a technique that allows the preparation of high-quality crystalline materials by depositing atomically thin layers one-by-one. The ability to control the growth speed, the material composition together with a low amount of defects makes MBE of crucial importance for manufacturing high-quality semiconductor heterostructures for optical applications and fundamental research.

The half-light half-matter nature of microcavity polaritons provides a unique opportunity to address them with light. This gives a handy ability to easily create and manipulate the polaritons with lasers tuned at an appropriate wavelength. Moreover, the low lifetime of the photonic component of polaritons means that they decay through one of the cavity mirrors, thus forming stream of photons that inherits such polariton properties as energy, polarization, momentum etc. Therefore, study of the emission of microcavities with standard optical tools like spectrometers, polarizers, fast photodiodes, and streak-cameras allows for an easy access to multiple polariton features. In this Chapter we will discuss the microcavity samples used for the research, and the general scheme for optical measurements.

3.1 Microcavity samples

The microcavity samples used for the experiments described in this thesis were grown by molecular beam epitaxy. This technique relies on creating the atomic fluxes of materials that deposit onto a crystalline substrate repeating its periodic structure. For example, sending

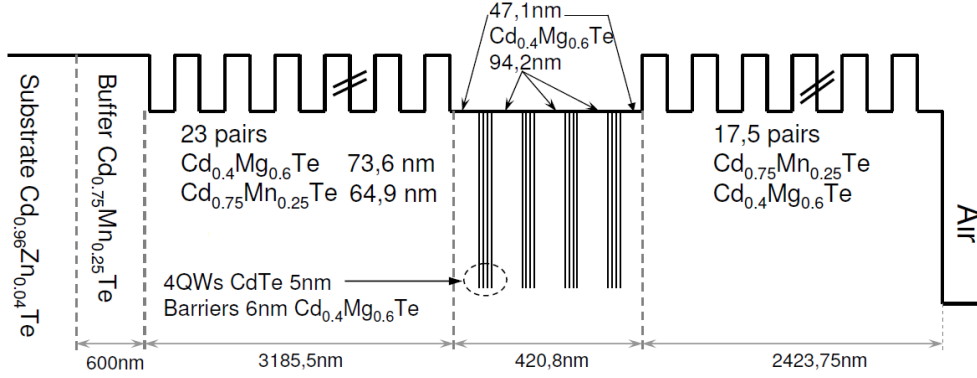


Figure 3.1: Sketch of the structure of the CdTe microcavity. The solid line represents variation of the refractive index in different layers of the structure. Adapted from [9].

fluxes of gallium and arsenic will allow the formation of crystalline GaAs, the thickness of which can be controlled by the flux of the different elements and time of deposition. More importantly, MBE allows for the creation of ternary solutions like $\text{In}_x\text{Ga}_{1-x}\text{As}$, where two different types of atoms with similar chemical properties (for example, In and As) occupy the same sublattice of the crystal. The concentration of indium x in the resulting material can be set by the ratio between the fluxes of indium and gallium. This allows for engineering the semiconductor heterostructures with layers of materials of well-controlled bandgaps, refractive indices and other physical properties, which is of crucial importance for manufacturing high-quality microcavities.

In the setup for the MBE growth, the fluxes of atomic components are optimized to cover the whole 2-inch substrate region during the growth. Nevertheless, some inhomogeneity of the fluxes can still be present. To reduce its effect, the substrate is rotated during the growth, thus providing rotational symmetry of the fabricated microcavity. At the same time, the flux in the center of the growth region is commonly higher than at the edges. This leads to variations of the microcavity thickness along the radius of the grown sample, an effect that is usually referred to as *the wedge*. Surprisingly enough, this effect is rather considered to be an advantage, because it leads to variation of the detuning along the sample radius, and allows for selecting a particular region of the microcavity for the experimental study.

Below, the semiconductor microcavities made of II-IV and III-V materials will be discussed. The II-IV CdTe microcavity was grown by Dr. Régis André in the group of Prof. L. S. Dang in Grenoble. The III-V GaAs microcavities with InGaAs quantum wells were grown by Dr. Fauzia Jabeen in our group in Lausanne.

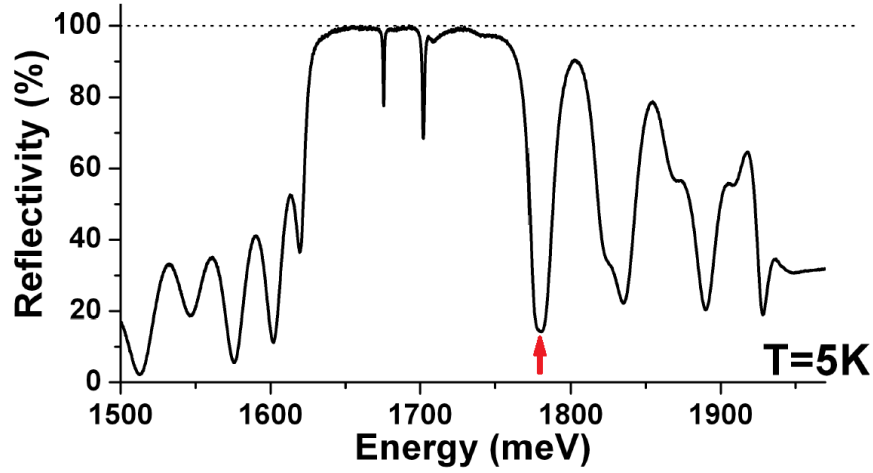


Figure 3.2: Reflectivity spectrum of the CdTe microcavity. Minimum of the reflectivity at $\lambda = 695$ nm can be used for the nonresonant excitation of polaritons. Reproduced from [9].

3.1.1 CdTe microcavity

The structure of the CdTe microcavity is presented in Figure 3.1. It starts with a $\text{Cd}_{0.96}\text{Zn}_{0.04}\text{Te}$ substrate blanketed with a 600 nm thick $\text{Cd}_{0.75}\text{Mn}_{0.25}\text{Te}$ buffer that covers the substrate defects and prepares the atomically flat surface for the subsequent growth. The microcavity by itself is formed by DBRs made of alternating layers of $\text{Cd}_{0.4}\text{Mg}_{0.6}\text{Te}$ and $\text{Cd}_{0.75}\text{Mn}_{0.25}\text{Te}$. The bottom and top DBRs contain 23 and 17.5 pairs of these materials, respectively. The microcavity spacer is made of $\text{Cd}_{0.4}\text{Mg}_{0.6}\text{Te}$ with an optical thickness of 2λ . Since the refractive index of the spacer is smaller than the one of the adjacent DBR layers, the electric field is zero at the edges of the spacer, and all 4 antinodes of the field are situated in the spacer. At the position of every field antinode, a stack of 4 CdTe quantum wells, each with a thickness of 5 nm, is situated. The inclusion of 16 quantum wells in total in the cavity first allows for a very large Rabi splitting, and second, reduces the exciton densities in the system, thus increasing the range of polariton densities at which strong coupling is still maintained.

The resulting exciton energy in quantum wells is $E_X = 1.6874$ eV, and the Rabi splitting is 26 meV, undoubtedly confirming realization of the strong coupling. This is clearly seen from the presence of two polariton modes in the reflectivity spectrum (Figure 3.2). For the detunings $\delta \approx 0$ meV the lower polariton emission is observed at $\lambda \approx 740$ nm. Since the substrate used for the sample growth was made of $\text{Cd}_{0.96}\text{Zn}_{0.04}\text{Te}$, it absorbs light at the wavelength of the lower polariton emission, making the sample not suitable for the transmission measurements.

The stopband of the microcavity covers the spectral region from 710 to 760 nm. The first

reflectivity minimum of the microcavity is situated at $\lambda = 695$ nm and is shown with an arrow in Figure 3.2. At this wavelength, the laser emission can enter the cavity and excite the electron-hole pairs in the quantum wells. The generated carriers then undergo phonon-assisted relaxation to the bottom of conduction band and top of the valence band, and form excitons that are accumulated in an excitonic reservoir at high wavevectors. The exciton reservoir then can populate the lower polariton branch through parametric or phonon-assisted scattering. The most dramatic feature of this particular microcavity is that, above a given excitation threshold, the ground state occupancy starts to be more than unity, thus forcing stimulated scattering of polaritons in the ground state and forming a Bose-Einstein condensation of polaritons [82, 45].

Another noticeable feature of the CdTe microcavity is significant photonic disorder. Despite the very high quality of the MBE growth, a certain amount of an internal stress due to the lattice mismatch between the different layers is still present. This stress leads to the fluctuations of the microcavity spacer thickness over the sample, and a subsequent change of the polariton potential. The characteristic lateral size of the potential fluctuations is of the order of few microns, and its depth is about 0.2–0.4 meV. The presence of this disorder led to numerous observations of intriguing phenomena, including formation of localized BECs and their synchronization [83], one-dimensional condensates [84], Josephson junctions [55], and pinning of quantum vortices to the defect potentials [58].

3.1.2 InGaAs microcavities

The variety of fabricated III-V microcavity samples with InGaAs quantum wells demonstrated the high reproducibility and perfect quality of the structures. Although showing no spontaneous BEC (which in fact has not been yet undoubtedly observed for InGaAs microcavities), the use of InGaAs quantum wells allows to reduce the bandgap in comparison to pure GaAs, and thus allow for the operation in transmission mode. Probably one of the most important difficulties for the growth of such samples is a more than a 7% lattice mismatch between gallium arsenide ($a_{\text{GaAs}} = 0.564$ nm) and indium arsenide ($a_{\text{InAs}} = 0.606$ nm) [31]. As a consequence, only the quantum wells with low indium fraction (less than 10%) could have high enough quality and low concentration of defects to be suitable for our studies.

The sample used in current work was grown on a GaAs substrate covered with a 1 μm thick GaAs buffer layer. The microcavity is formed by top and bottom DBRs containing 23.5 and

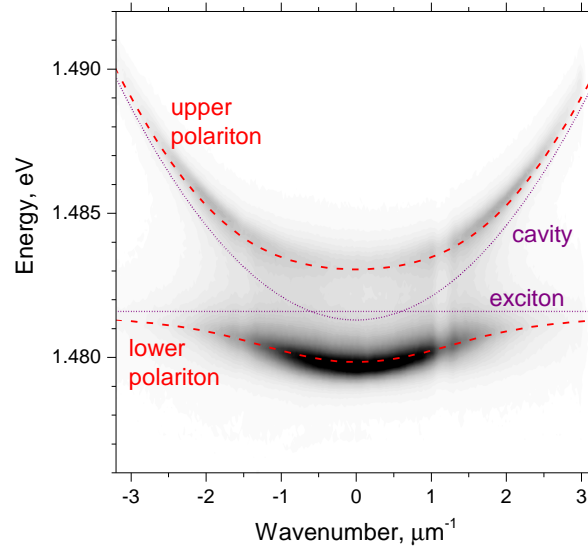


Figure 3.3: Emission of the lower and upper polariton in an InGaAs microcavity with a slightly negative detuning $\delta = -0.3$ meV. The Rabi splitting is 3.2 meV.

20 pairs of GaAs/AlAs, respectively, and a GaAs spacer with the optical length of λ . Since the refractive index of GaAs is bigger than the one of AlAs, the antinodes of the cavity field were situated both in the middle of the spacer and at its interfaces. A single 10 nm $\text{In}_{0.06}\text{Ga}_{0.94}\text{As}$ quantum well was situated in the middle of the spacer, at the position of the antinode of the electric field.

The resulting exciton energy was $E_X = 1.482$ eV, thus giving rise to the lower polariton emission at the wavelength of about 840 – 850 nm depending on the detuning (Figure 3.3). The Rabi splitting of the samples was close to 3.2 meV. The emission spectrum of the upper and lower polaritons at slightly negative exciton-photon detuning is presented in Figure 3.3.

3.1.3 Mesa fabrication

Planar microcavities favor the motion of polaritons in the plane perpendicular to the growth direction, thus making them a bright example of an artificial two-dimensional system. At the same time, the number of degrees of freedom can be further reduced if one creates some potential traps for polaritons in the plane of the microresonator. Numerous techniques have been proposed for the polariton confinement in planar microcavities, most of which exploit various ways of its post-processing, for instance gold patterning of the sample surface [16], use of surface acoustic waves [18], ion etching of the microcavity [17], and even application of

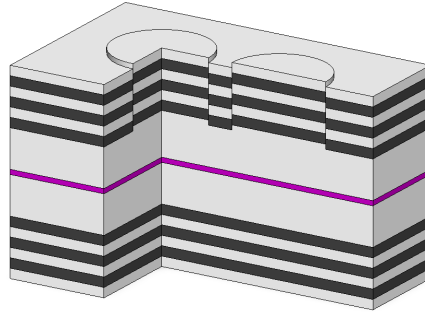


Figure 3.4: Sketch showing the microcavity with two round mesas.

a local strain [46]. Another possibility relies on the sample processing during the fabrication, where the spacer thickness can be varied in different areas of the microcavity. The principle of operation of these *mesas* is based on the simple fact that the longer spacer supports a cavity mode having longer wavelength, leading to the decrease of the energy of the polariton states [15]. The microcavity with mesas schematically depicted in Figure 3.4 represents a robust and easy-to-use design, which allows for the creation of potentials of arbitrary geometries, thus opening the road towards the study of polaritons in 0D and 1D geometries.

The main complexity of this type of microcavities is that the mesas are fabricated by etching of the unwanted areas of the spacer, implying that the MBE growth should be interrupted before depositing the top mirror, and the sample should be taken out of the MBE machine for the processing. This irrevocably leads to a reduction of the surface quality of the sample and to the appearance of defects in the microcavity. Therefore, it was highly important to develop a mesa etching process that does not lead to dramatic formation of surface defects, and ensure that there are no remnants of chemical materials on the surface before the MBE growth is restarted. Practically, it took significant amount of time and numerous tests on the photolithography, chemical etching, and surface cleaning in order to optimize the fabrication process and have good quality factor of the mesa samples. The protocol for the sample processing described below was developed jointly with C. Ouellet-Plamondon and relied on the standard wet chemical etching of the semiconductors.

The main steps of the fabrication of the mesa samples are schematically depicted in Figure 3.5. The MBE growth is interrupted after accomplishing the first half-cavity, which consists of the bottom DBR, the spacer with embedded quantum well, and the *etchstop*. The latter comprises ≈ 1.8 nm of AlAs (6 monolayers) and 6 nm of GaAs on top of it, and it should be removed by the wet chemical etching during the mesa fabrication. The half-cavity is taken out of the MBE

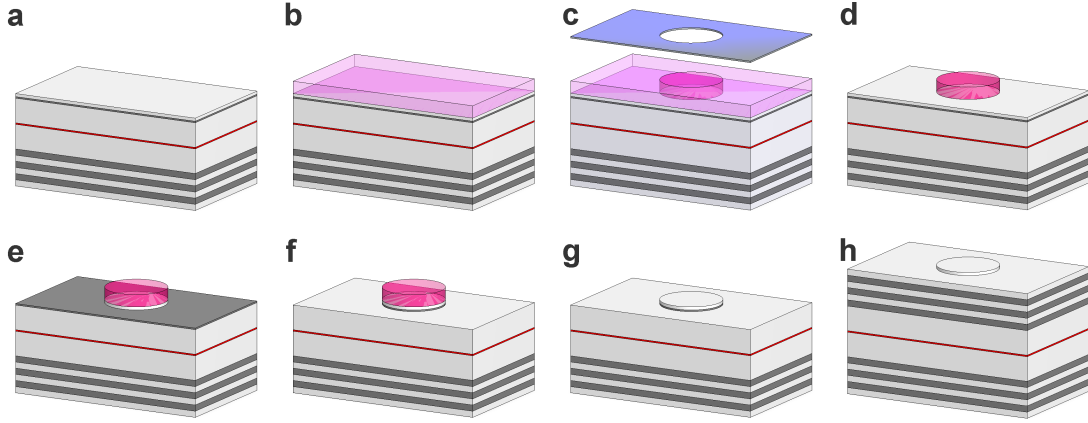


Figure 3.5: Fabrication of the mesa samples. (a) MBE-grown half-cavity, (b) photoresist deposition, (c) photoresist exposition through the patterns in the mask, (d) development of non-exposed photoresist, (e) wet etching of GaAs, (f) oxidation and wet etching of AlAs, (g) removal of the photoresist, (h) MBE growth of the top DBR.

machine and undergoes a standard photolithography process. For this, it is spin-coated with an S1805 photoresist up to the thickness of 500 nm, exposed with a UV lamp through the mask with desired patterns, and finally, processed in an MF319 developer to remove the exposed resist. The timings of spin-coating, exposure, and development depend on the precursors and equipment used, and generally speaking, they have to be optimized for a particular process.

Next, two selective chemical etchants are used to remove first GaAs, and next AlAs layers that are not covered by the photoresist. For etching of GaAs, a 1:500 $\text{NH}_4\text{OH}:\text{H}_2\text{O}_2$ solution is used, which does not affect the AlAs layer. Etching is performed for 15 seconds, and during this time the solution is stirred in a magnetic stirrer at 700 rotations per minute. After rinsing in water, the sample is left in air for 3 minutes to oxidize the AlAs layer, which is then removed by dipping the sample into 1:1 $\text{HCl}:\text{H}_2\text{O}$ solution for about 1 second. Oxidation of AlAs is a critical step, because the chemical reaction between AlAs and HCl is very active and usually leads to major damaging of the sample surface. This was nicely visualized during the optimization of the etching procedure on GaAs/AlAs DBRs, as shown with a scanning electron microscope (SEM) image in Figure 3.6a. The active chemical reaction between non-oxidized AlAs and HCl produces the through holes in the underlying layer of GaAs, so that the acid was even able to etch the next layer of AlAs and cause a collapse of the GaAs layer.

Finally, the sample surface is cleaned from the photoresist in 1165 photoresist removal at a temperature of 60 °C for 10 minutes. After this step, the sample is cleaned in the hydrogen plasma etching chamber, and then transferred under vacuum chamber into the MBE machine.

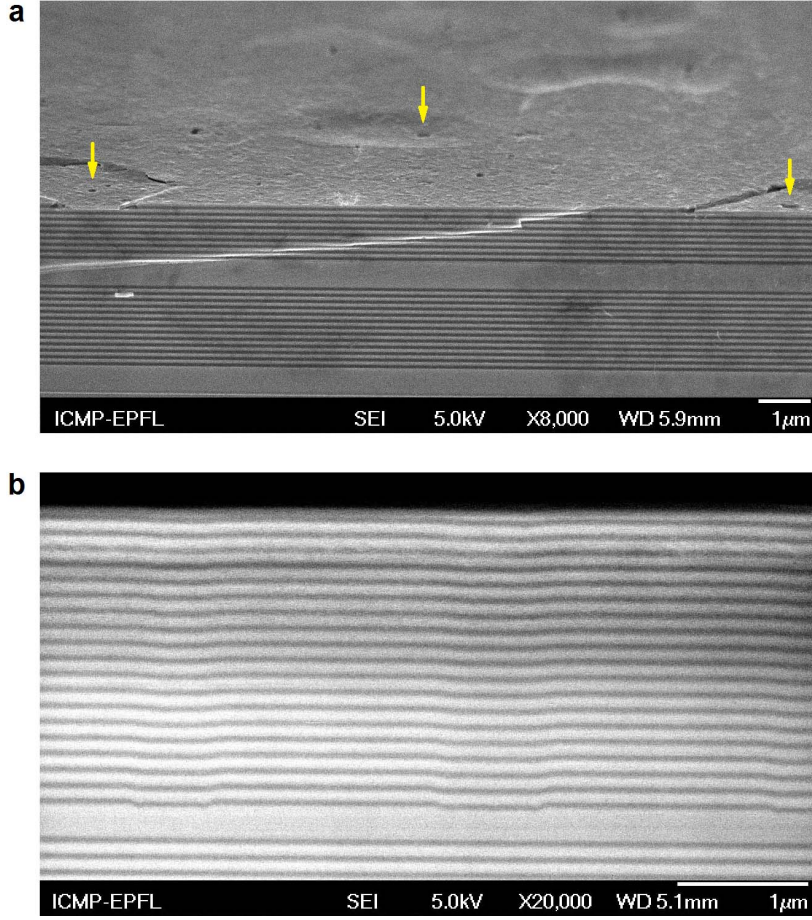


Figure 3.6: (a) Surface damage of the test sample due to reaction of non-oxidized AlAs with HCl. Active reaction creates the holes in the layer of GaAs (yellow arrows). HCl penetrates through the holes and dissolves the underlying layer of AlAs, causing collapse of the top GaAs layer. (b) Cleavage of a finished microcavity. Multiple mesas with the height of 20 nm are clearly seen.

This ensured a high surface quality before the growth of the second DBR and therefore allows the realization of a high-quality microresonator. The SEM image of the cleavage of one finished microcavity with mesas is shown in Figure 3.6b. For this image, the height of the GaAs layer in the etchstop was increased from 6 nm to 20 nm, which made it possible to clearly observe the mesas.

The spectrum of the mesa emission under nonresonant CW excitation is presented in Figure 3.7. The mesa of the height 6 nm results to the confining energy of the photonic mode $\Delta E_C = 9$ meV (white dashed line in Figure 3.7b). This confinement causes quantization of the photonic mode, leading to formation of distinct confined energy states. Each of those

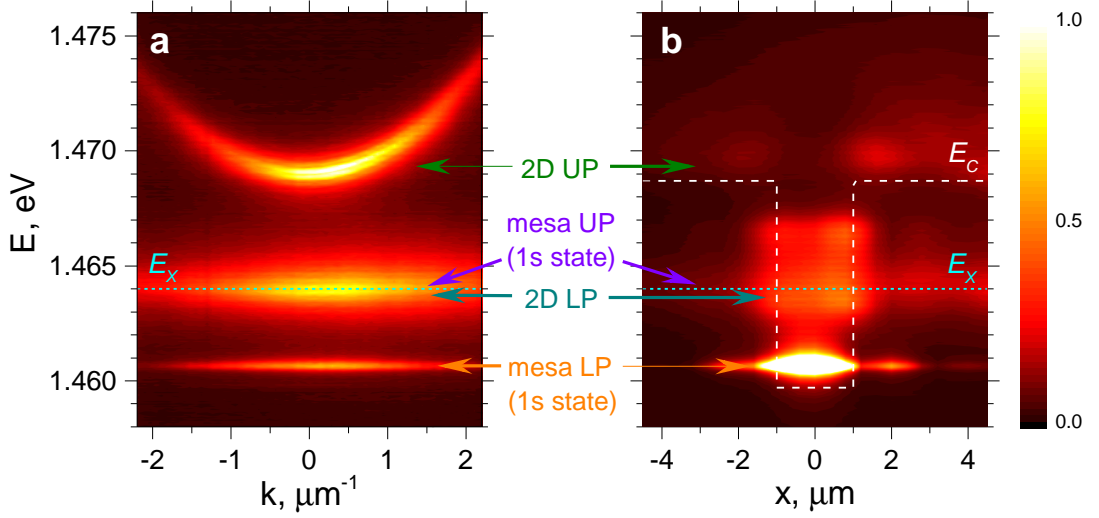


Figure 3.7: Spectrum of a round $2\ \mu\text{m}$ mesa in (a) reciprocal space, and (b) real space. The spectral features corresponding to the upper and lower polaritons (UP and LP) in the mesa and in 2D planar microcavity surrounding the mesa are shown with arrows. For the mesa, only the polaritons arising from the lowest (1s) quantized photonic state are shown. White dashed line in (b) shows the photonic potential that confines the light in the mesa and leads to emergence of quantized energy states. Cyan dashed line in (a) and (b) shows the energy of the exciton E_X in the quantum well.

states is subsequently coupled to the excitonic dipole, giving rise to formation of the confined polariton modes [85]. Particularly, the lower polariton state with the lowest energy appears at $E = 1.4605\ \text{eV}$ and features strong luminescence. The corresponding confined upper polariton emission appears close to the exciton energy at $E_X = 1.464\ \text{eV}$. Other confined photonic states have the energy higher than E_X , and therefore give rise to the lower polariton emission close to E_X , and upper polariton emission being few meV higher (confined states at $E \approx 1.467\ \text{eV}$ in Figure 3.7b). At the same time, the 2D photonic mode in the planar cavity around the mesa is also coupled to the exciton. Due to the positive detuning $\delta = +4.5\ \text{meV}$, it demonstrates a close to parabolic dispersion of the upper polariton (Figure 3.7a), and lower polariton emission outside the mesa region with the energy close to E_X (Figure 3.7b).

Under nonresonant excitation, the emission of the confined polaritons is broadened due to the interactions, and cannot provide any information about the quality factor of the microcavity. However, we have studied the exponential decay of the luminescence after a pulsed resonant excitation, and found the polariton lifetime to be $\tau = 5.2\ \text{ps}$. This allows us to calculate the quality factor of the cavity to be $Q \approx 11\ 000$.

3.2 Experimental techniques

The light-matter nature of microcavity polaritons provides a unique opportunity to both create and measure the state of the system using conventional free-space optical tools. As a consequence, the polaritonic system can be excited using a laser excitation with arbitrary chosen wavelength, intensity, polarization etc. On the other hand, the microcavity emission acts as a non-demolishing probe of the system, inheriting properties of the polaritons within the microcavity, and can be routinely studied using imaging techniques, spectroscopy, time-resolved measurements, and other tools to characterize the light features.

3.2.1 General excitation and detection scheme

The experimental layout used for excitation of the microcavity and detection of its emission is presented in Figure 3.8. The excitation scheme starts with a Coherent Verdi-V18 laser, that consequently utilizes two high-power laser diodes pumping the Nd:YAG laser head at $\lambda = 1064$ nm, and a subsequent second-harmonic generation to produce coherent emission at $\lambda = 532$ nm with an output power of 18 W. This emission is used to pump two Ti:Sapphire lasers, the wavelength of which can be tuned. The first one pumped with 10 W at $\lambda = 532$ nm is a mode-locked Spectra-Physics Tsunami laser with a broadband mirror set. It produces pulses with duration of $t \approx 300$ fs at a repetition rate of 80.5 MHz with the wavelength tunable in the range 690–880 nm and the mean output power 0.3–1.5 W depending on the wavelength. The second is a continuous-wave (CW) Coherent MBR-EL monomode laser possessing high output intensity stability and emission linewidth of few MHz only. The output wavelength of this laser can be tuned within the range 695–795 nm. The cavity of this laser has an active feedback system to stabilize the operating wavelength and prevent the mode hopping. The emission of the CW laser is modulated with an acoustooptic modulator (AOM) at a period of 500 Hz and a duty cycle 2.5–10 percents in order to reduce the thermal heating of the microcavity sample. The spatial mode of both lasers is cleaned through the spatial filters, which are simply the optical telescopes made of two lenses and a pinhole placed in between, at the focal planes of both lenses.

The microcavities are held in a helium-flow cryostat (Oxford Microstate He) at the temperature 5.0–5.1 K allowing to optimize the consumption of liquid helium for long experiments. To get the optical access to the sample from both top and bottom DBR, the cryostat is placed between two microscope objectives. We use infinity-corrected objectives since this create

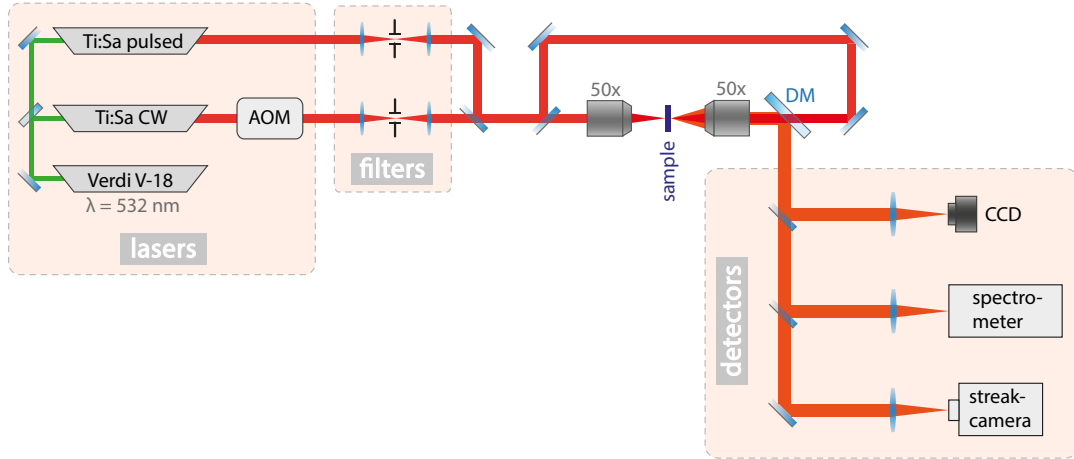


Figure 3.8: Sketch of the experimental setup. CW or pulsed laser can be focused on either side of the microcavity. The emission is collected from the top DBR of the microcavity and can be studied by a CCD, spectrometer, or a streak-camera.

collimated laser beams and do not require adjustment of the imaging systems if one inserts optics (polarizers, beamsplitters etc.) in the beam path. The objective used for the detection of the microcavity emission and resonant excitation is 50x Mitutoyo Plan Apo NIR, optimized for operation in the near infrared spectral region and having a numerical aperture $NA=0.42$. The objective used for excitation in transmission geometry is 50x Olympus LMPlanFLN with $NA=0.5$. One can redirect the laser beam to either of the objectives in order to excite the sample from the top or bottom DBR. For the excitation of a small area of the sample, the collimated laser beam is directed right in the objective, thus creating a spot with a size of about $3\ \mu\text{m}$ on the microcavity. If one wants to excite a large sample area, the laser is passed through an additional lens with a focal plane coincident with the back Fourier plane of the objective. This reduces the laser spot size in the Fourier plane of the objective, and consequently increases the real-space beam size. Depending on the focal distance of this lens, the excitation spot size may be adjusted between 10 and $25\ \mu\text{m}$.

The detection of the microcavity emission is always performed from the top of the microcavity, because of the lower thickness of the top DBR, and thus higher emission intensity in this direction. The emission is collected by the Mitutoyo objective and sent to a Thorlabs M254H45 dichroic mirror, which is transmitting the light with wavelength $\lambda < 700\ \text{nm}$, and reflecting the one with $\lambda > 700\ \text{nm}$. This allows to pass the excitation laser through this mirror, while more than 99% of the microcavity emission (at $\lambda = 740\ \text{nm}$ for CdTe or $\lambda = 840 - 850\ \text{nm}$ for InGaAs) is reflected to the side. The reflected emission is focused with a 400 mm lens on the

CCD camera for real-space imaging (Sony XC-EC50), a spectrometer, or a streak-camera, thus giving total magnification of $\Gamma = 100$. We use an ANDOR Shamrock spectrometer with focal length 750 mm equipped with 600 l/mm and 1800 l/mm gratings, and an ANDOR Newton 2D camera for imaging. The spectral resolution of the spectrometer with 1800 l/mm grating reaches $60 \mu\text{eV}$. For time-resolved measurements, a Hamamatsu C5680 streak-camera with an S25 photocathode optimized for the use in near infrared spectral region, and Hamamatsu ORCA-R2 CCD is utilized. The time resolution of this streak-camera can reach 2.2 ps.

The emission of the sample may also be detected in the reciprocal state. For this, an additional lens with a focal plane coinciding with the back Fourier plane of the objective is used. After this lens, the light propagating at different angles corresponds to the different wavevectors in reciprocal space, and hence the reciprocal space is imaged onto the detector plane. In our experiments, the focal length of the reciprocal imaging lens is $f = 400$ mm. Particularly, the use of the reciprocal space imaging with a spectrometer is necessary for accessing the polariton dispersion curve, like the one shown in Figure 3.3.

3.2.2 Spectral and temporal tomography

When the spectral measurements are performed, the real- or reciprocal-space image of the microcavity emission is focused on the plane of the entrance slit of the spectrometer. The narrow slit lets the light along a certain vertical line to enter the spectrometer, as it is shown in Figure 3.9. The input slit image is decomposed into the spectrum and recorded by the 2D camera, thus giving information about the spectrum at every point along the input slit.

Clearly, the information about the emission that does not enter the spectrometer slit is lost. If one wants to measure the spectrum along another slice of the emission, the corresponding area has to be focused on the entrance slit. By subsequently focusing the vertical lines on the slit one-by-one, we can finally get the spectrum for any points of the emission. This technique is called a *spectral tomography* and is schematically illustrated in Figure 3.9.

In our setup, the tomography is performed by moving the imaging lens in front of the spectrometer, which allows to shift the image with respect to the entrance slit. For convenience it can be easily automatized by using a computer-controlled translation stage for the lens. Particularly, in our experiment a Thorlabs Z812 actuator is used, and its motion together with the spectrometer operation is controlled by a LabVIEW script.

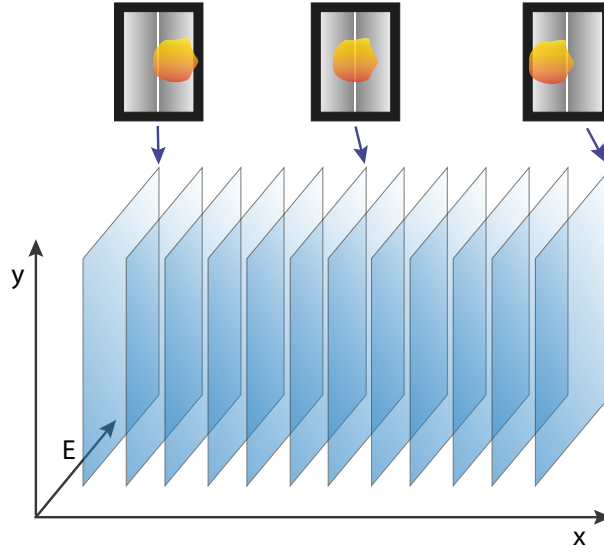


Figure 3.9: Principle of the spectral tomography. Shift of the imaging lens allows to focus different parts of the image on the entrance slit of the spectrometer. As a result, the spectrum at every point of the image can be acquired.

Absolutely the same technique can be implemented for a *temporal tomography* using the streak-camera. The only difference is the orientation of the entrance slit, which is vertical for the spectrometer, but horizontal for the streak-camera. Therefore, the lens for the spectral tomography is translated in horizontal direction, while the one for temporal tomography moves in the vertical direction.

3.2.3 Interferometry

The study of the first-order spatial coherence of macroscopic coherent states requires the use of the interferometric techniques, where the emission from two arbitrary parts should be mixed in order to observe the interference patterns. In our setup, we implement the Michelson interferometer, where a beamsplitter is used to split the input stream of light into two beams, which are then overlapped on the same beamsplitter. If the input light is coherent, the overlapping beams will form an interference pattern, and the orientation and density of interference fringes will depend on the angle between the wavefronts of two beams. The contrast of the fringes and their intensity can thus give access to the degree of coherence and the phase relations within the light stream.

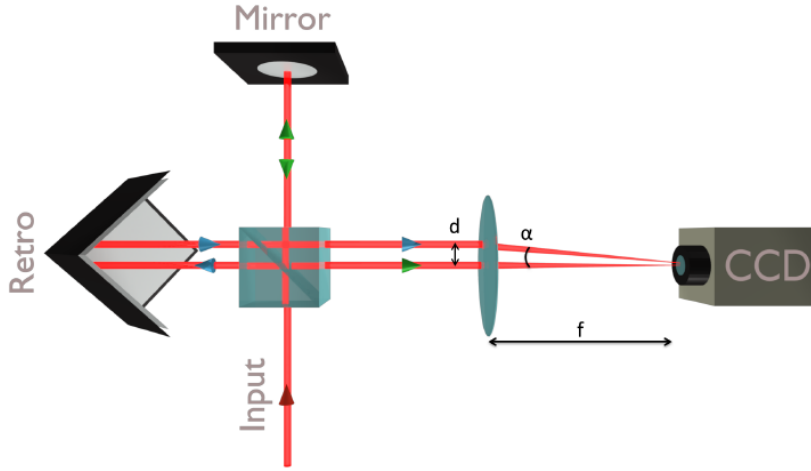


Figure 3.10: Michelson interferometer in the mirror-retroreflector configuration. The shift of the retroreflector defines the separation between two beams, the angle between their wavefronts after the lens, and hence the density of the fringes on the interference pattern. Reproduced from [86].

We use the Michelson interferometer in a mirror-retroreflector configuration, which is known for its ability to precisely control and adjust the shape of the interference pattern. The schematic image of the interferometer is given in Figure 3.10. The retroreflector is essentially a set of three flat mirrors placed at the right angle between each other, thus forming an inner corner of a cube. Its main feature is that the reflected beam is always parallel to the input one, no matter what is the angle of the incidence. At the same time, the motion of the retroreflector perpendicularly to the incident beam allows to change the position of the reflected one. Therefore, after an imaging lens placed at the output of the interferometer, the tilt of the beam can be controlled by the position of the retroreflector. Particularly, if the retroreflector is moved by a distance $d/2$ from the optical axis, the beam in this arm will move by d , and after the imaging lens with the focal distance f it will have a tilt of $\theta = \arctan(d/f)$ in respect to the optical axis. Together with the fixed position of the beam in the second interferometer arm, this allows to control the orientation and density of the interference fringes by simply translating the retroreflector.

One should note that the motion of the retroreflector does not tilt the light beam, and hence does not displace the image in the focal plane of the imaging lens. On the other hand, the retroreflector inverts the orientation of the input light beam, thus creating an inverted real-space image in the focal plane of the imaging lens. Therefore, the interferometer allows to overlap the real-space image of the microcavity (mirror arm) with a centrosymmetric replica

of itself (retroreflector arm). Two images coincide only at an *autocorrelation point*, which can be used as a beginning of the reference frame in the image plane. In other words, the interference pattern measures the interference between the points \mathbf{r} and $-\mathbf{r}$, where the vectors are defined in respect to the autocorrelation point. If the light field in the focal plane defined by the mirror arm is $A(\mathbf{r})e^{i\varphi(\mathbf{r})}$, then the intensity of the interference pattern at the position \mathbf{r} is

$$I_{\text{int}}(\mathbf{r}) = |A(\mathbf{r})|^2 + |A(-\mathbf{r})|^2 + 2A(\mathbf{r})A(-\mathbf{r})\cos(\mathbf{k} \cdot \mathbf{r} + \varphi(\mathbf{r}) - \varphi(-\mathbf{r}) + \varphi_0)g^{(1)}(\mathbf{r}, -\mathbf{r}), \quad (3.1)$$

where $|\mathbf{k}| = \sin(\theta) \approx d/f$, φ_0 is the phase offset between two interferometer arms, and $g^{(1)}(\mathbf{r}, -\mathbf{r})$ is the first-order coherence function. The fringes have the maximal contrast for $g^{(1)} = 1$, and it will decrease while decreasing $g^{(1)}$. From equation (3.1), the first-order coherence can be accessed if the field intensities in both arms $I_1(\mathbf{r}) = |A(\mathbf{r})|^2$, $I_2(\mathbf{r}) = |A(-\mathbf{r})|^2$ are measured:

$$I_f = g^{(1)}(\mathbf{r}, -\mathbf{r})\cos(\mathbf{k} \cdot \mathbf{r} + \varphi(\mathbf{r}) - \varphi(-\mathbf{r}) + \varphi_0) = \frac{I_{\text{int}}(\mathbf{r}) - I_1(\mathbf{r}) - I_2(\mathbf{r})}{2\sqrt{I_1(\mathbf{r})I_2(\mathbf{r})}} \quad (3.2)$$

The function I_f can obtain any values between the maximum $I_f^{\text{max}} = g^{(1)}$ and minimum $I_f^{\text{min}} = -g^{(1)}$ depending on the cosine term. In principle, by smoothly changing the phase offset φ_0 one could change the value of cosine term from -1 to 1, and thus measure $g^{(1)}$ from the maximal and minimal values of I_f . Experimentally this can be accomplished if one records the interference patterns for a set smoothly increasing values of φ_0 , thus performing a *phase tomography* of the interference pattern.

3.2.4 Interferometer stabilization and phase tomography

From the practical point of view, the interferometer is very sensitive to any small fluctuations of air in its arms or vibrations of the optical table. They unavoidably affect the phase offset φ_0 between two arms, introducing the phase noise and thus reducing the precision of measurements. To have the control on the phase of the interferometer, one can implement an active stabilization of it. This approach utilizes an extra laser beam that is sent on the input of the interferometer, this forming an interference pattern at the output, and one fringe of this pattern is permanently monitored by e.g. a small photodiode. The signal from the photodiode is sent to the feedback electronics that controls the position of the mirror in the interferometer arm by a mean of a piezo element. The feedback electronics maintains the

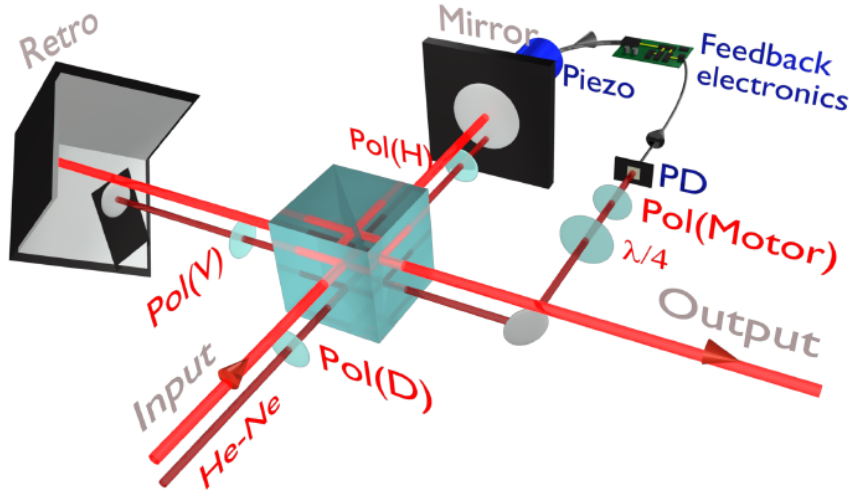


Figure 3.11: Active stabilization of the Michelson interferometer. The He-Ne laser beam used for the stabilization (thin) is situated below the signal of the microcavity emission (thick). The stabilization signal is monitored by the photodiode (PD) and through the feedback electronics adjusts the mirror position. Pol(D), Pol(V), Pol(H): diagonally, vertically, and horizontally oriented polarizers; Pol(Motor): polarizer on a motorized stage. Reproduced from [86].

photodiode signal at the same level by adjusting the piezo position, thus ensuring that the path difference between two interferometer arms is kept constant. The active stabilization thus provides robust and easy-to use tool to maintain the stability of the interferometer over long periods of time.

The main drawback of the abovementioned approach is that the phase difference φ_0 cannot be controlled at will. This obstacle is overcome by the scheme proposed in [87], where a control of polarizations is utilized in order to set the desired value of φ_0 . The scheme as it is implemented in the experiment is schematically presented in Figure 3.11. In order to not overlap with the microcavity emission that is studied, all the optics and the beam path for active stabilization in our experiment was situated 13 mm lower than the main optical axis.

The scheme starts with a diagonally linearly polarized monomode He-Ne laser, which is split on the beamsplitter and passed through the polarizers, making its emission vertical in one arm and horizontal in the other. The diagonal polarization of the laser ensures that the beams in two arms will have equal intensities. In the retro arm, the beam is reflected by an additional tiny mirror mounted on the retroreflector holder. After being reflected, the two beams are superposed again on the beamsplitter and then pass through the $\lambda/4$ waveplate. The waveplate turns the horizontal and vertical polarizations of two beams into the left- and

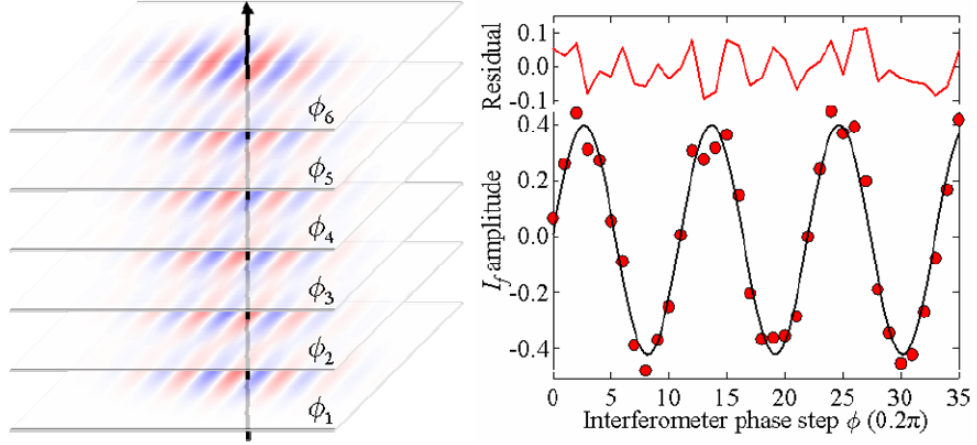


Figure 3.12: Left side: interference patterns for six different phase offsets between the interferometer arms. Right side: fit (black solid line) of the experimentally measured values of I_f for different ϕ (red circles). By fitting $I_f(\phi)$ for every point of the acquired image, one can reconstruct the two-dimensional map of the first-order coherence function $g^{(1)}$. Reproduced from [88].

right-circular ones. Being superposed on top of each other, two beams give rise to a linear polarization, the direction of which depends on the phase difference φ_0 , and the intensity is constant.

As a result, we can directly link the orientation of polarization to the phase difference φ_0 . To control the latter, one can pass the beam through a polarizer, and then detect it with a photodiode connected to the feedback system. The intensity of the light after the polarizer reads

$$I = 2I_0 \cos^2\left(\frac{\pi}{4} + \frac{\varphi_0}{2} + \varphi_{\text{pol}}\right), \quad (3.3)$$

where I_0 is the light intensity in each arm, and φ_{pol} is the tilt angle of the polarizer. Since the active stabilization is keeping the value of I constant, the turn of the polarizer by an angle $\Delta\varphi_{\text{pol}}$ changes the phase offset between the interferometer arms by $\Delta\varphi_0 = 2\Delta\varphi_{\text{pol}}$. Therefore, simple step-by-step turn of the polarizer allows to change the phase offset φ_0 , and thus perform a phase tomography.

For the active feedback, we use a Stanford Research SIM960 proportional–integral–derivative (PID) controller with parameters adjusted for the geometry of the system. The polarizer tilt angle is controlled by Thorlabs PRM1 motorized stage, thus allowing for the computer-

controlled phase tomography measurements. Nevertheless, even use of the active stabilization cannot completely suppress the phase noise. Therefore, the data are processed as follows. For every image position \mathbf{r} and every phase offset φ_0 , the value I_f is calculated according to equation (3.2). Next, for every position \mathbf{r} , the function $I_f(\varphi_0)$ is fitted with a cosine (Figure 3.12). The amplitude of the cosine gives the value of the first-order correlation function $g^{(1)}$.

Finally, one should emphasize that the phase tomography technique can be applied not only to the real-space images of the interference patterns. One can also retrieve the information about coherence by analyzing the images obtained by the spectrometer or the streak-camera, thus allowing to study the coherence at certain energy positions, or evolution of the coherence in time [89, 90]. Particularly, expansion of the coherence during formation of the polariton BEC will be discussed in Chapter 5 of this thesis.

4 Ultrafast second-order correlation measurements

As discussed in Chapter 2.4, traditional second-order correlation measurements are performed using the Hanbury Brown and Twiss setup. It consists of a 50:50 beamsplitter that splits the studied light into two parts, and two receivers capable to detect single photons in both arms. Nowadays, the role of the single photon detector is usually played by the avalanche photodiodes (APDs), the best of which have the time resolution of about 50–100 ps. This resolution can be improved by more than an order of magnitude by using a streak-camera. At the same time, it can also operate as a single photon detector thanks to the microchannel plate. In this Chapter, we describe the setup that was assembled for ultrafast second-order correlation measurements with a streak-camera, and discuss the requirements and limitations for the experiments with it.

4.1 Overview

The second-order correlations in polariton BECs were studied under both pulsed and CW nonresonant excitation [91, 92, 93]. Particularly, when crossing the condensation threshold, a decrease of the photon bunching [91], as well as change of a coherence time [91, 92] were reported. Nevertheless, it is necessary to emphasize that polaritons possess high mobility [94], high speed of sound [10], fast interactions with the excitonic reservoir [56], and low lifetime of about ~ 10 ps due to their photonic component. As a consequence, the polariton dynamics occurs on a picosecond timescale. Such fast changes of the polariton properties simply cannot be traced by the APDs, which have resolution of an order of 100 ps. Indeed, this was an obstacle that prevented accessing of the initial thermal statistics of noncondensed polaritons with $g^{(2)}(0) = 2$.

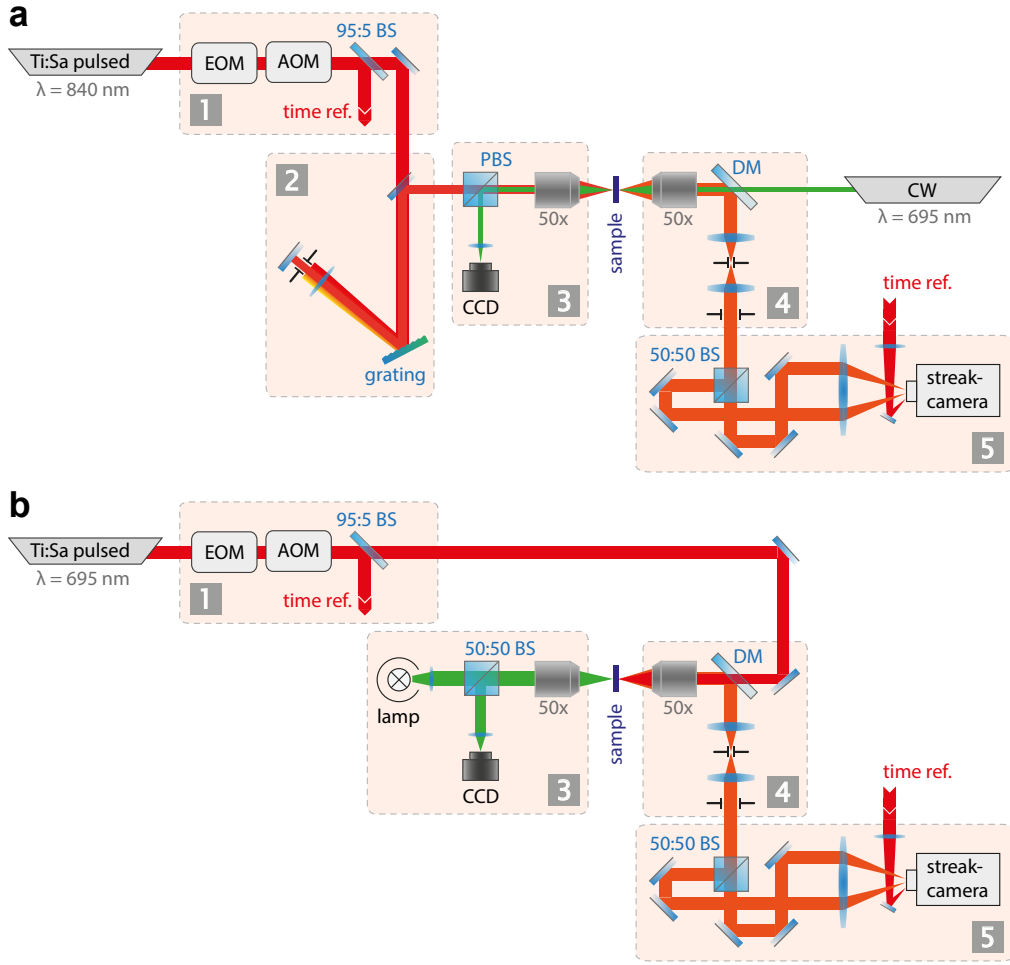


Figure 4.1: Setup for the ultrafast second-order correlation measurements in (a) transmission and (b) reflection geometry. Enumerated sections of the setup are: 1 – pulse picker, 2 – pulse shaper, 3 – active sample stabilization, 4 – sample imaging and real/reciprocal space filtering, 5 – HBT scheme and single photon counting. DM is a dichroic shortpass mirror with a cutoff wavelength of 710 nm.

The revolution in the time-resolved second-order correlation measurements was performed with a use of an alternative type of detector, namely the streak-camera in a single photon counting mode [27, 28]. With a resolution being about 2 ps, lower than the characteristic lifetime of a polariton system, this allowed to access the change of the emission statistics from thermal to Poissonian at the threshold of polariton condensation [28]. High temporal resolution is also favorable for measurements of the time resolved statistics of photocounts, which has been reported for instance for quantum dot microresonator lasers [95]. In this Chapter, an alternative configuration of the setup for ultrafast light statistics measurements, suitable for study of extended polaritonic systems, is described.

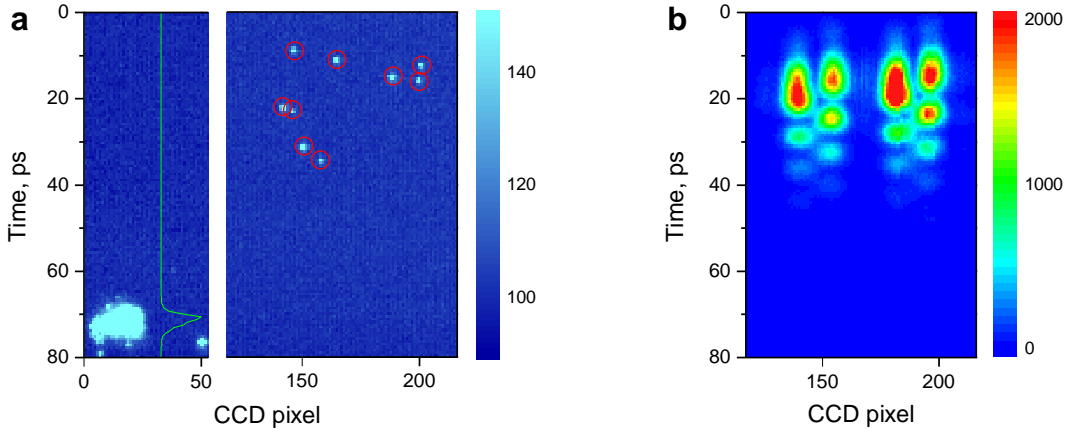


Figure 4.2: Second-order correlation measurements. (a) One frame with single photon counts and time reference laser acquired by the streak-camera. Single photons detected by the software are marked with red circles. Temporal profile of the reference laser is shown in green. (b) Integrated image formed by summing up single photons detected in 300 000 frames.

4.2 Ultrafast second-order correlation measurements

The setup used for the second-order correlation measurements was based on the C5680 streak-camera with an S-25 photocathode. Even though the very idea of the single-photon counting using a streak-camera was similar to the pioneering experiments [27, 28, 96], the setup in this experiment was tailored to meet specific demands for accessing the properties of the polaritonic systems. One of the main requirements was an ability to study the statistics of the extended polariton population, which implies that the streak-camera should provide sufficient real-space resolution. Another important aspect of the system was its ability to study the microcavity emission at low occupation requiring long experimental times, during which the stability of the system should be maintained. The main improvements of the single photon counting system that allowed us to fulfill both requirements are summarized below.

Laser pulse picking. The idea of the time resolved second-order correlation function measurements implies that the correlations are only calculated between the photon counts arriving only from the same laser pulse. Different laser pulses (and the polariton dynamics that they launch) are essentially uncorrelated. In order to be used with the streak-camera operating in the synchroscan mode (this means that the sweep voltage is applied in phase with the laser pulses, at the repetition rate of 80.5 MHz), this requires an additional technique that prevents the emission after different laser pulses be mixed with each other.

In [96], a horizontal sweep of the streak-camera was used to make the different laser pulses arrive at different position on the X-axis of the streak tube phosphorescent screen. Being clearly an evident and easy-to-use way of separating the laser pulses, this approach has a disadvantage for studying the emission of large or spatially inhomogeneous regions of the sample. It comes from the fact that the horizontal sweep cannot take less than 50 ns for the whole screen. This means that two adjacent images cannot be separated by more than 240 pixels (CCD width is 1024 pixels) or, accounting for the parameters of the imaging setup, 20 μm of the real-space image. Therefore, the polariton luminescence coming from the region more than 20 μm can overlap with each other on the streak-camera screen. If the magnification of the imaging setup is reduced, one would also reduce the spatial resolution for studying the inhomogeneous light (e.g. polariton emission from few potential traps close to each other).

In our setup, separation of different laser pulses is performed not after the microcavity sample, but before it. It is realized by selecting only one single laser pulse out of train of pulses generated by the mode-locked laser. This single laser pulse excites the microcavity sample, and the polariton emission after one single pulse is studied. The main idea is that during one acquisition frame of the streak-camera, only the light coming from this *single shot* reaches the camera. Hence, the repetition rate of this system is defined by the frame rate of the CCD used to image the phosphorescent screen of the streak-tube, which can change in our case between 45 and 85 Hz.

In this configuration, the streak-camera CCD triggers the pulse picker that selects a single laser pulse during the CCD acquisition time. For this, the emission of the mode-locked laser passes subsequently through a Fastpulse 5046SC-1/4 electro-optic modulator (EOM) and an IntraAction AOM-802N acousto-optic modulator (AOM), which are shown in section 1 of Figure 4.1. The EOM passes only one laser pulse, blocking all the others with an extinction ratio better than 10^3 . Subsequently, the AOM completely dampens all of the attenuated laser pulses outside the time window of $\approx 2.5 \mu\text{s}$.

Use of the Hanbury Brown and Twiss setup. Real-space imaging of the condensate with the streak-camera can be combined with the traditional HBT scheme for the second-order correlation measurements. In this configuration, the photon stream is split into two parts on a 50:50 beamsplitter, and both paths are imaged alongside each other on the streak-camera entrance slit (section 5 in Figure 4.1). To keep the distance of both paths equal, a set of mirrors is used, two of which are installed on a translation stage so that fine adjustment of the length of two paths can be performed.

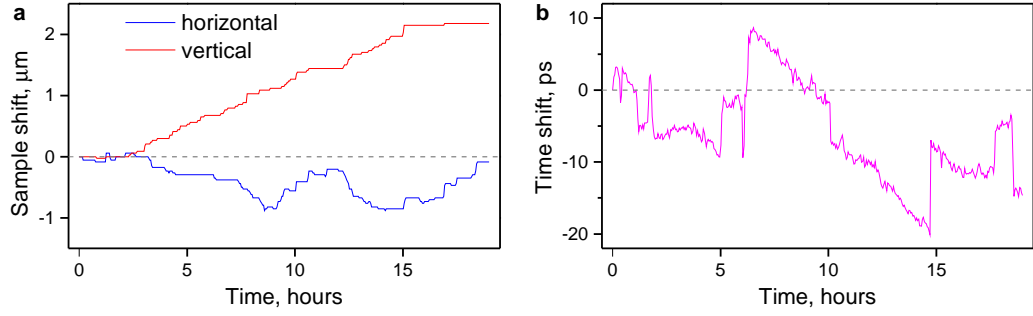


Figure 4.3: (a) Performance of the active sample stabilization in XY-plane. (b) Movement of the streak-camera time axis position during the experiment.

Use of the HBT scheme is very practical to prevent errors while reconstructing the $g^{(2)}$ function for low time delays between two photons, which occur if two photons arrive close to each other and are detected as a single one [29]. Another aspect of the use of two arms is that it allows to increase the dynamical range of the detection system, since the detector area used for photon counting becomes twice bigger, and hence it can accept twice more photons.

Time reference. The acquisition rate of 45–85 Hz implies that the statistics should be accumulated for several hours. During this time, the locking between the streak-camera sweeping pulses and the laser pulses can fluctuate, which can lead to shift of the time axis of the streak-camera, and cause a significant reduction of the temporal resolution. To fix the time reference, a tiny fraction of the exciting laser pulse is sent on the streak-camera slit alongside with the microcavity emission. This laser pulse produces a bunch of counts, forming a spot on the streak-camera screen, as shown on the bottom of Figure 4.2a. For each frame, the center of this spot is computed, and the time axis is subsequently corrected. The calculated time shift is shown in Figure 4.3b, and it is clearly much larger than the time resolution of the streak-camera. This unambiguously justifies the necessity of the time axis correction. The image with corrected time axis can be seen in Figure 4.2b, where the Josephson oscillations in a photonic molecule are presented (see Chapter 5 for more details). Clear oscillations with a period of about 9 ps confirm high quality of the time axis correction.

Active sample stabilization. During the many-hour experiment, the microcavity sample can shift in respect to the exciting laser and the imaging optics. This happens mostly because of the gradual cooling of different parts of the cryostat, and subsequent change of their size. This shift is typically of order of several microns, which is indeed very critical for the experiments with polaritonic populations in small artificial traps. Hence, use of an extra tool that maintains the position of the sample is of high importance.

We use an active feedback system that is tracking position of the sample and moving it back if necessary. Namely, the system repeatedly acquires the images of the sample and compares them by using a LabVIEW image cross-correlation subroutine. If an image shift is detected, the cryostat position is adjusted by using piezo elements in the cryostat translation stages until the image shift becomes acceptable.

A simplistic imaging system is depicted in section 3 of Figure 4.1. For the experiments in transmission geometry, a CW laser with a wavelength of $\lambda = 695$ nm is used to excite the polaritons from the top of the sample (shown as green on the right side of the sample in Figure 4.1b), and the pattern of their emission is observed from the bottom of the microcavity (left side in Figure 4.1b). In reflection geometry, the sample is installed on the front site of the sample holder. The back surface of the holder is illuminated with a incandescent light source and imaged in a confocal geometry (Figure 4.1b). In Figure 4.3a, an example of the adjustment applied to the sample during a 19-hour experiment is shown. As it can be seen, the sample holder can move over few microns during a long experiments, which is critical if for instance the polaritons in small artificial traps are studied.

4.3 Data acquisition

As discussed in the previous Chapter, the acquisition speed of the system is limited by the frame rate of the CCD. Even though the maximal frame rate of the full CCD area is 16 Hz only, it can be noticeably increased by using the pixel binning, and reading the signal from only a part of the CCD area. One should note that reducing the vertical size of the CCD readout area will also reduce the accessible time range, so that evolution at the longer time will not be accessed. Thus, a compromise between the frame acquisition rate and the measured time range has to be found for every particular experiment. Practically, if nonresonant excitation is used (Chapter 5), the lifetime of the polariton BEC is given by the long-living excitonic reservoir, making it demanding to use the full CCD area. This gives the time range of 165 ps and the frame rate of 45 Hz. On the other hand, if the resonant excitation is used (Chapter 6), the polariton lifetime is much shorter since it is defined by the quality of the resonator. This allowed us to use 1/4 of the CCD lines with refresh rate up to 85 Hz and the time range of 40 ps.

At high frame rates of the CCD one should be sure that the glow time of the phosphorescent screen is short enough to prevent the fluorescence coming from the previous frames. In the C5680 streak-camera, a P-43 phosphorus is used, for which the luminescence decreases by

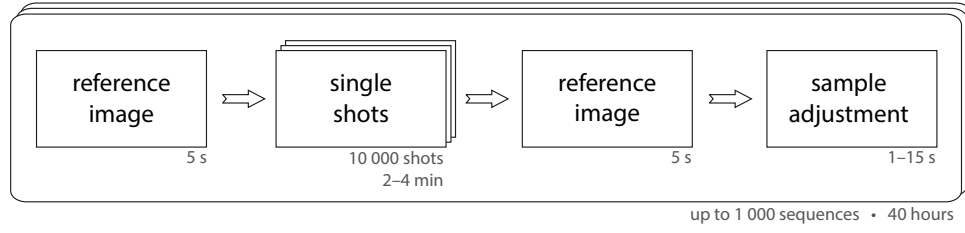


Figure 4.4: Timeline of the ultrafast second-order correlation measurement experiment.

10^3 in 5 ms. This is significantly lower than the fastest CCD frame rate, being about 12 ms, which means that the afterglow effects are negligible in our experiment. In practice, we set the CCD acquisition time to 1 ms since it is enough to acquire the most of the phosphorescent screen emission. Further increase of the acquisition time would only lead to the increase of the streak-camera dark noise, which is found to be the main obstacle for the correlation measurements of the low-intensity light. Indeed, at signal-to-noise ratio (SNR) lower than 20, the experimental error of $g^{(2)}$ measurement starts to be too large for confident claim about the light statistics [95]. In our experiment, the dark count rate is found to be $1.2 \cdot 10^{-6}$ photocounts per 1 binned CCD pixel. Practically this means that for the CCD area of 192x128 pixels we detect one dark count every 35 frames.

As mentioned above, the permanent active feedback on the sample position is essential for the long-term stability of the experiment. The single photon counting is being paused during the correction phase, since the sample imaging changes the excitation conditions of the sample. Another step during the pause in single photon counting, which was found to be useful, is observation of the sample emission dynamics. The main purpose of this is to check the way the sample is imaged, and to pinpoint possible issues, such as errors in the position stabilization, intolerable jitter of the streak-camera, or change of the exciting conditions. In this regime, the pulse picker passes bunches of 100 laser pulses at the repetition rate of 5 kHz, which provides sufficient power of the sample emission to be detected by the streak-camera, and saved as *reference images*.

Overall, we find it to be very practical to perform the data acquisition in sequences, each of them consists of 10000 single laser shots, two reference images before and after single shots, and the stabilization of the sample position at the end. The timeline of the experiment is shown in Figure 4.4. Practically, in every sequence the single-photon counting takes from 2 to 4 minutes, where reference image acquisition and the sample stabilization take not more than 25 seconds in total.

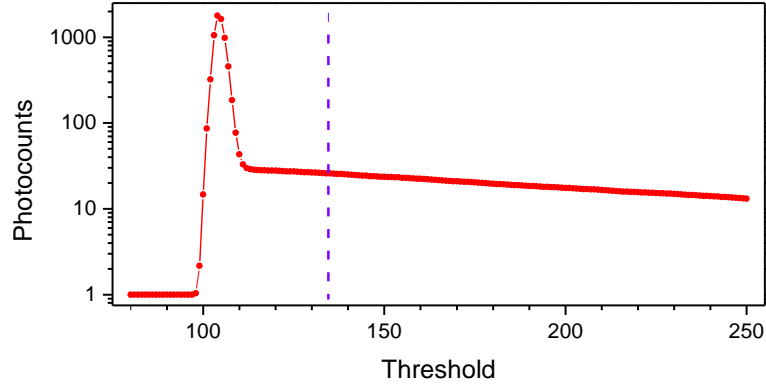


Figure 4.5: Threshold for the single photon counting. Dashed vertical line corresponds to the threshold of 135 used in the experiments.

4.4 Data processing

For every single photon counting sequence, the frames acquired by the CCD camera are saved in a single file with different frames stored one after another. Then, every frame is processed using a photon counting procedure that looks for spots with an intensity higher than a certain threshold, and then finds central positions of every spot. The single-photon counting threshold is found empirically to be not too high to miss the spots that are not bright enough, as well as not too low to detect a CCD noise as single photons. It is clear from Figure 4.5 that the latter results in increased number of counts at threshold below 110. Lower thresholds would get close to CCD background signal, and all the pixels form a single connected spot, that is recognized as a single photocount. In our experiment, the single photon counting threshold is set to 135, which is above the CCD noise, but still stays low enough to detect all the bright spots.

Next, for every frame, the position of the time reference laser is determined and used to correct the time position of the single-photon counts (on the left of Figure 4.2a). Since one acquired sequence can occupy up to 1 GB of a disk space, they are deleted after the single-photon counting and the reference time calculation are done. To optimize the disk space usage even more, the sequence processing is being performed while the next sequence of single photons is being acquired, and the processed sequences are being deleted during the experiment.

For the further processing, the reference images acquired before and after every single shot sequence are verified (Figure 4.6). If the reference image features significant distortion (like in Figure 4.6c), the corresponding sequence is disregarded from the following computation.

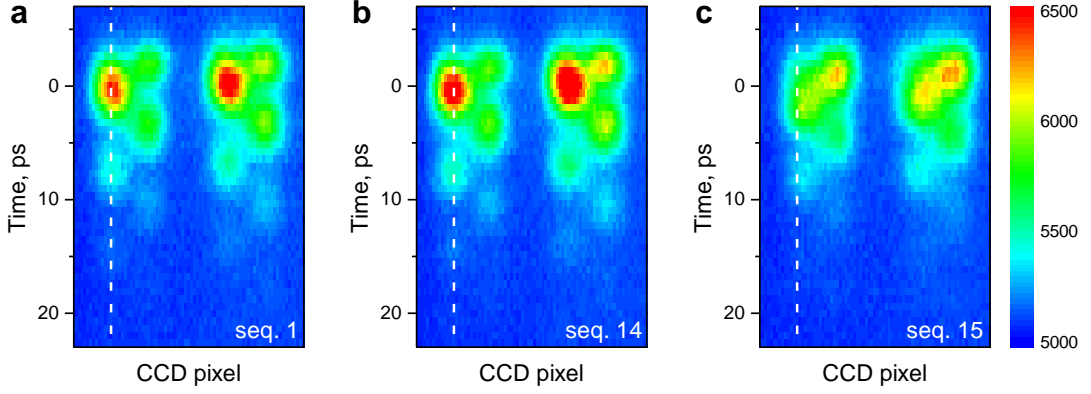


Figure 4.6: Reference images before the single shot sequences number (a) 1, (b) 14, (c) 15. Dashed line is a guide to the eye. During the sequence 15 the sample has shifted, and this sequence was excluded from the subsequent data processing.

Next, all the photon counts from valid sequences are divided into the time bins of given size in space and time, and then number of single photons in every time bin $n_j^s(t)$ is calculated. Here, all the variables are discrete: $s = 1, 2, \dots, N$ enumerates the sequences, whereas $j = 1, 2$ and $t = t_1, t_2, \dots, t_{\max}$ are the space and time numbers of the bin. After this, the time-dependent second-order correlation function between two moments of time t_1 and t_2 can be calculated as defined in Chapter 2.4:

$$g^{(2)}(t_1, t_2) = \frac{\langle n_1(t_1) \cdot n_2(t_2) \rangle}{\langle n_1(t_1) \rangle \cdot \langle n_2(t_2) \rangle} \quad (4.1)$$

with the averaging being performed over the sequence number s . The error of $g^{(2)}$ is calculated from the standard errors of $\langle n_1 \rangle$, $\langle n_2 \rangle$ and $\langle n_1 \cdot n_2 \rangle$.

Of particular interest for the measurements of the light statistics is the zero-delay second-order correlation function, also discussed in Chapter 2.4. It appears from equation (4.1) at $t_1 = t_2 = t$:

$$g^{(2)}(0)(t) = \frac{\langle n_1(t) \cdot n_2(t) \rangle}{\langle n_1(t) \rangle \cdot \langle n_2(t) \rangle} \quad (4.2)$$

It is worth mentioning that the total number of sequences can alter for different t because of the time reference that shifts the time axis. This can be seen from an example shown in Figure 4.7: for $t = t_1$, total number of sequences is 2, because the time axis of the sequences number 2 and 3 was shifted, and they were not involved in computation of $g^{(2)}(0)(t_1)$. At later moments of time, such as $t = t_3$, the number of sequences is 4, even if there were no photons detected in any of these sequences. In the data processing routine, for every moment of time

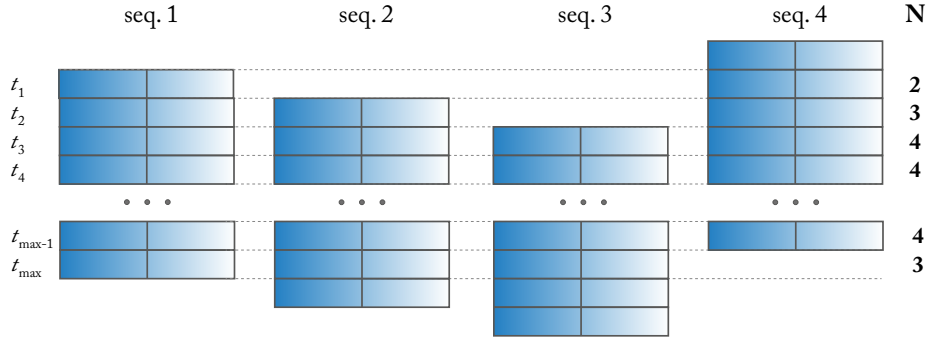


Figure 4.7: Shift of the time axis causes reducing number of sequences N , which is used to calculate $g^{(2)}$ at different moments of time.

first, the number of sequences is counted, and then the $g^{(2)}$ value is calculated.

4.5 Conclusion

The setup allows us to simultaneously measure the dynamics of the microcavity emission, and the time-resolved second-order correlation function. It features high temporal (up to 2.2 ps) and spatial (about 1 μm) resolution, and uses an active stabilization to fix the spatial position of the sample as well as the time axis during the experiment. Finally, use of the HBT scheme makes the setup well suited for study of spatially extended microcavity emission. In the next Chapters the application of this setup to study of various polaritonic systems will be presented.

5 Formation of a polariton BEC

Spontaneous Bose-Einstein condensation of polaritons is a bright manifestation of a quantum phase transition in the solid-state system. The presence of the *condensation threshold*, the minimal population of polaritons able to trigger the condensation process, makes the microcavity a very convenient system to accurately compare the behavior of non-condensed polaritons with the condensed ones by simply crossing the threshold. Such feature allowed for an exhaustive analysis of various characteristics like the long-range order, energy state occupancies, polarization [45], presence of topological defects [11, 12], and others on both sides of this quantum phase transition.

On the other hand, the spontaneous condensation occurs in time domain, with the large population of non-condensed polaritons relaxing down the dispersion curve by means of the stimulated scattering, and occupying the single energy state. Therefore, the same quantitative characteristics are expected to signify the phase transition during the process of BEC formation. One of important characteristics is the second-order coherence, which is expected to directly indicate the appearance of the polariton coherence at the BEC transition. In this Chapter, we take advantage of a streak-camera as an ultrafast single photon detector to study the statistics of the microcavity emission, and evaluate its second-order coherence all along the condensation process.

5.1 Overview

During the spontaneous BEC formation, the charge carriers undergo energy relaxation, reach the lower polariton dispersion branch at high momentum k , and finally, occupy its ground

state at $k \approx 0$ through stimulated scattering. The latter process is mediated by the parametric scattering of polaritons [97, 98] and hence occurs on a timescale of few picoseconds. To access such fast dynamics, one requires an ultrafast light detector like a streak-camera. Streak-cameras have been used widely by the polariton community, which made it possible to follow the condensation process dynamically, and to have access to such important characteristics as the long-range order and first-order spatial coherence [89, 99], phase profile, and appearance of topological defects [58, 100].

Another quantity expected to change during the condensation process is the second-order coherence of the microcavity emission. Specifically, when the polaritons do not yet occupy the ground energy state, they obey a Boltzmann energy distribution [45, 101], which is expected to lead to the thermal light statistics [59]. On the other hand, the polariton BEC is a single-mode state that can be described with a wavefunction possessing a well-defined phase, and hence it is expected to observe coherence of polariton population at first, second and even higher orders. Very conveniently, the polariton statistics can be accessed right from the photon statistics of the microcavity emission, since the emitted photons form part of the polaritonic wavefunction [39]. Therefore, the measurements of the polariton statistics were traditionally performed using the Hanbury Brown and Twiss detection scheme with avalanche photodiodes [59]. Unfortunately, this approach suffered from the low time resolution of APDs, and despite the second-order coherence below and above the condensation threshold was accessed and compared [91, 92], it was impossible to resolve the dynamical transition during the condensation. Also, the low time resolution prevented these measurements from seeing clear signatures of a thermal or coherent light statistics.

An alternative method to estimate the second-order coherence was suggested in [102]. It relies on the fact that the degree of linear polarization of the microcavity emission is known to increase for a condensed phase due to the polarization pinning to the crystallographic axes [103, 104]. The authors explain how the degree of linear polarization is linked to the second-order coherence, and therefore are able to access it by performing the time-resolved polarization measurements. While being clearly an interesting proposal, this technique still remained an indirect way of measuring the second-order coherence.

In our study, we take advantage of a streak-camera, which is also capable to detect single photons. This is achieved by applying the voltage to the microchannel plate (MCP) inside the streak tube, which essentially acts as an electron multiplier. While one photon hitting the photocathode of the streak tube produces one single electron, the MCP allows to turn

this electron into an avalanche that is much more easy to detect. Such approach makes it possible to measure photon statistics with a time resolution of few picoseconds, and therefore, to access the second-order coherence during the polariton relaxation down to the BEC. The experimental conditions and requirements that turned out to be necessary for this are mentioned below.

5.2 Spontaneous Bose-Einstein condensation of polaritons

The spontaneous formation of the polariton BEC was studied in the CdTe planar microcavity that was described in Chapter 3. From the previous research [45], it is known that this very microcavity possesses a noticeable photonic disorder, which manifests itself as a variation of the energy of the cavity mode on a micrometer scale. When crossing the BEC threshold at a certain excitation power P_{thr} , such a photonic disorder can lead to formation of multimode condensates [83, 90], where separated BECs formed in the minima of the photonic disorder co-exist with each other. This becomes particularly evident by applying the spectral tomography technique, described in Chapter 3.2.2, to a spatially extended region of the sample. Results of such measurements are presented in Figure 5.1. Below the condensation threshold (panels on the left), no long-range order is present in the system, as it can be evidenced from the absence of the interference fringes in Figure 5.1e. Crossing the condensation threshold is accompanied by an emergence of the long-range order (confirmed by the fringes in Figure 5.1f) and massive occupation of the bottom of the lower polariton branch (Figure 5.1b). From the latter, it can be noticed that although the photoluminescence comes from the bottom of the dispersion curve, the emission rather appears in different energy states. Practically, it was possible to distinguish seven of them, marked E1–E7 in Figure 5.1b. These energy levels corresponded to the emission from clearly distinct regions of the sample, as it was evidenced by the real-space spectral tomography data. The regions corresponding to the emission of different energy states are depicted in Figure 5.1d as colored semi-transparent regions, marked with labels from E1 to E7 and overlaid with a real-space image of the microcavity emission.

One can clearly see that the states at the energies E1–E6 are localized, either in one or in few spatially separated regions. In fact, most of them (E2–E6) demonstrate bright emission from several spatially separated spots. This implies that they should be considered not as condensates occupying a single potential minimum, but rather as spatially extended condensed phases, which demonstrate nonuniform emission intensity from the spatially large region [90]. The limiting case is the state E7, emission of which can be observed from a spatially elongated

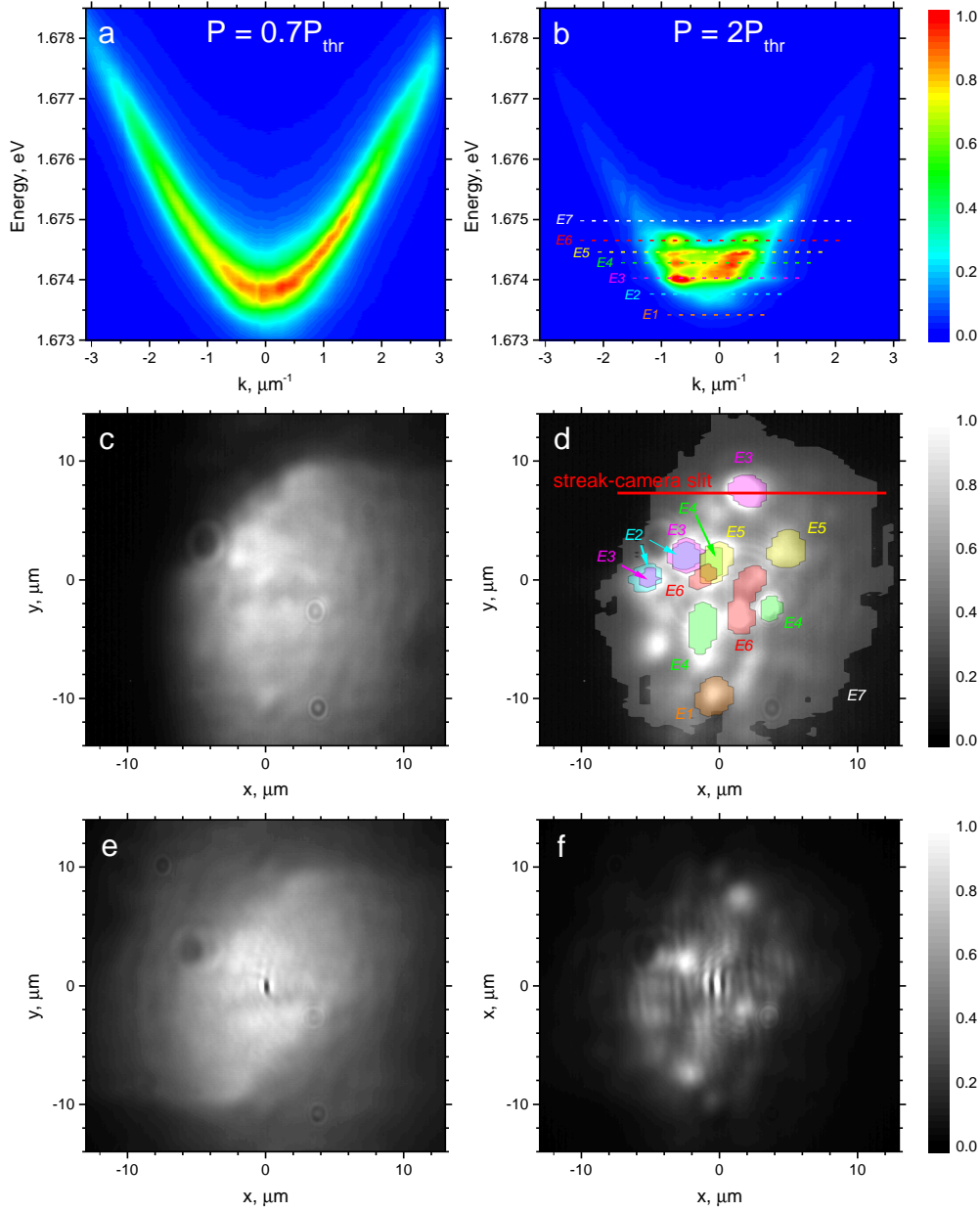


Figure 5.1: (a-b) Dispersion of the lower polariton branch of the CdTe microcavity under nonresonant pulsed excitation. (c-d) Real-space photoluminescence of the microcavity. (e-f) Photoluminescence signal after the Michelson interferometer in the mirror-retroreflector configuration. Laser excitation power is $0.7 P_{\text{thr}}$ for (a,c,e), and $2 P_{\text{thr}}$ for (b,d,f). Below the condensation threshold, no long-range order is present. Above the BEC threshold, polariton condensation in multiple spatial modes occurs. Modes with different energies $E1 - E7$ are shown with colored dashed lines in (b), and with colored semi-transparent regions in (d). Red line in (d) shows the position of the entrance slit of the streak-camera during the time-resolved measurements (sections 5.3–5.5).

5.2. Spontaneous Bose-Einstein condensation of polaritons

region more than $15\ \mu\text{m}$ in diameter that includes all the maxima of the states E1–E6. This is the reason of the emission being almost absent at the energy of E7 in Figure 5.1b: this state occurs at a wavevector $\mathbf{k} \neq 0$, whereas the dispersion plot is given for $k_y = 0$. Therefore, only a faint emission from the E7 state can be seen on the dispersion curve.

Another noticeable feature of the multimode condensation is that the emission of different BECs can arise from the same spatial region. This can be seen from the overlap of the states E2–E3, and E4–E6 in Figure 5.1d. Such behavior is consistent with the previous observations of coexisting condensates in the same CdTe microcavity [90].

To sum up, the microcavity luminescence is composed by the emission of several BEC. However, study of the emission statistics of multiple polariton condensates would be rather undesirable. One of the reasons is that the formation of different condensates is not expected to happen simultaneously, and this might significantly affect the emission statistics during the condensate formation. Another argument is that emission of several coherent sources from the same region of space could lead to quantum beats. With the energy separation between the different states of about 0.2–0.5 meV, this would lead to the beats with the period of order of 10–20 ps. This would not only be additional source of uncertainty in the experiment, but also would be difficult to distinguish from Josephson oscillations between weakly coupled condensates [55], or relaxation oscillations due to the presence of the excitonic reservoir [105]. Therefore, it is highly preferable that the second-order correlation measurements are performed on a single BEC.

Based on these reasons, the single bright spot in the E3 state on the top of Figure 5.1d was chosen for the correlation measurements. As seen from the plot, this spot was separated by at least $5\ \mu\text{m}$ from the other bright emission spots, and could be imaged on the input slit of the streak-camera (red line in Figure 5.1d) separately from the other localized BECs. Moreover, this particular spot demonstrated very strong emission, which was highly favorable for the single-photon counting. In fact, even strong emission required very long integration time to get clear measurements. To gather enough signal, the excitation power was boosted up to $10P_{\text{thr}}$. At such high power, the dynamical blueshift did not allow to see clearly the emission of different BECs, and therefore spectra in these excitation conditions are not presented here. Nevertheless, the state E3 still appeared to be separated in energy from the extended state E7, and they did not merge into a single condensate like in [83]. Therefore, the streak-camera was detecting the photons emitted from both states E3 and E7.

To separate the emission of these two BEC, a real-space filter (Figure 4.1b, part 4) was used. It was formed by the two $f = 200$ mm lenses with a pinhole of a variable size in between, thus passing the emission only from the region just around the bright E3 state onto the streak-camera slit. Because of high brightness and localization of the E3 state, the emission detected by the streak-camera in this case was dominated by the state E3, and the measured statistics could have been attributed to this single BEC solely. Without the real-space filter, we were in fact recording the emission from both condensates. The results of the time-resolved $g^{(2)}(0)$ measurements are discussed in the following section.

5.3 Zero-delay second-order correlation measurements

The measurements of the time-resolved second-order correlation function $g^{(2)}(0)$ were performed following the technique described in Chapter 4. The CdTe microcavity was excited with nonresonant laser pulses with duration of ≈ 300 fs and at a central wavelength $\lambda = 697$ nm. The emission from the lower polariton branch was collected in the reflection geometry, passed through a bandpass filter with $\lambda_{pass} = 740 \pm 5$ nm ($E_{pass} = 1.674 \pm 0.010$ eV) to cut off the scattered laser light, and focused on the streak-camera entrance slit. The photon correlations were calculated for the emission coming from the microcavity area of $6 \mu\text{m}$, centered onto the E3 BEC (Figure 5.1d). To start with, we study the statistics of polaritons during the formation of a single BEC in the state E3, selected by the real-space filtering.

The measured dynamics of the sample emission intensity is presented in Figure 5.2a, where the beginning of the time axis corresponds to the arrival of the exciting laser pulse. The lower polariton branch starts to be occupied ≈ 30 ps after the nonresonant laser pulse. Later on, at $t \approx 40$ ps, the polariton density at the ground state increases massively, manifesting the formation of the polariton condensate. The formed BEC has an out of equilibrium, driven-dissipative nature: on one hand, it is being permanently fed by the relaxation from the long-living excitonic reservoir; on the other hand, polaritons are leaking out of the cavity due to the short lifetime of their photonic component. As a result, the lifetime of the BEC is determined not by the quality factor of the microcavity, but rather by the lifetime of the excitonic reservoir, and amounts to about 50 ps, as can be observed in Figure 5.2a.

The corresponding values of the measured second-order correlation function are presented in Figure 5.2b. When the polaritons relax to the bottom of the polariton dispersion curve and eventually form the condensate, the $g^{(2)}(0)$ function changes its value from about 2 down

5.3. Zero-delay second-order correlation measurements

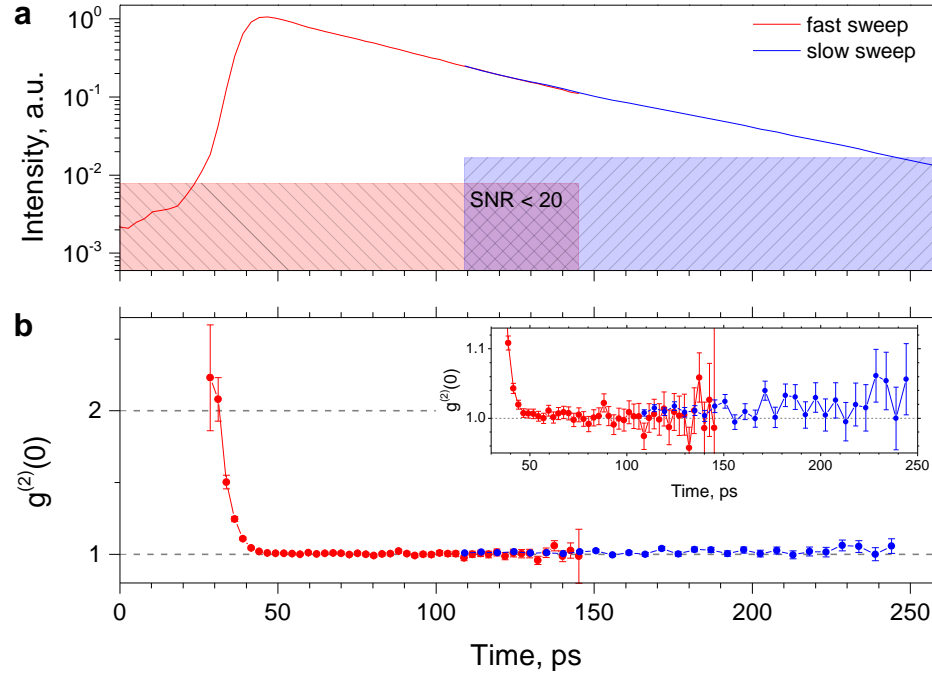


Figure 5.2: (a) Dynamics of the intensity of the microcavity emission after nonresonant pulsed excitation. Shaded areas mark the regions for which SNR is less than 20. (b) Measured $g^{(2)}(0)$ during the evolution of the polariton BEC. Inset: zoomed in version of the data in (b). Two data sets are acquired using different time ranges of the streak-camera and are shown in red and blue respectively. Measured $g^{(2)}(0)$ is shown only for SNR > 20.

to 1.005 ± 0.002 . This unambiguously indicates that the thermal statistics of the emission is replaced with a coherent one when the BEC is established, and clearly confirms the creation of a macroscopic coherent state. The further evolution of the BEC can be observed using a slower time range of the streak camera (this corresponds to the slower sweep voltage applied to the streak-camera deflection plates). These data are presented in Figure 5.2 with the blue points. As one can see, the condensate emission keeps a high degree of second-order coherence for at least 200 ps.

During the subsequent evolution of the BEC, the polariton density decreases, and finally one should expect the breakdown of the condensate [106]. This is expected to occur when the population of the exciton reservoir will be too low for an effective feeding of the BEC. After the condensed state vanishes, the emission should again be dominated by the thermal polaritons giving $g^{(2)}(0) = 2$. Practically, this transition remains unobservable in our experiment since it would occur significantly later than the longest time achievable by our detection system. At this time, the experimental SNR becomes too low for quantitative measurements. At the

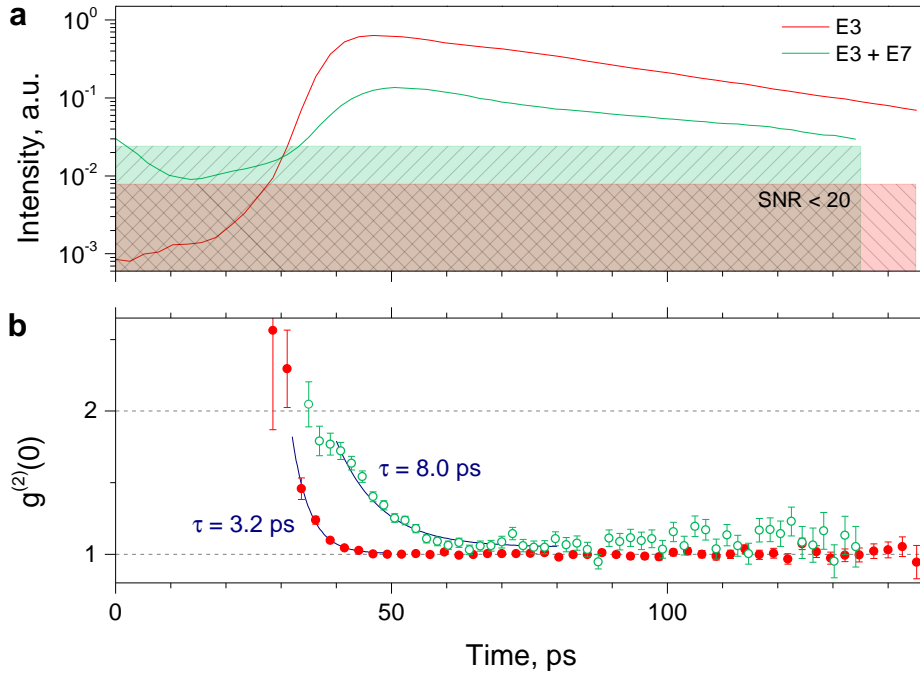


Figure 5.3: Comparison of the coherence of a single BEC in state E3 (red), and two BECs E3 and E7 (green). (a) Dynamics of the emission intensity. (b) Measured $g^{(2)}(0)$ during the formation of the polariton BEC. Dark blue lines are exponential fits to the decay of the $g^{(2)}(0)$ with the decay time given on the plot. Difference in the intensity of two curves is primarily due to the alignment of the bandpass filter.

same time, an increasing trend of $g^{(2)}(0)$ with time (inset in Figure 5.2b) can point out that the role of thermal polaritons in the overall emission increases while the polariton density drops down.

Next, we move to the study of the emission coming from two BECs in states E3 and E7. For this, no real-space filtering was applied during the imaging of the microcavity emission. The results of measurements with and without real-space filtering are compared in Figure 5.3. The most prominent difference between the two is that the $g^{(2)}(0)$ for the emission of both condensates shows a noticeable deviation from the value of 1. In fact, such behavior does not seem surprising: if no real-space filtering is performed, one also detects the emission of the noncondensed thermal polaritons far from the center of the laser excitation spot. Presence of the light with thermal statistics naturally lead to an increase of the measured $g^{(2)}(0)$ value.

More interestingly, the transition time from thermal to coherent state gets noticeably longer if emission from both condensates E3 and E7 is recorded. While for the BEC E3 alone the transition to the coherent state was occurring over about 3.2 ps, here, for both BECs, the

5.4. Comparison with the first-order spatial coherence

transition time increases to 8 ± 1 ps. (One should note that these values are the upper limits since they are close to the actual time resolution of the streak-camera being 2.2 ps.) This difference can be directly related to the difference in the size of two condensates, since a certain amount of time is required to expand the BEC over the large region. Therefore, the time of formation of a localized BEC E3 is defined by the relaxation. On the contrary, the transition time for the large BEC E7 also includes the time spent to expand the condensate over its whole area.

In fact, formation of a macroscopic coherent state not only requires that all the particles reach the ground energy state, but also that the quantum phase is synchronized across the condensate region. The timescale of the phase synchronization can be defined by both the speed of sound, and the driven-dissipative nature of the polariton BEC. The latter means that the condensed fraction of polaritons does not form a closed system, but is in constant interaction with the exciton reservoir. Therefore, the phase propagation velocity can exceed the speed of sound, as it has been shown in [89]. This makes it highly demanding to study how the second-order coherence is affected by the phase propagation velocity. The latter can be measured from the first-order spatial correlation function akin to what has been performed in [89]. Results of such measurements are discussed in the following section.

5.4 Comparison with the first-order spatial coherence

Following the definition (2.39), the time-dependent first-order spatial coherence of the spatially extended polariton BEC can be defined as $g^{(1)}(\mathbf{r}_1, \mathbf{r}_2, t) = \langle \Psi^*(\mathbf{r}_1, t) \Psi(\mathbf{r}_2, t) \rangle$, where $\Psi(\mathbf{r}, t)$ is the condensate wavefunction. Experimentally, it was accessed using the scanning Michelson interferometer in mirror-retroreflector configuration as described in Chapter 3.2.4, thus giving us the value of $g^{(1)}(\mathbf{r}, t) = g^{(1)}(\mathbf{r}, -\mathbf{r}, t)$. For this, the position of the sample was adjusted so that the images of the localized condensate in the state E3 in mirror and retroreflector arms were overlapping with each other when imaged onto a CCD or a streak-camera slit. In other words, the autocorrelation point of the interference image was at the position of the localized BEC E3. The sample was excited nonresonantly in the same way as in the experiment where $g^{(2)}(0)$ was measured. Particularly, it was important that the excitation spot is centered on the autocorrelation point to get the symmetry of the condensate propagation. The excitation power was set to $2P_{\text{thr}}$.

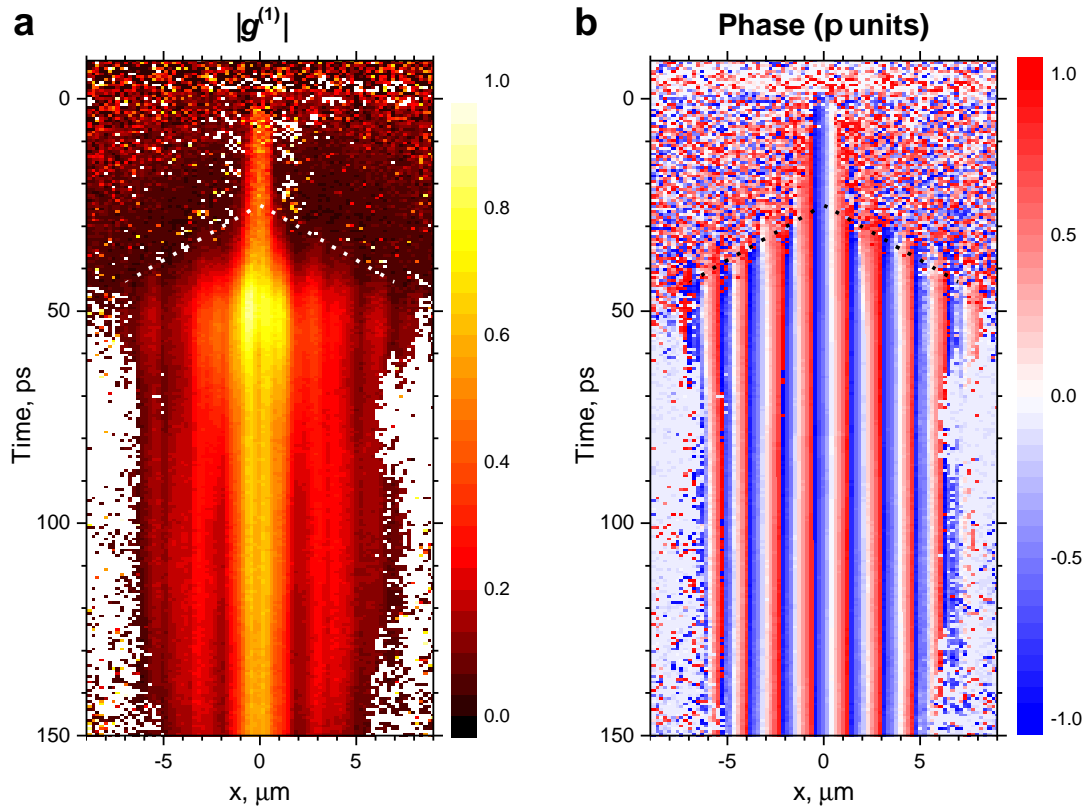


Figure 5.4: Dynamics of (a) the amplitude of the first-order spatial coherence function $g^{(1)}(\mathbf{r}, t)$, and (b) the phase of the interferogram. Data are acquired for the streak-camera slit position shown in Figure 5.1d. The autocorrelation point ($x = 0 \mu\text{m}$) is at the center of the BEC E3. Absence of the coherence data at $|x| > 8 \mu\text{m}$ is due to a dark non-luminescent defect in this area of the sample. Dashed lines schematically show the propagation of the coherence front and are at the same position on both plots.

The results of the measurements are presented in Figure 5.4. The left panel shows the amplitude of the first-order coherence, $|g^{(1)}(\mathbf{r}, t)|$ evolving in time and space, with the exciting laser pulse arriving at $t = 0$ ps, and $x = 0 \mu\text{m}$ being the autocorrelation point. One can clearly see that the coherence remains high on the autocorrelation point even at the time when no polariton emission is observed. This is due to the equal length of the interferometer arms: even for a thermal light, the coherence length would be larger than the imbalance between the interferometer arms. The size of the autocorrelation area of about $1 \mu\text{m}$ is defined by the resolution of the imaging system. Although hindering the real degree of coherence of the localized BEC in state E3, this does not affect the study of the long-range propagation of the condensate in the state E7.

5.4. Comparison with the first-order spatial coherence

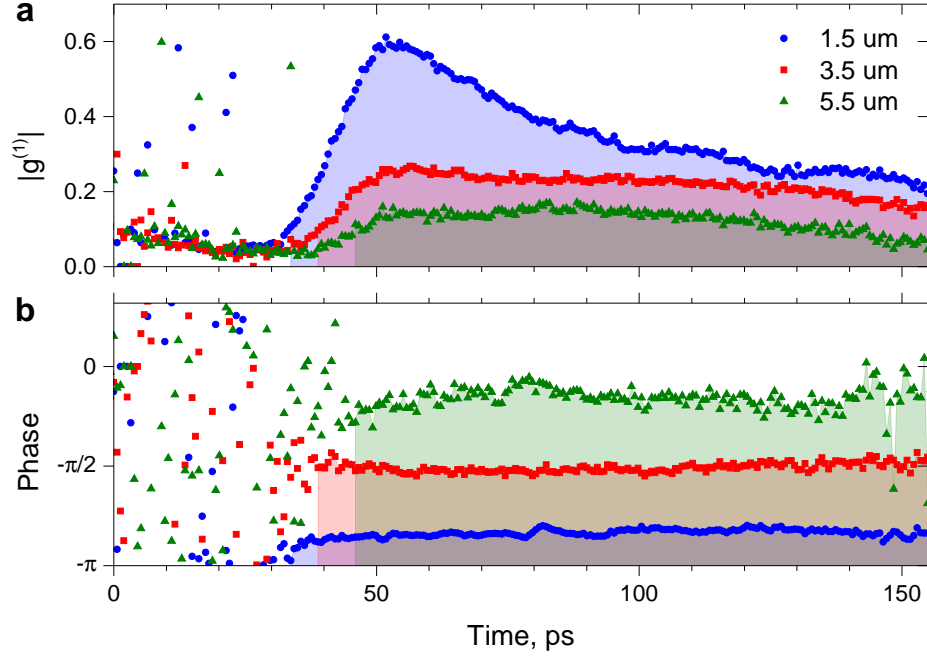


Figure 5.5: Dynamics of (a) the amplitude of the first-order spatial coherence function $g^{(1)}(\mathbf{r}, t)$, and (b) the phase of the interferogram at distances 1.5 (blue), 3.5 (red), and 5.5 (green) μm from the autocorrelation point. Shaded areas for every curve show the moment when the coherence emerges, as indicated by the dashed lines in Figure 5.4.

About 30 ps after the laser pulse, the polaritons start reaching the bottom of the dispersion curve. At the same point, degree of the first-order coherence $|g^{(1)}(\mathbf{r}, t)|$ around the autocorrelation point starts to increase (Figure 5.4a), manifesting the formation of the condensate in the state E7. Then, the coherence starts to emerge around the autocorrelation point with a constant speed: the further one goes from the autocorrelation point, the more time is required to get coherence. This is schematically shown in Figure 5.4a with white dashed lines. The moment when the coherence emerges can be seen even more clearly in Figure 5.4b, where we present the phase of the interferogram. Although this quantity is meaningless by itself for a single BEC, it is clear from the plot that on the onset of the coherence, the phase starts to have a well-defined value. Even more strikingly, the phase stays at a constant value up to the end of the experiment, for at least 150 ps. The black dashed line at the same position and with the same slope as in (a) indicates the propagation velocity of the coherence front.

The mentioned features can be seen even more clearly in Figure 5.5. Here, the dynamics of $|g^{(1)}(\mathbf{r}, t)|$ (a) and the phase of the interference pattern (b) are shown at the distances 1.5 (blue), 3.5 (red), and 5.5 (green) μm from the autocorrelation point. The stabilization of the phase is

especially evident from the part (b). At the onset of coherence, the phase suddenly stabilizes, after which it does not exhibit any noticeable change. It is also worth noticing that the phase stabilization occurs when $|g^{(1)}|$ reaches the value of 0.08–0.1, as it is seen from Figure 5.5. This presumably corresponds to the fact that at this value, the interference fringes start to be clearly visible on the background, and therefore the phase of the interference pattern could clearly be defined.

To sum up, such measurements allow to determine the propagation speed of the coherence front. One should remind that coherence at a certain distance r from the autocorrelation point means that the coherent area has size of $2r$, since the interferometer mixes a microcavity emission with its mirror image. This allows to find the coherence propagation speed to be $0.4 \mu\text{m/ps}$. Therefore, the formation of the coherent condensate with the size of $6 \mu\text{m}$ should take up to 7.5 ps. This value is consistent with the relaxation time of $g^{(2)}(0)$, which was measured to be 8 ± 1 ps (Figure 5.3). However, one should note that these two measurements were performed at different excitation power ($10P_{\text{thr}}$ for $g^{(2)}$, and $2P_{\text{thr}}$ for $g^{(1)}$). These values stay lower than the speed of sound estimated from the blueshift of the BEC energy and being about $0.8 \mu\text{m/ps}$, similar to the value reported in [89]. This indicates that the phase propagation at this particular position of the microcavity is defined not by the driven-dissipative nature of polaritons, but rather by the polariton-polariton interactions, similarly to what occurs in the atomic BECs.

5.5 Nonzero-delay second-order correlation measurements

A closer look on the polariton second-order coherence can be given by looking on the nonzero-delay correlation function $g^{(2)}(\tau) = \langle g^{(2)}(t_1, t_2 = t_1 + \tau) \rangle_{t_1}$. This function is widely used for traditional correlation measurements, since the contrast between the values of $g^{(2)}(\tau = 0)$ and $g^{(2)}(\tau \rightarrow \infty) = 1$ clearly reveals the statistics of photocounts, and the transition time between these values can be attributed to the coherence time of the system [59]. However, this quantity is only reliable if one deals with the source, properties of which do not change in time, for example, a CW laser or an LED. This is not the case of our study: after the pulsed excitation, the microcavity emission traverses both the regimes without and with the long-range order. Averaging over these two regions when calculating $g^{(2)}(\tau)$ will essentially wash out the statistical features of both of these states. Particularly, this could have been the primary reason of seeing no significant change in $g^{(2)}(0)$ when passing the polariton condensation threshold in the pioneering works [91, 92], where the avalanche photodiodes with the time

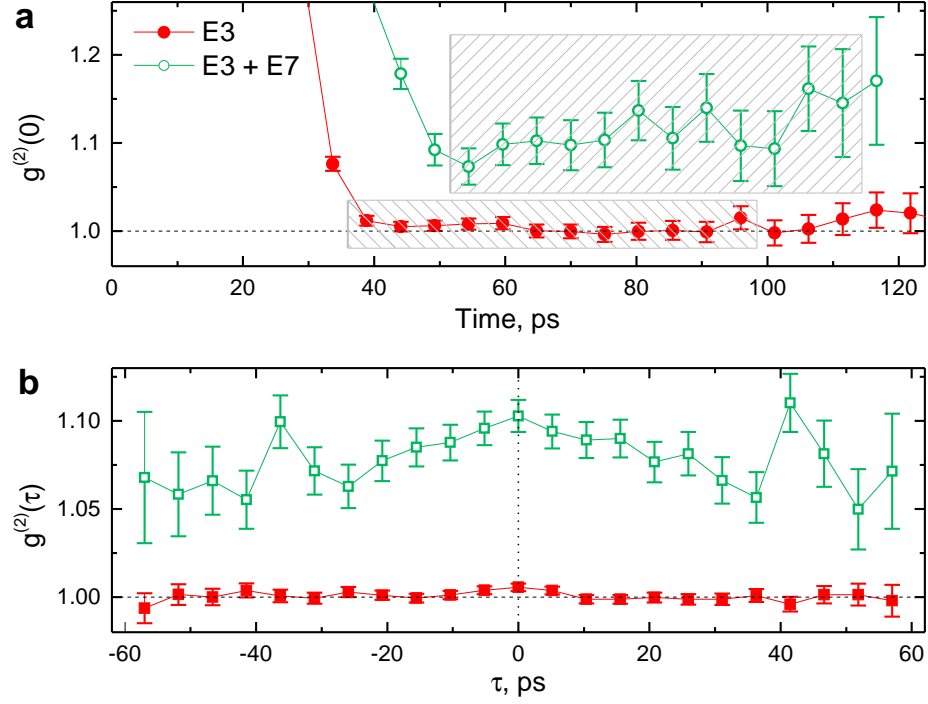


Figure 5.6: (a) Dynamics of $g^{(2)}(0)$ for a single BEC with (red filled points) and without (green open points) real-space filtering. (b) Results of $g^{(2)}(\tau)$ measurements for the data within hatched rectangles in (a).

resolution of about 50 ps have been used.

Fortunately, the use of our ultrafast correlation measurements makes it possible to separate the microcavity emission before and after the condensation, and to consider these two regimes independently. From the experimental point of view, the study of the emission of thermal polaritons before the condensation remains challenging since it lasts for a very short time (less than 10 ps), when the lower polariton branch starts being occupied, and the condensate is not yet formed. More important, low polariton density on the lower polariton branch makes the photoluminescence signal very hard to detect. These two factors make measurements of $g^{(2)}(\tau)$ of noncondensed polaritons barely possible. Therefore, the data below will be presented only for the emission of polaritons that have already formed a BEC.

The statistics of the condensed polaritons is shown in Figure 5.6. The $g^{(2)}(\tau)$ data were calculated from the weighted mean of $g^{(2)}(t_1, t_2)$ values during the time shown with dashed rectangles in Figure 5.6a. The measured $g^{(2)}(\tau)$ values are presented in Figure 5.6b.

As it was mentioned above, the $g^{(2)}(\tau)$ graphs are expected to reach the value of 1 for large time delays τ between different photons. However, this transition cannot be seen for the emission of the BEC in the state E3, since $g^{(2)}(\tau = 0)$ is already too close to 1 (red data points in Figure 5.6b). On the contrary, for the emission of both BECs E3 and E7, $g^{(2)}(\tau = 0)$ is noticeably higher than 1, but the values of τ giving $g^{(2)}(\tau) = 1$ stay beyond the time limits of the experiment (green data points). Nevertheless, the descending trend of $g^{(2)}(\tau)$ when increasing τ is clearly seen. This allows us to estimate the lower bound of the BEC coherence time to be 60 ps, i.e. the maximal time range given on the graph. This result shows once again that the coherence of the non-equilibrium polariton BEC is not defined by the lifetime of polaritons in the microcavity, but by the lifetime of the whole condensate, which is given by the long-living excitonic reservoir.

5.6 Conclusion

In this Chapter, ultrafast second-order photon correlation measurements were used to directly observe the statistics of polaritons during their relaxation to the ground state and spontaneous formation of Bose-Einstein condensate. After being established, the condensate keeps its coherence thanks to the long-living excitonic reservoir, which feeds the BEC for at least 200 ps. These results are in good agreement with the measurements of the first-order spatial coherence.

The major experimental difficulty during this experiment was low luminescence intensity of the microcavity during the time region of interest. Particularly, unambiguous observations of the transition from thermal to coherent statistics became possible only at an excitation power one order of magnitude higher than the condensation threshold. Another challenging goal, the measurements of the dynamics of the light statistics that remains thermal all the time below the condensation threshold, turned out to be barely achievable because of the weak intensity of the emission. To the best of our knowledge, the only measurement of this kind so far was reported in [30], shortly after our first report [107], and the thermal statistics with $g^{(2)}(0) = 2$ was still not observed.

The measurements of spontaneous condensation processes suffer from the fact that a significant amount of excitation power goes to the exciton reservoir, which increases the lifetime of the system, but drastically reduces the peak luminescence intensity. One can realize an opposite kind of behavior by preparing a coherent state through a resonant laser excitation of

the lower polariton branch. In this case, it is the quality factor of the microcavity that sets the polariton lifetime to be of order of 1–10 ps. In the next Chapter, we will discuss the statistics of resonantly excited polaritons localized in artificially created mesa potentials.

6 Periodic squeezing in a polariton Josephson junction

Various bosonic systems possess an intrinsic nonlinearity that arises from the repulsive particle-particle interactions. For the condensed phases it leads to the emergence of the nonlinear term in the Gross-Pitaevskii equation (1.17). Nonlinear behavior of microcavity polaritons originates from their excitonic predecessor and leads to variety of the quantum phenomena like, for instance, bistability [108, 109] or specific features in the dynamics of vortices [110, 111] and solitons [13].

As it was mentioned in Chapter 2.5, the nonlinear effects in photonic systems are one of the prime mechanisms of generating the nonclassical and squeezed states of light fields. Concerning the polaritonic system, the concept of the photon blockade in the semiconductor microcavity has already been proposed in 1997 [69]. However, the polariton nonlinearity turned out to be insufficient to realize any nonclassical effects even for decent positive detunings and the polariton traps with the size down to $1\ \mu\text{m}$. At the same time, the quadrature squeezing close to the turning point of the polariton bistability curve has been successfully accessed both in a planar microcavity [25] and a micropillar [26].

In this Chapter, we investigate the second-order coherence of polaritons in a more sophisticated system, a polariton Josephson junction consisting of two potential traps with tunnel coupling between them. This geometry is of high interest since the Josephson physics can also be enriched when the nonlinearity is introduced into the system. Our measurements supported with the simulations of the system at a quantum level indicate the emergence of the quadrature squeezing arising from the interplay between the tunneling and the polariton nonlinearity. The origin of this phenomenon and its possible future extensions are discussed in detail.

6.1 Overview

It has been predicted in the seminal work of B. D. Josephson that a potential difference between two weakly coupled superconductors can give rise to a non-classical oscillating current between them [112]. One year later, the *Josephson effect* was demonstrated experimentally [113]. This discovery quickly found numerous practical applications, including magnetic sensors, voltage standards, and qubits [114].

Since the key ingredient of the Josephson junction (JJ) is the tunnel coupling of two quantum states, similar phenomenology was predicted in other macroscopic quantum systems. The term *bosonic Josephson junction* is used to specify such systems where the (quasi)particles involved in the dynamics have bosonic statistics [115]. The first observations of the Josephson effect in bosonic systems were performed in the junction made of two baths of superfluid ^3He [116] and ^4He [117] connected via small apertures. Later on, successful demonstration of Bose-Einstein condensation of alkali gases [43] and its macroscopic coherence even after splitting into smaller parts [118] provided atomic BECs as a new very convenient experimental system for the experiments on Josephson physics. Subsequent studies, first on multiple [119] and next on single junctions [120, 121] demonstrated the rich phenomenology of bosonic Josephson junctions, as predicted by the mean-field models. Last but not least, bosonic Josephson junctions realized with microcavity polaritons were reported both in BEC regime [55] and for resonant excitation [19].

Interestingly, even if the phase coherence between two macroscopic quantum populations is kept, the quantum dynamics of the system can provoke nonclassical effects. Particularly, interactions can suppress the fluctuations of the particle number or relative phase below the standard quantum limit [122]. This phenomenon can also be treated as a *pseudospin squeezing*, where the pseudospin is a thought degree of freedom of a particle showing on which side of the Josephson junction it is [123, 124]. Similar effects caused by the nonlinearities in photonic systems are expected to affect the light statistics. One bright example is the unconventional photon blockade discussed in Chapter 2.5. A more general effect, squeezing of Gaussian states [81], allows controlling the light statistics by tuning the parameters of the system.

This Chapter is devoted to the measurements of the light statistics emitted by a polariton Josephson junction. The latter is formed by two mesas set close enough to each other to realize weak tunnel coupling between them. By exciting resonantly the coupled polariton modes,

the Josephson oscillations in the system can be triggered, and the features of the polariton statistics can be revealed using the setup for ultrafast correlation measurements.

6.2 Bosonic Josephson junction in a nutshell

In this section, a brief theoretical description of the bosonic Josephson junction will be provided. Generally speaking, the behavior of a coherent system in a double-well potential is a many-particle problem described by the many-body Schrödinger equation. However, if one is interested in description of the weakly coupled ground state between two wells, then the problem can be studied in a two-mode approximation. The two-mode model provides a full quantum description of the system, and allows obtaining the dynamical solution through numerical evolution of the master equation.

On the other hand, it is much more illustrative to take a primal look on the Josephson dynamics from the mean-field description of the system. Although its area of validity is restricted only to large occupancies of the system, the mean-field model can be reduced to a simple set of differential equations with solutions giving a flavor of the different possible regimes of Josephson dynamics. In this section, we take a brief look on both quantum two-mode approximation and semiclassical mean-field description of the system.

6.2.1 Two-mode approximation

We start with considering the particles in a deep potential well. This leads to quantization of the energy states, and if the lateral size of the well is small enough, the separation between the quantized levels will be sufficient to consider them separately from each other. If two potential wells are brought close enough to each other to allow for a weak tunneling, then the coupling renormalizes the eigenvalues of the Hamiltonian and lifts the degeneracy of two ground states. Important conditions for validity of such consideration is that neither the coupling nor the particle-particle interactions should be strong enough to significantly shift the ground energy levels. In this case, one can introduce the creation and annihilation operators for the particles in both left and right potential wells $\hat{a}_{L,R}^\dagger$ and $\hat{a}_{L,R}$ [125]. The resulting Hamiltonian reads

$$\hat{\mathcal{H}} = \sum_{k=L,R} \left[E_k \hat{a}_k^\dagger \hat{a}_k + U \hat{a}_k^\dagger \hat{a}_k^\dagger \hat{a}_k \hat{a}_k \right] - J \left(\hat{a}_L^\dagger \hat{a}_R + \hat{a}_R^\dagger \hat{a}_L \right), \quad (6.1)$$

where E_k is the ground state energy, U is the strength of particle-particle interaction, and J is

the coupling between two modes.

6.2.2 Mean-field model

The mean-field model of the bosonic Josephson junction was in great details discussed in [126, 127, 128], where the system dynamics was classified. Later on, study of the dynamics accounting for dissipation [126] and damping [129] was carried out. In this section, the description of [127] will be followed, and few remarkable solutions of the Josephson dynamics will be discussed.

The dynamics of a degenerate Bose-gas with weak interaction can be described by the Gross-Pitaevskii equation:

$$i\hbar \frac{\partial}{\partial t} \Psi(r, t) = \left[-\frac{\hbar^2}{2m} \nabla^2 + V(r) + g |\Psi(r, t)|^2 \right] \Psi(r, t), \quad (6.2)$$

where $\Psi(r, t)$ is the wavefunction of the whole system, $V(r)$ is the double-well potential, and g describes the particle-particle interactions. Practically, one can usually access the quantum phases independently in the two potential traps. For example, in case of experiments with polaritons, one can study the intensity and the phase of the emission of both traps. Therefore, we will describe the whole system with a superposition of two wavefunctions Ψ_L and Ψ_R for the left and right potential traps respectively. This is possible because, for a weak link, the wavefunctions of two sides do not overlap:

$$\int \Psi_L(r, t) \Psi_R(r, t) dr = 0, \quad (6.3)$$

and the cross-interactions terms $\Psi_L \cdot \Psi_R$ arising from the quadratic term $|\Psi(r, t)|^2$ will be strictly zero. Moreover, the wavefunctions can be further factorized onto the spatially and temporally dependent terms:

$$\Psi(r, t) = \Phi_L(r) \psi_L(t) + \Phi_R(r) \psi_R(t). \quad (6.4)$$

Substituting this ansatz into the GPE (6.2), we obtain two equations for two traps:

$$\begin{aligned} i\hbar \frac{\partial}{\partial t} \psi_L(t) &= \left[E_L^0 + U_L |\psi_L(t)|^2 \right] \psi_L(t) - J \psi_R(t) \\ i\hbar \frac{\partial}{\partial t} \psi_R(t) &= \left[E_R^0 + U_R |\psi_R(t)|^2 \right] \psi_R(t) - J \psi_L(t), \end{aligned} \quad (6.5)$$

with the constants being defined by the corresponding overlap integrals [127]. The physical meanings of the variables $E_{L,R}^0$, $U_{L,R}$, and J is analogous to ones defined in equation (6.1). From now on, we will simplify the further consideration by assuming the interparticle interaction equal in both modes: $U_L = U_R = U$.

Equation (6.5) does not depend on the spatial degree of freedom, which makes it possible to consider the two modes as coherent states, each with well defined phase $\psi_k(t) = \sqrt{N_k(t)} e^{i\varphi_k(t)}$. Here N_k are the occupation numbers of the two states, and φ_k are the phases. When the phases are defined to the certain constant and their absolute values are of no meaning (except the fact that they evolve linearly with time), the *relative phase* $\phi(t) = \varphi_L(t) - \varphi_R(t)$ reveals the dynamics going on in the system and also serves as a signature of coherence. Another meaningful value is the *population imbalance* $z(t)$ between the two traps:

$$z(t) = \frac{N_L(t) - N_R(t)}{N_L(t) + N_R(t)}, \quad (6.6)$$

which takes values from -1 to 1 and shows how the total system occupancy is distributed between two traps. Particularly, $z(t)$ is positive if most of the particles occupy the left trap, negative in the opposite case, and zero for equal populations. By substituting expressions for $z(t)$ and $\phi(t)$ into equations (6.5), we can get the dynamical solutions

$$\frac{d}{dt} z(t) = -\sqrt{1 - z^2(t)} \sin[\phi(t)] \quad (6.7)$$

$$\frac{d}{dt} \phi(t) = \frac{\Delta E}{2J} + \frac{UN(t)}{2J} + \frac{z(t)}{\sqrt{1 - z^2(t)}} \cos[\phi(t)]. \quad (6.8)$$

where $\Delta E = E_L^0 - E_R^0$, and $N(t) = N_L(t) + N_R(t)$ is the total system occupancy.

For a symmetric Josephson junction with $\Delta E = 0$ one can classify the solutions depending on the nonlinear term U , i.e. on the strength of the particle-particle interactions.

Weak interactions. If only weak or even no particle-particle interactions are present in the system, then $UN \ll 2J$ and the only nontrivial solution of equations (6.7–6.8) are weak sinusoidal oscillations between two traps. This regime is usually referred to as *Rabi oscillations* or *plasma oscillations*. In this mode, both the population and the relative phase oscillate around the equilibrium point.

Medium interactions. If $UN \sim 2J$, the energy shift due to the particle interaction becomes significant to dynamically renormalize the energy states during the oscillations. The main consequence is that the oscillation period is changed compared to the case of Rabi oscillations. For the polariton system, which is dissipative by nature, the interaction term decreases with time due to decrease of $N(t)$. Therefore, one can observe the anharmonic oscillations with the period changing in time as the nonlinearity drops down. This regime has been observed in [19].

Strong interactions. The most spectacular Josephson physics occurs when $UN \gg 2J$. Given that population imbalance is large, the interactions drastically raise up the energy of the corresponding state. As a consequence, large energy difference prevents intensive tunneling so that the particles remain trapped on one side of the junction. This regime is called *macroscopic quantum self-trapping* (MQST), and it was experimentally realized with cold atoms [120] and polaritons [19].

One should note that equations (6.7–6.8) also have a trivial stationary solution $z(t) = 0$ and $\phi(t) = 0$. This means that the two mesas are equally populated, have equal phases, and therefore do not exhibit any oscillations. Such solution can be observed when the mesas are simultaneously excited with equal number of particles, i.e. the initial population imbalance $z(0)$ is zero. Therefore, to start the oscillations, one should prepare the JJ with a non-zero initial population imbalance. Large initial imbalance is especially important for realization of the self-trapping regime, where one should overcome a certain threshold to significantly split the renormalized energy levels.

Lastly, we consider the case of an asymmetric Josephson junction with $\Delta E \neq 0$.

AC Josephson effect. In this case, a non-zero constant term $\Delta E/2J$ is present on the right side of equation (6.8), giving rise to a solution with a running phase. In other words, the relative phase in this regime does not oscillate around the equilibrium value, but has a constant trend, either increasing or decreasing. The name *AC Josephson effect* arises from a similarity to the analogous effect in the superconducting Josephson junction, where the potential difference applied to the junction triggers the running phase solution and induces the oscillating current. One should note that given the strong interactions in the system, one can also obtain a running phase solution with a self-trapping of particles on one side.

6.3 Polariton Josephson junction

The polariton Josephson junctions were manufactured following the recipe described in Chapter 3.1.3, and consisted of two mesas with a small separation between them. The use of mesas has a significant advantage in comparison to the pillars [130]: the coupling strength between the mesas can be quite large for practical applications even if they are separated by $\approx 1 \mu\text{m}$. It is not the case for the pillars etched for the full depth of the microcavity, where the coupling requires the overlap of the pillars [19], since otherwise neither excitonic nor photonic components of the wavefunction can propagate outside the microcavity.

The Josephson junctions were created by fabricating two circular mesas with $2 \mu\text{m}$ diameter close to each other. This size was small enough to have large splitting between the quantized energy levels, and at the same time large enough to be reproducibly fabricated using the photolithography process. For the characterization of different junctions, their real- and reciprocal-space spectra, as well as real-space dynamics was recorded. These data for three JJ with different mesa separation are summarized in Figure 6.1.

For all Josephson junctions, one can observe the polariton emission from the 2D microcavity region surrounding the mesas with an exciton-photon detuning $\delta = +5 \text{ meV}$. (Figure 6.1 a–c). At such strong positive detuning, the upper polariton has a clear parabolic dispersion, resembling the one of the cavity mode. The lower polariton emission occurs close to the position of the exciton at $E_X = 1.464 \text{ eV}$ with almost flat dispersion.

On the contrary, mesas provide a 9 meV deep quantum well for the photonic mode (dashed line in Figure 6.1 d–f), leading to its quantization. Strong coupling of these quantized states to the exciton leads to formation of distinct polariton emission levels. Particularly, coupling of the lowest energy photonic mode to the exciton leads to formation of the lower polariton at $E = 1.461 \text{ eV}$ with a strong luminescence (Figure 6.1 d). Other photonic states in $2 \mu\text{m}$ mesas are located above the energy of the exciton, and the resulting emission of the lower polariton will be close to the exciton energy at $E = 1.464 \text{ eV}$. The upper polariton emission for all quantized states in the mesas is located above the exciton energy and has low emission intensity.

The data in the left column of Figure 6.1 are presented for a separation of $1 \mu\text{m}$ between the mesas. At this distance, the overlap of the polariton wavefunctions in two mesas is too weak for any significant coupling, so they behave as independent ones. This means, the ground states in both mesas remain unperturbed (Figure 6.1 a, d), and the dynamics of polaritons just

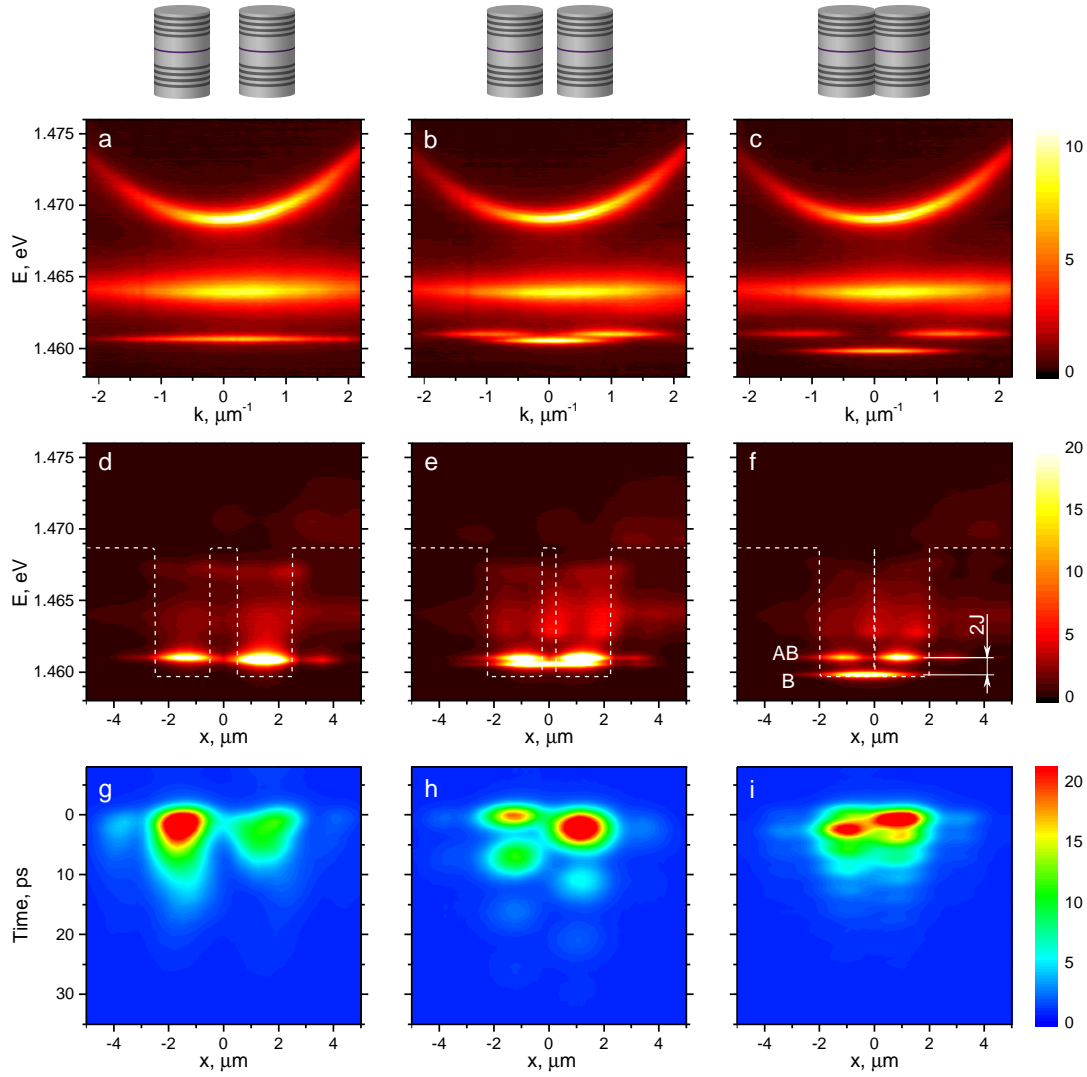


Figure 6.1: Josephson junctions with different mesa separations. (a-c) k -space and (d-f) real-space spectra of the microcavity under nonresonant CW excitation, (g-i) real-space dynamics under resonant pulsed excitation. Left column: for large mesa separation, no coupling is present, and the lowest energy state in both mesas at $E = 1.461$ eV is seen. Center column: coupling between two mesas leads to splitting of the ground energy level into bonding (B) and antibonding (AB) ones, and to subsequent Josephson oscillations of polaritons between two mesas (h). Right column: even stronger coupling leads to further splitting of B and AB states, and to an increase of the frequency of Josephson oscillations. Dashed line in (d)–(f) represents the energy of the cavity mode. Diameter of all mesas is $2 \mu\text{m}$.

features an exponential decay after a fast resonant pulse (Figure 6.1 g).

For a smaller gap between the mesas, namely $0.5 \mu\text{m}$ (central column in Figure 6.1), the overlap of the polariton wavefunctions leads to their tunnel coupling. This gives rise to the

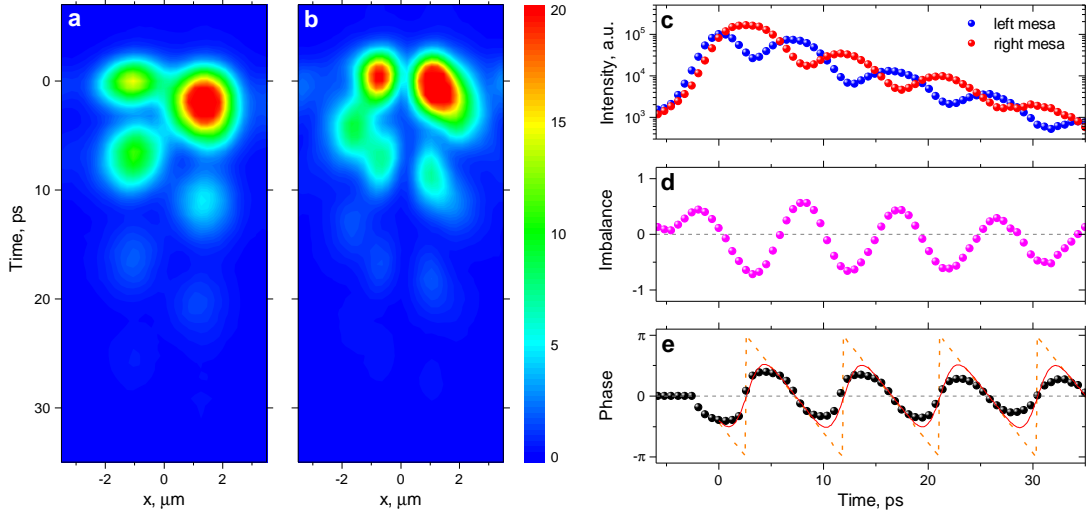


Figure 6.2: Josephson oscillations in a JJ with a $0.5 \mu\text{m}$ gap between the two mesas. (a) Real-space dynamics. (b) Real-space dynamics after the Michelson interferometer in the mirror-retroreflector configuration, giving the phase evolution. (c) Polariton population in left and right mesa. (d) Population imbalance between two mesas. (e) Measured phase of Josephson oscillations.

renormalization of the energy levels and splitting of the ground state into two: bonding (B) and antibonding (AB) ones with the energy separation $2J = 0.43 \text{ meV}$. Evolution of these two states gives rise to the Josephson oscillations: the polariton population oscillates between the left and the right mesa with a period defined by the energy splitting, $T = h/2J = 9.2 \text{ ps}$.

If the mesas are brought even closer, up to their direct contact (right column in Figure 6.1), the splitting between the B and AB states increases further, up to 1.2 meV . Correspondingly, the period of Josephson oscillations decreases down to 3.3 ps .

For practical applications, we used a JJ with a gap of $0.5 \mu\text{m}$. The main reason for this was that the period of Josephson oscillations in this case (9.2 ps) was significantly longer than the time resolution of the streak-camera (3.4 ps). The time-dependent intensity of the left $I_L(t)$ and right $I_R(t)$ mesa was extracted from the Josephson dynamics (Figure 6.2 a) and is presented in Figure 6.2 c. Figure 6.2d depicts the corresponding population imbalance $z(t)$.

According to equation (6.7), the dynamics of the bosonic JJ is driven by the relative phase difference between two sides of the junction. In case of the polariton JJ, this phase can be measured by superimposing the emission of the left and the right mesas and observing the resulting interference pattern. In our experiment, this was done using the Michelson interferometer in mirror-retroreflector configuration, as described in Chapter 3.2. The measured

phase difference is presented with black points in Figure 6.2e.

Although one would expect the phase to linearly increase with time as $\phi(t) = \omega \cdot t$ for the Josephson regime, this is not what is observed in the experiment. The reason is the finite temporal resolution of the streak-camera, which turns the phase “jumps” from $-\pi$ to π (since the phase is defined by modulo 2π) to smooth transitions. This is seen from the asymmetry of the measured phase oscillations: their raising edges are always steeper than the falling ones. This means that the falling edges correspond to the linear phase evolution, whereas the raising ones – to the phase jumps from $-\pi$ to π . Furthermore, the whole phase evolution can be represented by convolving the linearly increasing phase (dashed orange line in Figure 6.2 e) with the Gaussian representing the streak-camera resolution (2.2 ps). The discrepancy between the experimental data and the simulations (red line) can be explained by an extra jitter of the streak-camera, which was not compensated during this experiment.

The intensity oscillations together with the running phase unambiguously confirm that we indeed observe the Josephson oscillations of polaritons. At higher excitation densities, the regime with $UN \sim 2J$ and anharmonic oscillations can be achieved. This is confirmed by slight aperiodicity of the Josephson oscillations in Figure 6.3b given in the next Chapter. Nevertheless, even at the strongest excitation power we were not able to observe the MQST in this junction.

6.4 Second-order correlation measurements

The second-order correlation measurements were performed following the technique described in Chapter 4. The polaritonic Josephson junction was excited in resonance with the bonding and antibonding states. To prevent excitation of higher energy states, the laser pulses were spectrally filtered using a home-built pulse shaper (part 2 of Figure 4.1a). This reduced the spectral width of the laser to 0.7 meV, simultaneously increasing its duration to 1 ps. The system was excited with circularly polarized laser light. The laser was focused onto a 3 μm spot, mostly on one of the mesas in order to create high initial population imbalance and obtain high contrast of oscillations. The emission of the Josephson junction was collected in transmission geometry, and its real-space was imaged onto the entrance slit of the streak-camera. The data set presented here was obtained from 3.9 million pulses, acquisition of which took 34 hours.

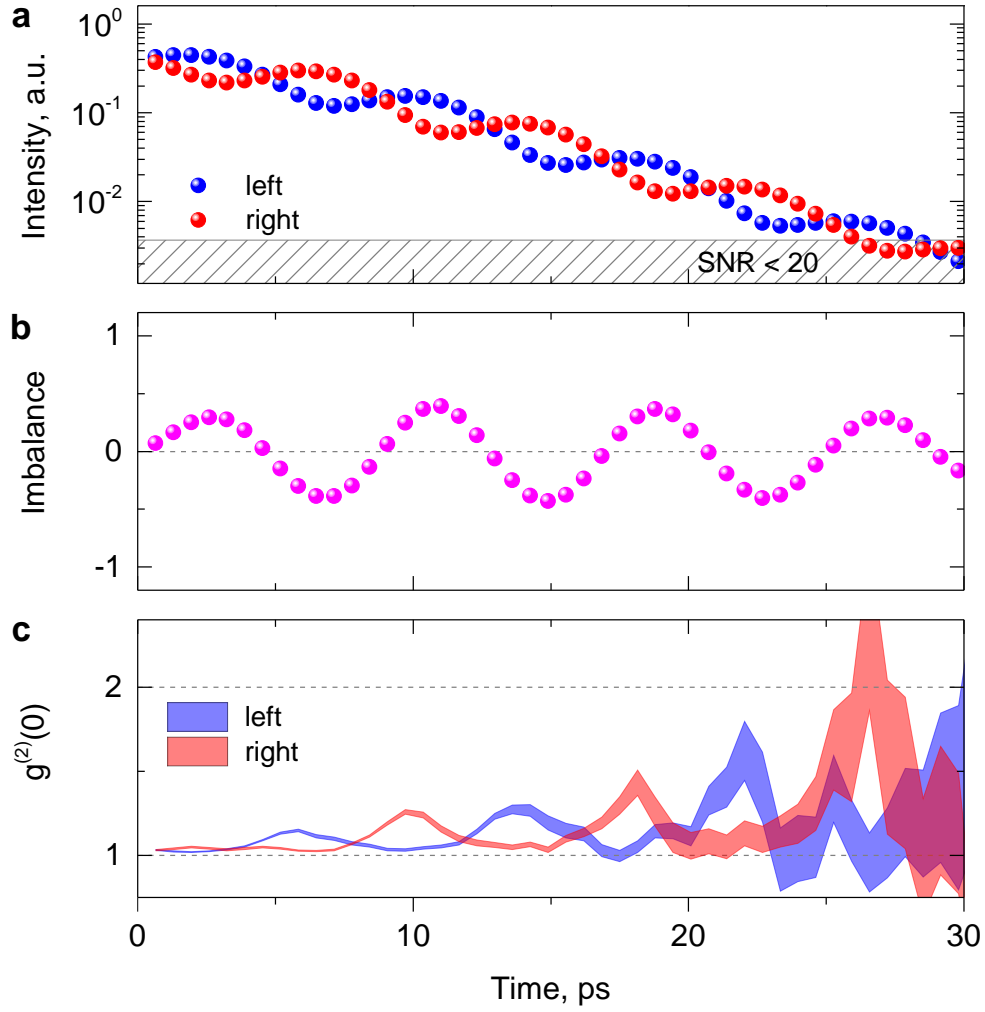


Figure 6.3: Dynamics of (a) emission intensity, (b) population imbalance, and (c) zero-delay second-order correlation function on a polariton Josephson junction. Shaded areas show the experimental errors. Emission statistics oscillates between Poissonian and bunched in phase with Josephson oscillations.

In Figure 6.3 a–b, the intensity of the emission from two sides of the junction and the population imbalance during the Josephson oscillations respectively are presented. The corresponding second-order correlation function $g^{(2)}(0)$ is shown with shaded areas in Figure 6.3 c. Despite the fact that the phase relation between the mesas' emission stays well-defined, which means that it should keep its first-order coherence, the emission does not show coherent statistics. The observed features can be summarized as follows:

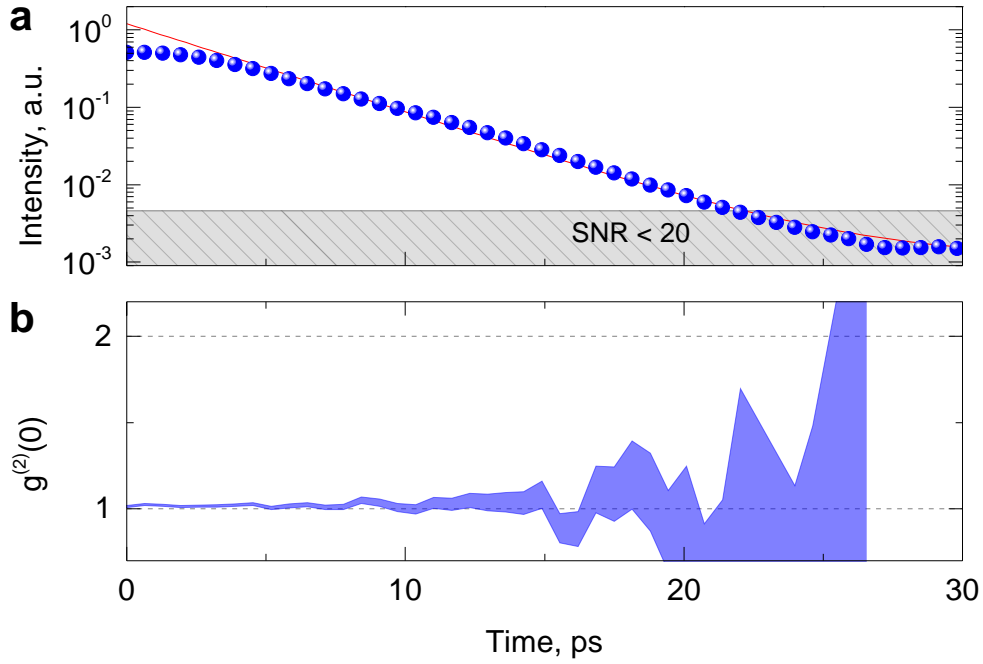


Figure 6.4: Dynamics of (a) emission intensity and (b) second-order correlation function of a single $2\ \mu\text{m}$ mesa. Emission statistics stays Poissonian all along the system evolution. Red line in (a) is an exponential fit showing that during first 3 ps saturation of the detector has occurred.

- the emission statistics in both mesas oscillates between the Poissonian and super-Poissonian one;
- this change occurs precisely in phase with the Josephson oscillations, and in opposite phases between two mesas;
- the magnitude of maximal bunching increases with time.

To start with, we should address the very first point, the fact that the light statistics does not stay Poissonian during the evolution of the system. It is well known that one of the main mechanisms of changing the light statistics are optical nonlinearities. The polaritonic system features some nonlinearity due to the excitonic component of the polariton wavefunction. Nevertheless, as it was emphasized before, we work at quite negative detuning (Figure 6.1), and it is highly improbable that the nonlinearity is the only reason for changing the light statistics. To prove this, we repeat the correlation measurements in the same conditions, but on a single $2\ \mu\text{m}$ mesa. The results are shown in Figure 6.4, where it is clearly seen that the emission stays coherent all along the system evolution.

Next, the polariton decoherence during the system evolution might be responsible for bunching with time. However, in no way it could explain the reversed process, a decrease of $g^{(2)}(0)$ value.

Finally, one cannot simply link the oscillations of $g^{(2)}(0)$ to the oscillations of the mesa occupancies, since as one can see from Figure 6.3, different $g^{(2)}(0)$ values can be observed for the same occupancies. Therefore, our observations bring us to the conclusion that the nontrivial behavior of the second-order coherence is some mutual effect of the coupling and nonlinearity, which also depend on the phase of Josephson oscillations. Indeed, it will be shown below that these features arise from the squeezing of the light field in the two-mode system, which induces deviations to the statistics of the coherent state. In the next section we introduce the theoretical model describing the system behavior at the quantum level.

6.5 Theoretical description

The theoretical simulations of the polariton statistics in the system were performed with a model developed by Dr. Hugo Flayac and discussed in details in [131]. The Hamiltonian of the system is essentially the one introduced in the two-mode approximation (6.1) only adding of the external driving coherent field that represents the laser excitation:

$$\hat{\mathcal{H}} = \sum_{k=L,R} \left[\hbar\omega_c \hat{a}_k^\dagger \hat{a}_k + U \hat{a}_k^\dagger \hat{a}_k^\dagger \hat{a}_k \hat{a}_k + P_k(t) \hat{a}_k^\dagger + P_k^*(t) \hat{a}_k \right] - J \left(\hat{a}_L^\dagger \hat{a}_R + \hat{a}_R^\dagger \hat{a}_L \right), \quad (6.9)$$

where ω_c is the resonance frequency of each of the modes. To mimic the experimental conditions, the system is driven by Gaussian laser pulses defined as

$$P_{L,R}(t) = p_{L,R} \exp \left[\frac{-(t-t_0)^2}{\sigma_t^2} \right]. \quad (6.10)$$

The relative intensity between p_L and p_R allows to mimic the initial population imbalance in the system.

The quantum dynamics of the system is conventionally studied by means of the master equation. However, in the case of the large populations, direct solution of the master equation would require enormous computational power. A convenient solution is to present the polariton operator as a sum of a large mean-field coherent component $\alpha_k = \langle \hat{a}_k \rangle$, and a quantum

fluctuation $\delta \hat{a}_k$:

$$\hat{a}_k = \alpha_k + \delta \hat{a}_k, \quad (6.11)$$

and to study the evolution of the two components independently. Namely, the mean-field dynamics can be evaluated through c-number equations:

$$\begin{aligned} i\hbar \dot{\alpha}_L &= [\Delta_L - i\kappa/2 + U|\alpha_L|^2]\alpha_L - J\alpha_R + P_L(t) \\ i\hbar \dot{\alpha}_R &= [\Delta_R - i\kappa/2 + U|\alpha_R|^2]\alpha_R - J\alpha_L + P_R(t), \end{aligned} \quad (6.12)$$

under the rotating wave approximation with the laser frequency ω_L , $\Delta_{L,R} = \omega_c - \omega_L$ being the detuning, and $\kappa = \hbar/\tau$ is the dissipation.

The fluctuation fields $\delta \hat{a}_k$ are governed by the master equation:

$$i\hbar \frac{\partial \hat{\rho}_f}{\partial t} = [\hat{\mathcal{H}}_f, \hat{\rho}_f] - i\frac{\kappa}{2} \sum_{k=L,R} \hat{\mathcal{D}}[\delta \hat{a}_k] \hat{\rho}_f. \quad (6.13)$$

where $\hat{\mathcal{D}}[\hat{o}] \hat{\rho} = \{\hat{o}^\dagger \hat{o}, \hat{\rho}\} - 2\hat{o} \hat{\rho} \hat{o}^\dagger$ are Lindblad dissipators accounting for the losses to the environment, and the Hamiltonian $\hat{\mathcal{H}}_f$ reads

$$\begin{aligned} \hat{\mathcal{H}}_f &= \sum_{k=L,R} \left[\Delta_k \hat{a}_k^\dagger \hat{a}_k + U \left(\alpha_k^{2*} \hat{a}_k^2 + \alpha_k^2 \hat{a}_k^{\dagger 2} \right. \right. \\ &\quad \left. \left. + \hat{a}_k^\dagger \hat{a}_k^\dagger \hat{a}_k \hat{a}_k + 2\alpha_k^* \hat{a}_k^\dagger \hat{a}_k \hat{a}_k + 2\alpha_k \hat{a}_k^\dagger \hat{a}_k^\dagger \hat{a}_k \right) \right] - J \left(\hat{a}_L^\dagger \hat{a}_R + \hat{a}_R^\dagger \hat{a}_L \right). \end{aligned} \quad (6.14)$$

where δ notation is omitted for compactness. Equations (6.12) and (6.13) are solved numerically in a Hilbert space truncated to a sufficient number of quanta to properly describe the weak fluctuation field. The expectation values are computed as $\langle \delta \hat{o} + \langle \hat{o} \rangle \hat{\mathbb{I}} \rangle = \text{Tr}[(\delta \hat{o} + \langle \hat{o} \rangle \hat{\mathbb{I}}) \hat{\rho}_f]$.

The second-order correlation function is calculated using a standard definition

$$g^{(2)}(t_1, t_2) = \frac{\langle \hat{a}^\dagger(t_1) \hat{a}^\dagger(t_2) \hat{a}(t_2) \hat{a}(t_1) \rangle}{\langle \hat{a}^\dagger(t_1) \hat{a}(t_1) \rangle \langle \hat{a}^\dagger(t_2) \hat{a}(t_2) \rangle}.$$

The Kerr nonlinearity present in the system is known to induce the squeezing of the light field due to presence of the quadratic terms $\alpha_k^{2*} \hat{a}_k^2 + \alpha_k^2 \hat{a}_k^{\dagger 2}$ in the Hamiltonian (6.14). Such terms lead to formation of the squeezing operator as defined in equation (2.28). Therefore, it is illustrative to calculate the value of the squeezing parameter $\xi_k = r_k \exp(i\theta_k)$ in the system.

Its magnitude and phase can be extracted from

$$\begin{aligned} r_k(t) &= \frac{1}{2} \left[|\langle \Delta \hat{a}_k \rangle| + |\langle \hat{a}_k \rangle|^2 - \langle \hat{a}_k^\dagger \hat{a}_k \rangle \right] \\ \theta_k(t) &= \arg \langle \Delta \hat{a}_k \rangle, \end{aligned} \quad (6.15)$$

where $\Delta \hat{a}_k = \langle \hat{a}_k^2 \rangle - \langle \hat{a}_k \rangle^2$. Concerning the coherent state $\alpha = |\alpha|e^{i\varphi}$ created by the displacement operator $D(\alpha)$, it is by definition equal to the mean value of the field $\langle \hat{a}_k \rangle$.

The calculated populations of both modes are mostly defined by the mean-field dynamics, and so does the population imbalance. The latter is shown with an orange line in Figure 6.5 a. Its noticeable deviation from the measured values is due to the temporal resolution of the streak-camera, which, in this case, amounted to 3.4 ps and therefore smoothed the dynamics of the oscillations. Nevertheless, when the simulated curve is convolved with the Gaussian representing the streak-camera resolution, it approximates the observed population imbalance quite well, as shown with a black dashed line. At the same time, the numerical solutions for the $g^{(2)}(0)$ function are superimposed on the experimental data in Figure 6.5 b and clearly show a remarkable agreement. The calculated values of the phase relation between the mean-field and squeezing operators $\cos(\theta - 2\varphi)$, and the squeezing magnitude r are presented in Figure 6.5 c and d, respectively. They not only show the periodic variation of the phase relation, but also the presence of a significant amount of quadrature squeezing, which also demonstrates oscillations in time.

Surprisingly, the maximal degree of bunching increases with time, whereas the magnitude of the squeezing magnitude is rather decreasing. Furthermore, the local maxima of squeezing magnitude do not correspond to the strongest bunching. This indicates that the bunching observed is defined not only by the amount of the squeezing, but rather by the phase term $\cos(\theta - 2\varphi)$. This behavior will be further discussed in the following section.

6.6 Discussion

6.6.1 Origin of the polariton squeezing

A coherent ensemble of non-interacting bosons in a single mode is expected to maintain its coherence until the interactions with the environment will disturb it. In the polariton Josephson junction we consider here, the evolution is affected by two more entities: single mode nonlinearity, and coupling between the two modes. In order to clarify the role of both of

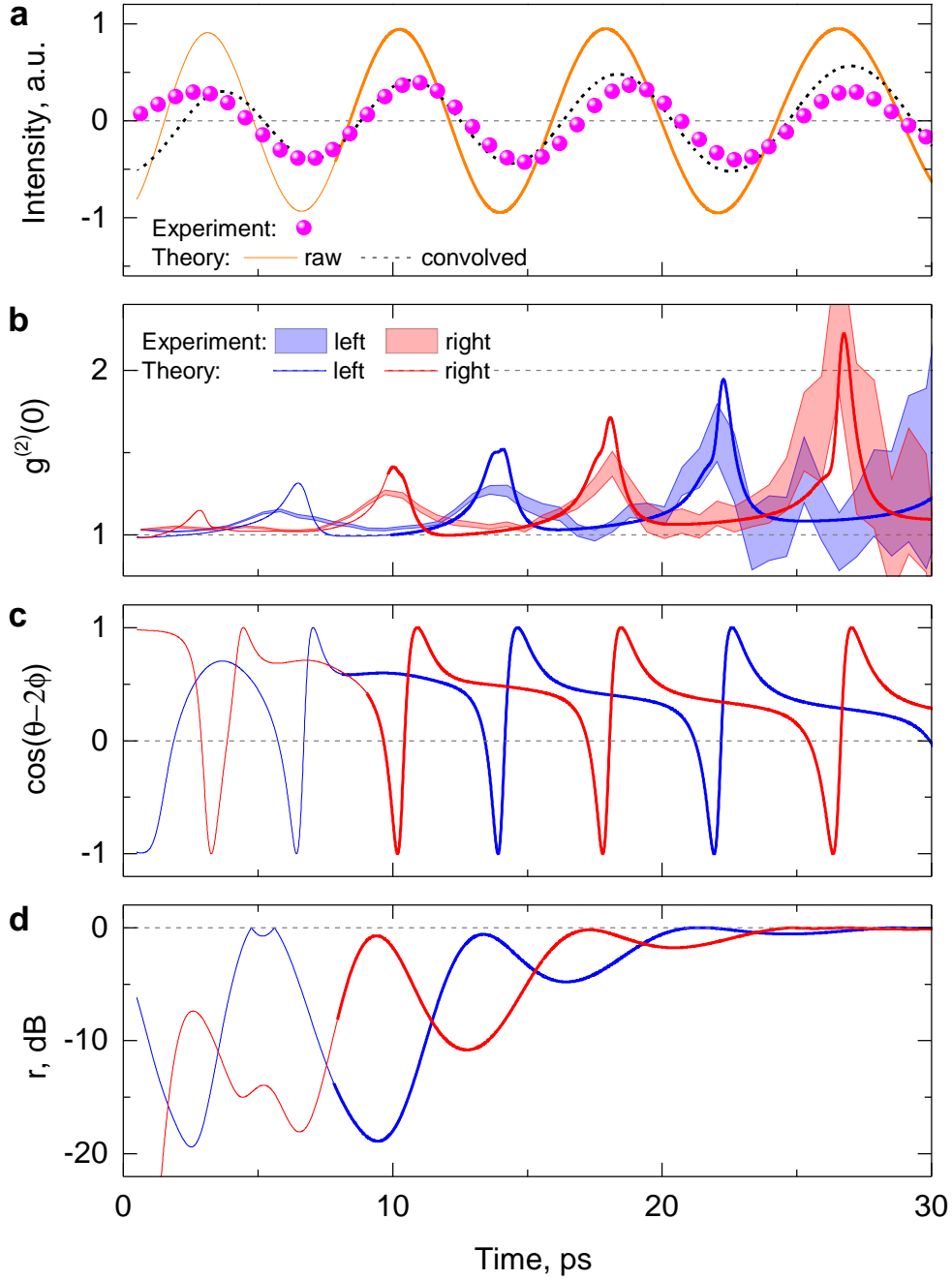


Figure 6.5: Simulations of the emission statistics coming from the Josephson junction. (a) Population imbalance measured in the experiment (magenta points), and simulated without (orange solid) and with (black dashed) convolution with the streak-camera resolution (3.4 ps FWHM). (b) $g^{(2)}(0)$ measured in the experiment (shaded) and simulated (lines). Shaded areas represent the errorbars. (c) Simulated phase relation. (d) Simulated squeezing magnitude. Blue and red lines correspond to the emission from the left and right mesa, respectively.

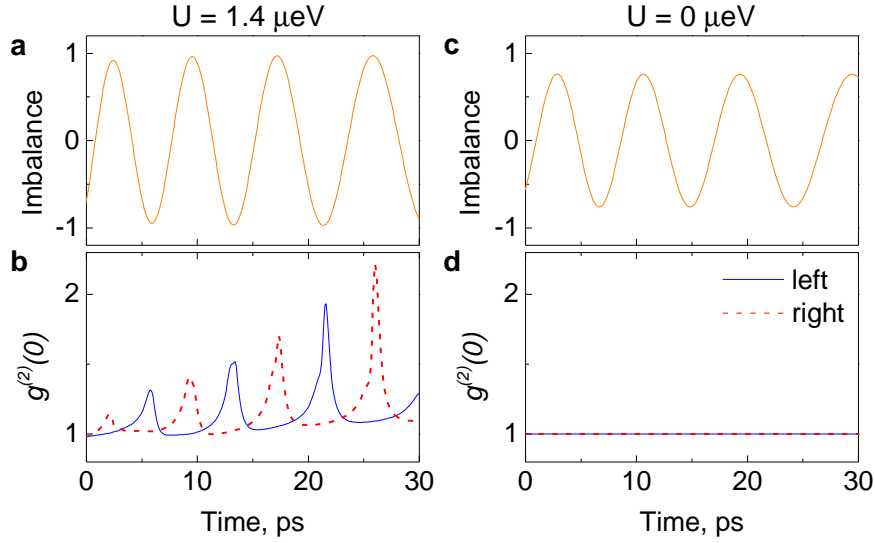


Figure 6.6: Role of the nonlinearity. (a) Population imbalance and (b) second-order correlation function for interparticle interactions $U = 1.4 \mu\text{eV}$. (c-d) Same, but for $U = 0$.

these entities, we consider each of the two independently.

To start with, if no nonlinearity U is present in the system, the Hamiltonian (6.9) loses all the higher-order terms. In this case, the Josephson oscillations can still be observed, however, the variety of solutions will be less rich than in nonlinear systems [127, 129]. The simulations with U set explicitly to 0 show that the dynamics of Josephson oscillations can still be reproduced, however, the light statistics shows absolutely no deviation from the coherent one giving $g^{(2)}(0) = 1$, as shown in Figure 6.6. This clearly shows that the coupling only cannot be responsible for the periodic changes in the observed light statistics.

Next, we consider the role of the coupling J in the system. In fact, even a single-mode polariton system possesses a Kerr-type nonlinearity U due to the excitonic component of the polariton wavefunction. At the single particle level, this nonlinearity is known to be very weak, which means that U remains much less than the polariton linewidth. Therefore, its behavior can be qualified in a linearized picture, where the higher-order terms in the Hamiltonian (6.14) are omitted. The remaining nonlinear terms $\alpha_k^{2*} \hat{a}_k^2 + \alpha_k^2 \hat{a}_k^{\dagger 2}$ allow us to transform the equations for the fluctuation fields to those of degenerate parametric oscillators. In this case, the parametric interaction amplitude seen by e.g. the left mesa equals to

$$\lambda_L^{\text{eff}} = U \left[\alpha_L^2 - \frac{J^2}{U^2 |\alpha_R|^4 - |\Delta_R - i\kappa/2|^2} \alpha_R^2 \right] \quad (6.16)$$

and can be linked to a squeezing parameter ξ_L as

$$\begin{aligned} r_L &= \frac{1}{2} \operatorname{arctanh} \left(\frac{2|\lambda_L^{\text{eff}}|}{\kappa} \right), \\ \theta_L &= \arg(\lambda_L^{\text{eff}}). \end{aligned} \quad (6.17)$$

Now, if there is no coupling between two modes, then $J = 0$ and the parametric interaction amplitude is linked only to the population of the same mode. Therefore, the squeezing parameter is bound to the population and cannot be adjusted. Essentially, we are left with a weak nonlinearity in a single mode, which cannot lead to any significant changes of the light statistics. This is also confirmed by our measurements in a single mesa shown in Figure 6.4.

As a result, we can doubtlessly claim that the change of the light statistics is coming from the mutual interplay between the weak nonlinearity and coupling of two modes. Equation (6.16) gives a clue to the physics of this action: it provides an additional degree of freedom for the control of the orientation of the squeezing ellipse, therefore allowing to change the squeezing direction by simply changing the populations between two mesas.

6.6.2 Effect of the system occupancy on the polariton statistics

The second-order correlation function shows a drastic dependence not only on the phase relation between the squeezing and the displacement operators, but also on the total occupancy of the system. To demonstrate the qualitative difference, we present in Figure 6.7 the dependence of $g^{(2)}(0)$ on both the phase relation and the total number of particles in the system n_{tot} obtained from equation (2.57). In this figure different subplots correspond to the different squeezing magnitudes involved in the study. Below, we address in more details the limiting cases of low occupancies $n_{\text{tot}} \approx 1$ and large occupancies $n_{\text{tot}} \gg 1$.

Large occupancies.

We start with considering the system with large number of particles $n_{\text{tot}} \gg 1$. In this case, the second-order correlation function is strictly limited to $1 - 1/|\alpha|^2 \leq g^{(2)}(0) \leq 3$ [81]. The strongest bunching, $g^{(2)}(0) \rightarrow 3$, is realized for the large squeezing magnitudes when $r \rightarrow +\infty$. Such values have previously been accessed in the experiment with continuous variable squeezing generated by the means of an optical parametric amplifier [132]. On the contrary, the minimal value of $g^{(2)}(0) = 1 - 1/|\alpha|^2$ is obtained when the squeezing magnitude meets

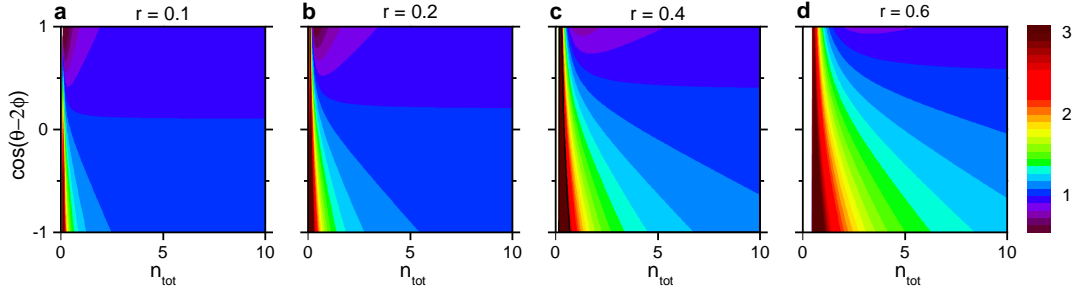


Figure 6.7: Map of the $g^{(2)}(0)$ function versus total population n_{tot} and $\cos(\theta - 2\varphi)$ for different amplitudes of the squeezing parameter: (a) $r = 0.1$, (b) $r = 0.2$, (c) $r = 0.4$, (d) $r = 0.6$. Antibunching can be observed in violet regions in the top-left corner of (a)–(c). The data were calculated from equation (2.58).

so-called *optimal squeezing condition*. Regardless on the squeezing amplitude, in the case of large occupancies $|\alpha| \gg 1$, this value will always be close to 1.

This leads to the main restriction for the study: if the system occupation is large, no non-classical statistics can be achieved. Nevertheless, the squeezing can manifest itself in super-Poissonian light statistics: $g^{(2)}(0)$ increases when $\cos(\theta - 2\varphi)$ is decreased (Figure 6.7). In our experiment, both phase angles θ and φ oscillate in phase with the Josephson oscillations, and so does the term $\cos(\theta - 2\varphi)$. Together with the fact that the regime of large occupancies is exactly what is explored in our experiment, this explains why the oscillations of $g^{(2)}(0)$ are observed in phase with the Josephson oscillations. It is important to emphasize once again that this very mechanism of generation of the super-Poissonian statistics is significantly different from all the other observations of bunching in polaritonic systems: it is the coupling of two nonlinear modes, and not a single-mode Kerr-nonlinearity, dephasing, thermalization, or any other mechanism.

Low occupancies.

The system behavior drastically changes for the total system occupancy of an order of unity. Decrease of $n_{\text{tot}} \rightarrow 0$ discards the strict upper and lower bounds for the value of $g^{(2)}(0)$, and opens the way towards the observation of the nonclassical light statistics. In this regime, sizable antibunching can be observed if the other necessary conditions are fulfilled, namely, the phase interrelation is such that $\cos(\theta - 2\varphi) \approx 1$, and the squeezing magnitude is relatively low. The regions of noticeable antibunching ($g^{(2)}(0) < 0.8$) are shown with violet regions in Figure 6.7. At the same time, the opposite phase relation $\cos(\theta - 2\varphi) \approx -1$ can lead to

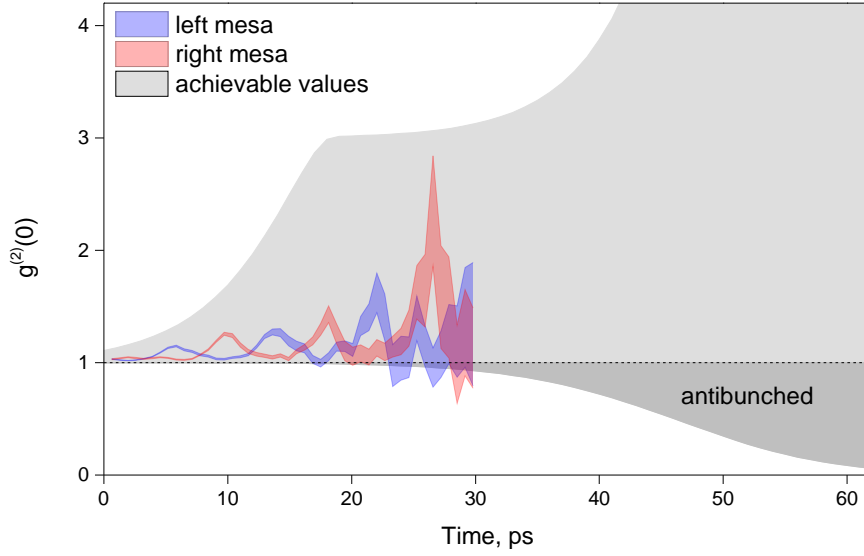


Figure 6.8: Achievable values of $g^{(2)}(0)$ (gray shaded) for realistic squeezing magnitudes r involved in the experiment, and arbitrary values of $\cos(\theta - 2\varphi)$. Blue and red shaded areas show experimentally measured $g^{(2)}(0)$ values.

the observation of superbunching with $g^{(2)}(0) > 3$. Generally speaking, this regime, shown with brown regions in Figure 6.7, would be more easily achievable for the large squeezing magnitudes.

Considering the Josephson junction, the proper phase relation can only be met at a certain phase of the Josephson oscillations. As a consequence, $g^{(2)}(0)(t)$ is expected to oscillate between values below 1 and above 1 as shown in Ref. [131]. Unfortunately, the regime of low occupancies remained inaccessible with our experimental layout. Particularly, for the data presented in Figure 6.5, the polariton population is in the range of a hundred at $t = 30$ ps, when the signal-to-noise ratio becomes insufficient to make any confident claims about the statistics of the emission. This experimental limitation is due to the imperfection of the streak-camera as a single photon detector, namely low quantum efficiency of the photocathode, as well as high dark noise of the streak-camera tube. The weakest light detectable in this layout is estimated to correspond to about 50 polaritons in the system. From equation (2.58), this corresponds to the $g^{(2)}(0)$ not less than 0.98, which is clearly too high for confident claims of the antibunching.

To further clarify this point, we demonstrate the range of accessible $g^{(2)}(0)$ at every moment of time in Figure 6.8. These values were calculated from Equation 2.58 for the system occupancy at any given moment of time, squeezing magnitude limited by the maximal theoretical value,

and arbitrary values of $\cos(\theta - 2\varphi)$. As it was discussed before, for large occupancies of the system at $t < 30$ ps, $g^{(2)}(0)$ neither exceeds the value of 3, nor demonstrates any significant nonclassical features. Later on, the system occupancy drops, and $g^{(2)}(0)$ can address larger range of values. Particularly, the strong antibunching gets achievable only at $t > 40$ ps, which stays beyond the scope of our experiment. Despite the fact that the simulated values of $g^{(2)}(0)$ do not predict a non-classical statistics for the particular parameters used in simulations, the antibunching in an analogous system would result from the vary same mechanism [131].

6.6.3 Effect of the streak-camera resolution

The second-order correlation function is calculated based on the number of photons observed by the streak-camera CCD. The finite temporal resolution of the streak-camera implies that if the photon is detected at time t , it could have arrived in fact at a different moment of time $t - \tau$ time with a certain probability. If the latter is given by the probability density function $\nu(\tau)$, then the number of photons detected at time t is given by the convolution

$$n_{1,2}(t) = \int_{-\infty}^{+\infty} n_{1,2}^0(t) \cdot \nu(t - \tau) d\tau, \quad (6.18)$$

where $n_{1,2}^0(t)$ are the streams of photons in two arms of HBT setup before the detector. This means that the time resolution plays its role *before* the correlations are calculated in the experiment.

At the same time, the simulated $g^{(2)}(0)$ values are calculated by solving the mean field and quantum master equation. Therefore, one can account for the time resolution (by calculating the convolution, for example) only *after* the calculation of $g^{(2)}(0)$, which is clearly not the same as what is measured in the experiment. As a rough approximation, we present the simulated $g^{(2)}(0)$ convolved with the Gaussian representing the streak-camera resolution in Figure 6.9 with black dashed lines. Even though it is not expected to coincide perfectly with the experimental data, it does mimic the periodic oscillations of the $g^{(2)}(0)$ function quite reasonably. An accurate description of the time resolution would be possible using Monte-Carlo simulations. Nevertheless, this would require considerable time and computational resources without any noticeable change in the observations.

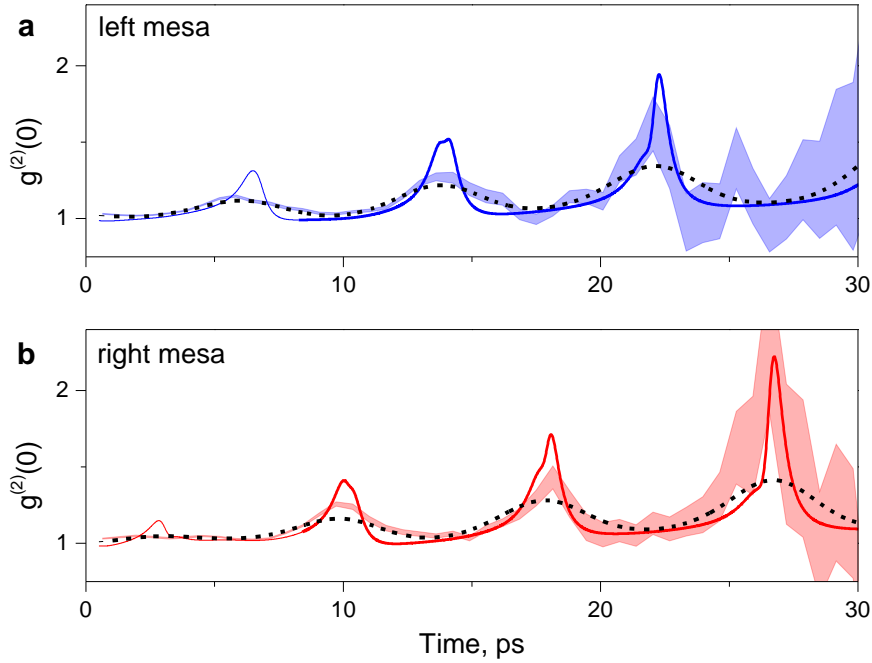


Figure 6.9: Effect of the convolution on simulated $g^{(2)}(0)$ values in (a) left mesa, and (b) right mesa. Shaded areas: experimentally measured $g^{(2)}(0)$; solid lines: simulated $g^{(2)}(0)$; black dashed lines: same, but convoluted with a Gaussian with FWHM = 3.4 ps representing the resolution of the streak-camera.

6.6.4 Repeatability of the experiment

In order to confirm the robustness of the effect, the experiment was repeated in various experimental conditions. Particularly, we changed the excitation laser power, the initial population imbalance between two mesas, and the exciton-photon detuning in the Josephson junction. The results of six different experiments are presented in Figure 6.10. This Figure unambiguously proves that the main qualitative feature — oscillations of the light statistics between the Poissonian and super-Poissonian one, with opposite phases between two mesas — is present for any initial conditions.

At the same time, the main quantitative characteristic, which is the degree of bunching, can be different even if the experiment is repeated on the same Josephson junction with the same laser excitation power. For example, this is the case for the subplots a–b and c–d in Figure 6.10. Particularly, from the subplots c–d we see that the same laser power can lead to both strong bunching with maximal $g^{(2)}(0) > 1.8$, and weak bunching where $g^{(2)}(0)$ never exceeds 1.2.

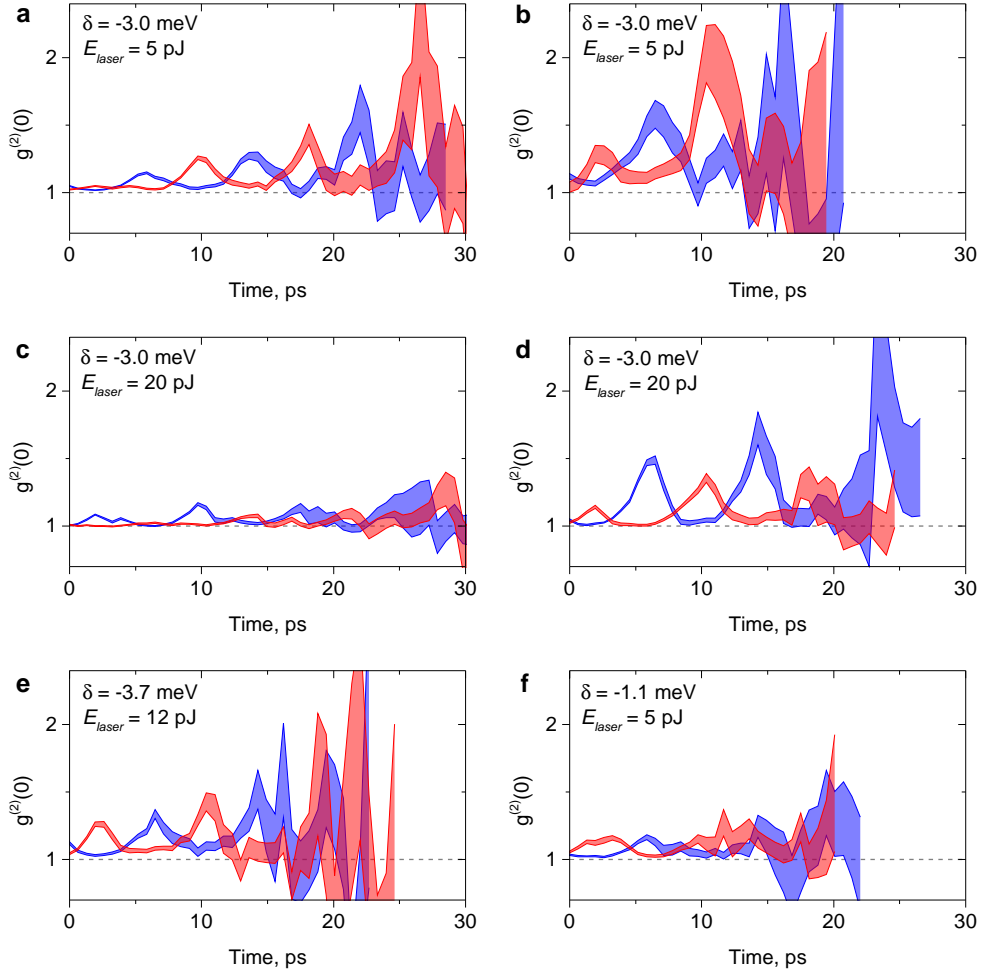


Figure 6.10: Measured $g^{(2)}(0)$ at different experimental conditions. Data in (a) are the same as in Figures 6.3 and 6.5. The exciton-photon detuning δ and the energy of the exciting laser pulse are given in each plot.

One possible explanation of this feature is the difference of the initial population imbalance imprinted by the laser in different experiments. In fact, this quantity was barely accessible with our measurements, and thus was not thoughtfully controlled. This was due to the resolution of the streak-camera, which may hinder the actual initial population imbalance like in Figure 6.5a. The only important condition for the experiment is that the laser should not excite both mesas of the Josephson junction equally, because as we discussed before, such symmetry will prevent the system from starting the oscillations. The effect of the initial population imbalance on the light statistics is highlighted in [131], therefore confirming the importance of its control.

Data in Figure 6.10 e–f were acquired for two other Josephson junctions with the exciton-photon detuning that differs from the one in subplots a–d. They demonstrate qualitatively the same oscillations of the light statistics, even though the amplitude of oscillations for the most positively detuned junction (Figure 6.10 f) is very low. Nevertheless, this cannot be sufficient to claim any dependence of the effect on the exciton-photon detuning, since similarly low degree of bunching was also observed for a different junction Figure 6.10 c. Therefore, for this set of experimental data, the low degree of bunching can be explained by the certain value of the initial population imbalance. Currently this is the only data set that was acquired for this particular exciton-photon detuning.

The detailed study of the roles of the detuning and the initial population imbalance would require an additional thorough research. While the detuning can easily be varied thanks to the wedge during the growth of the microcavity, the initial imbalance can be estimated from the distance between the excitation laser spot and the center of the Josephson junction. The zero distance could be found from the absence of Josephson oscillations, because in this case the laser spot would excite both mesas equally. The movement from the zero distance could be measured by using piezo actuators, and the corresponding population imbalance could be estimated given that the size of the laser spot and the dimensions of the Josephson junction are known.

6.6.5 Two-dimensional correlation map

More subtle features of the oscillating light statistics can be resolved when measuring the correlations between the photons arriving at different moments of time, $g^{(2)}(t_1, t_2)$ (Figure 6.11 a). The most salient feature of the plot are the local maxima of $g^{(2)}(t_1, t_2)$ correlation function that are arranged on a rectangular lattice. We compare the $g^{(2)}(t_1, t_2)$ plot with the numerical simulations shown in Figure 6.11 b and observe that the latter perfectly mimics the arrangement of the maxima of $g^{(2)}(t_1, t_2)$ in a rectangular lattice, as well as the amplitude of these maxima that increases with time. This confirms that this effect originates from periodical squeezing. The difference in the amplitude and sharpness of these peaks results from the temporal resolution of our experiment.

The simulated values of the two-time second-order correlations are obtained by summing all possible second-order truncations of the fourth-order correlations. More details on the calculations can be found in [131].

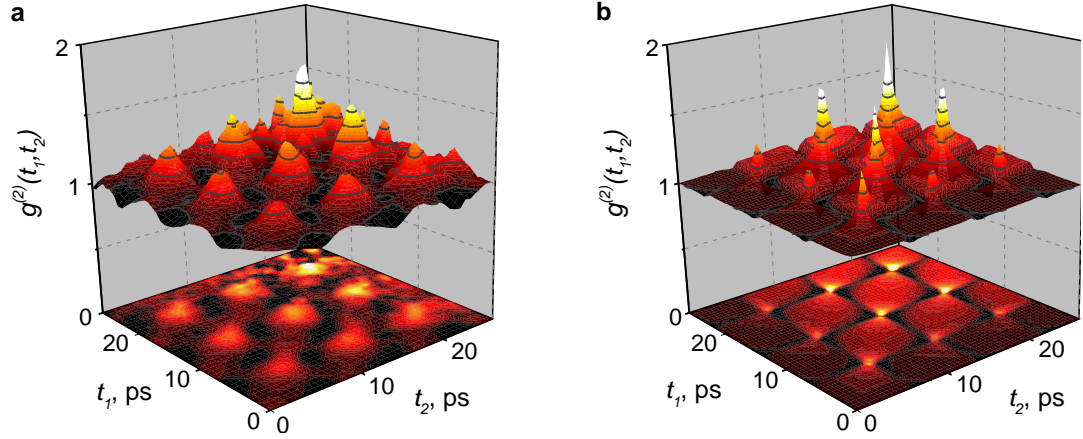


Figure 6.11: Two-dimensional correlation function $g^{(2)}(t_1, t_2)$. (a) Measured $g^{(2)}(t_1, t_2)$ for the emission from the left mesa. (b) Simulated $g^{(2)}(t_1, t_2)$. The arrangement of the regions where $g^{(2)}(t_1, t_2) > 1$ in a rectangular grid is well represented by the simulations.

6.7 Conclusion

In this Chapter, we examined the second-order coherence of light emitted from the polariton Josephson junction. It was shown that the interplay of Josephson coupling with the intrinsic weak nonlinearity of polaritons can lead to dramatic changes in the light statistics. Even more, the very regime of Josephson oscillations allows to periodically change the ratio between the populations of two mesas, thus controlling the degree of the field squeezing. As a consequence, the polariton Josephson junction creates a squeezed coherent state, parameters of which change periodically in time. Our measurements shed light on the nature of nonclassical phenomena in the photonic two-mode systems, and can motivate further research in other photonic systems with coupling like photonic crystals [80] or microwave Josephson junctions [133].

7 Perspectives

In this Chapter, we will discuss a few possible directions of future research on the coherence properties of polaritonic system. Particularly, we will mention new experiments that can be promising for future studies with the dedicated setup.

7.1 Unconventional photon blockade

An up-to-date understanding of the unconventional polariton blockade mechanism that was introduced in Chapter 2.5, associates this effects with the squeezing of coherent states. In principle, this state can become non-Gaussian to a certain degree due to the higher-order terms in equation (6.14), but this is only possible at very low occupancies of the system. This undoubtedly means that the nonclassical statistics arising from this elusive phenomenon can only be detected when there are only few particles present in the system. At these occupancies, the system of two coupled nonlinear modes acts as a quantum filter that perturbs the Poissonian statistics of coherent excitation, reducing the probability of having two photons, but increasing the chance of having three photons [131]. Interestingly enough, the probability of having one single photon in the output is not changed, and therefore this mechanism cannot be considered as a tool to generate a single photon Fock state.

The main drawback of the streak-camera is its low quantum efficiency, which is mostly due to the probability to produce the electron when an infrared photon hits the photocathode of the streak-tube. Recently, a new generation of fast single-photon detectors has appeared, which essentially are constituted of superconductive nanowires that are sensitive to light. The time resolution of these detectors can be as high as 20 ps with a quantum efficiency exceeding

60 %. Furthermore, they can be used at the repetition rate of the mode-locked laser, thus decreasing the data acquisition time to few minutes only. Currently, the period of Josephson oscillations in polaritonic systems [19, 134] stays shorter than the time resolution of these detectors; nevertheless, it can certainly be increased by properly tuning the distance between the traps. Furthermore, instead of using the Josephson coupling of two spatially separated modes, one may use two polarization states in a single round polariton trap. This allows to control the splitting between two modes by tuning the asymmetry of the trap, and also increase its size, thus decreasing the inhomogeneous broadening of polariton lines due to the lower interaction with the surface defects on the sides of the potential traps. To the best of our knowledge, the experiment of this kind with using two superconductor nanowires for correlation measurements is currently being planned in Innsbruck.

Another proposal of interest might be detection of the photon statistics in a way similar to the up-conversion spectroscopy. In this layout, the beam of photons under study of energy $h\nu_1$ is mixed with a short but strong laser pulse with photon energy $h\nu_2$ on a nonlinear crystal. The wavelengths of the two beams and the orientation of the crystal are tuned to allow for sum frequency generation $h\nu_{\text{sum}} = h\nu_1 + h\nu_2$. Therefore, the laser pulse can be used as a sampler that can select a moment of time for which the sum frequency will be generated, thus giving a resolution of ~ 300 fs. The stochastic nature of the up-conversion process assures that the statistics of studied photons will be inherited by the up-converted signal, which can be subsequently detected by APDs in a Hanbury Brown and Twiss setup. An extra bonus comes from the fact that the up-converted signal of the InGaAs microcavity emission ($\lambda \approx 840$ nm) will be in the blue region, for which the detectors can have very high sensitivity.

The main difficulty for such an experiment is that one cannot use the same laser for resonant excitation of the microcavity and as a beam sampler. In this case $h\nu_1 = h\nu_2$, and the generation of the second harmonics from the powerful sampling laser will act as a very strong noise source that will prevent observation of the single photon statistics. Ideally, one should use different wavelengths of the studied light and sampling laser. This would require the use of two mode-locked lasers, which is barely possible, or alternatively of a tunable optical parametric amplifier, a much more tractable solution.

Finally, properties of the squeezed light produced by the Josephson junction can further be studied using the homodyne detection of the quantum state [135]. In this case, the signal from the microcavity is mixed with a local oscillator on a beamsplitter, and the signals in the two outputs are studied with the balanced detector. The role of the local oscillator can be played by

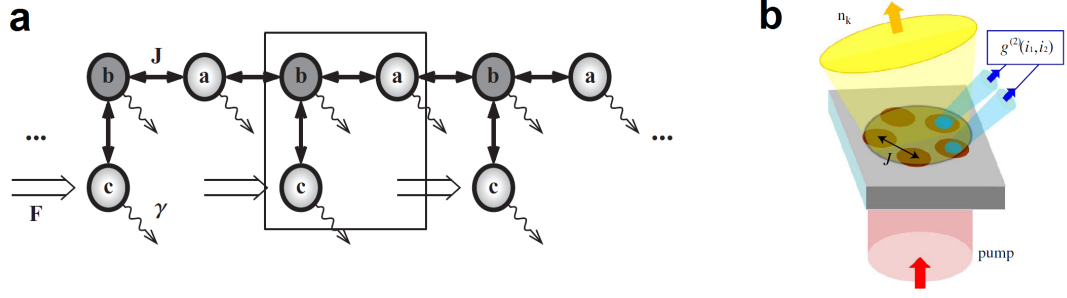


Figure 7.1: (a) Driven-dissipative Lieb lattice. Driving only the sides marked c leads to emergence of strong correlations. Represented from [136]. (b) Chain of polariton traps folded in a “necklace” geometry. Represented from [137].

the laser pulse used to excite the microcavity, and a controllable delay can be used for the time sampling. Even though the nonclassical statistics of light cannot be accessed with this type of measurements, the interest in quantum state tomography comes from the fact that it gives access to both the magnitude and the angle of the squeezing, thus allowing for a thorough comparison of the experimental measurements with the theoretical model (Chapter 6.5).

From the experimental point of view, the homodyne detection is subject to two main difficulties. First of all, it is very critical to the quantum efficiency of detection, which requires use of the wavelength-matched photodiodes, minimal amount of optics, and perfect spatial matching of the microcavity emission mode with the local oscillator beam. Particularly, these were the prerequisites for the previous observations of the quadrature squeezing in polaritonic system [25, 26]. Second, the phase delay between the microcavity emission and the local oscillator has to be fixed, thus requiring active stabilization using a technique similar to the one used to stabilize the Michelson interferometer (Chapter 3.2.4). An additional difficulty comes from the fact that this stabilization has to be performed through the microcavity. Although this is realizable (e.g. by using the laser diodes with a wavelengths for which the microcavity is transparent), assembly of the whole experiment may require significant efforts.

7.2 Correlation measurements in other geometries

To access the strongly correlated photons in a polaritonic system, one can move from the system of two coupled photonic modes to more complicated geometries. In fact, the driven-dissipative nature of the polaritonic system allows to obtain various stationary or dynamical solutions depending on the relation between excitation and losses. In certain types of poten-

tials, nonclassical states can emerge under specific excitation conditions. Particularly, such behavior is expected to occur in frustrated geometries [138], one bright example of which is the Lieb lattice, theoretically described in [136] and schematically shown in Figure 7.1a. Here, selective excitation of particular sides of the lattice can lead to emergence of strongly correlated photons in the system.

The Lieb lattice is essentially a linear geometry. However, strong photon correlation can also occur in the looped system, where the one-dimensional chain of coupled potential traps is folded into a “necklace” (Figure 7.1b). Such a geometry applied to microcavity polaritons was first described in [137]. In this case, the interactions lead to strong correlations in the system, which could be evidenced by optical transmission or second-order coherence measurements. If the nonlinearity is further increased, one can expect even stronger photonic correlation leading to “fermionization” of the photons in the system.

7.3 Photon blockade with polaritons

The concept of the photon blockade was introduced in Chapter 2.5. To remind shortly, if the repulsive interactions between the photons are stronger than the linewidth, then the system will only be able to absorb a single photon. However, if resonance excitation is used, the second photon can not be absorbed because the interaction will significantly shift the energy level for the two-photon state. Despite the visual simplicity, this concept turned out to be really hard to realize in photonic system because of very low strength of the photon-photon interaction. The use of microcavity polaritons as a nonlinear photonic system for realization of the photon blockade was proposed in [69]. Nevertheless, the polariton nonlinearity turned out to be very small, and significant renormalization of energies is predicted to be achievable only in very small polariton traps with a diameter of about 500 nm.

The fabrication of such small potential traps is in fact a significant challenge for the semiconductor processing techniques. Particularly, one of the most useful approaches, the reactive ion etching of micropillars [17], is ideal for the fabrication of large geometries, but fails to produce high-quality structures with a size of less than $\approx 2 \mu\text{m}$ due to the surface defects. The other techniques, including strain of the microcavity [46], patterning of the top DBR [16], or use of surface acoustic waves [18] cannot reach the required size of the mesas.

Recently, it turned out to be possible to fabricate the round mesas with the size down to 400 nm in our group. However, currently it is not really clear if the traditional second-order correlation

measurements with the avalanche photodiodes can be used to observe the antibunching in this system. The reason is the same as the one that forced us to assemble the photon correlation setup based on the streak-camera: the lifetime of polaritons in such small mesas is not longer than 5 ps, which is an order of magnitude less than the resolution of APDs. Even if a certain degree of antibunching is present in the system, it can be smoothed by the detector resolution. However, the use of the streak-camera under pulsed excitation will also be impossible: if the photon blockade effect is present in the system, then one laser pulse will create only one photon, which will be way below the signal-to-noise ratio of the streak-camera.

A possible solution could be found in using a resonant CW laser to excite the mesas resonantly, and a pulse picker to prevent detection of photons with large time delays between them by the streak-camera. This might give us an access to $g^{(2)}(\tau)$ correlation function with a resolution of not less than 2.2 ps. Preliminary estimations of the quantum efficiency of the detector as well as the expected signal-to-noise ratio have shown that the measurements of this kind are realizable, and therefore are of high interest to be performed in the nearest future.



Bibliography

- [1] P. Lebedew, “Untersuchungen über die druckkräfte des lichtetes,” *Annalen der Physik*, vol. 311, no. 11, pp. 433–458, 1901.
- [2] A. Einstein, “Über einen die erzeugung und verwandlung des lichtetes betreffenden heuristischen gesichtspunkt,” *Annalen der physik*, vol. 322, no. 6, pp. 132–148, 1905.
- [3] H. J. Round, “A note on carborundum,” *J. Electr. World*, vol. 49, p. 308, 1907.
- [4] O. Lossev, “Luminous carborundum detector and detection effect and oscillations with crystals,” *The London, Edinburgh, and Dublin Philosophical Magazine and Journal of Science*, vol. 6, no. 39, pp. 1024–1044, 1928.
- [5] E. M. Purcell, H. C. Torrey, and R. V. Pound, “Resonance absorption by nuclear magnetic moments in a solid,” *Physical review*, vol. 69, no. 1-2, p. 37, 1946.
- [6] S. Haroche and D. Kleppner, “Cavity quantum electrodynamics,” *Phys. Today*, vol. 42, no. 1, pp. 24–30, 1989.
- [7] J. Hopfield, “Theory of the contribution of excitons to the complex dielectric constant of crystals,” *Physical Review*, vol. 112, no. 5, p. 1555, 1958.
- [8] C. Weisbuch, M. Nishioka, A. Ishikawa, and Y. Arakawa, “Observation of the coupled exciton-photon mode splitting in a semiconductor quantum microcavity,” *Physical Review Letters*, vol. 69, no. 23, p. 3314, 1992.
- [9] J. Kasprzak, *Condensation of exciton polaritons*. PhD thesis, Université Joseph-Fourier-Grenoble I, 2006.
- [10] A. Amo, J. Lefrère, S. Pigeon, C. Adrados, C. Ciuti, I. Carusotto, R. Houdré, E. Giacobino, and A. Bramati, “Superfluidity of polaritons in semiconductor microcavities,” *Nature Physics*, vol. 5, no. 11, pp. 805–810, 2009.

Bibliography

- [11] K. G. Lagoudakis, M. Wouters, M. Richard, A. Baas, I. Carusotto, R. André, L. S. Dang, and B. Deveaud-Plédran, “Quantized vortices in an exciton–polariton condensate,” *Nature Physics*, vol. 4, no. 9, pp. 706–710, 2008.
- [12] K. Lagoudakis, T. Ostatnický, A. Kavokin, Y. G. Rubo, R. André, and B. Deveaud-Plédran, “Observation of half-quantum vortices in an exciton-polariton condensate,” *Science*, vol. 326, no. 5955, pp. 974–976, 2009.
- [13] A. Amo, S. Pigeon, D. Sanvitto, V. Sala, R. Hivet, I. Carusotto, F. Pisanello, G. Leménager, R. Houdré, E. Giacobino, *et al.*, “Polariton superfluids reveal quantum hydrodynamic solitons,” *Science*, vol. 332, no. 6034, pp. 1167–1170, 2011.
- [14] S. Utsunomiya, L. Tian, G. Roumpos, C. Lai, N. Kumada, T. Fujisawa, M. Kuwata-Gonokami, A. Löffler, S. Höfling, A. Forchel, *et al.*, “Observation of bogoliubov excitations in exciton-polariton condensates,” *Nature Physics*, vol. 4, no. 9, p. 700, 2008.
- [15] O. El Daïf, A. Baas, T. Guillet, J.-P. Brantut, R. I. Kaitouni, J.-L. Staehli, F. Morier-Genoud, and B. Deveaud, “Polariton quantum boxes in semiconductor microcavities,” *Applied Physics Letters*, vol. 88, no. 6, p. 061105, 2006.
- [16] C. Lai, N. Kim, S. Utsunomiya, G. Roumpos, H. Deng, M. Fraser, T. Byrnes, P. Recher, N. Kumada, T. Fujisawa, *et al.*, “Coherent zero-state and π -state in an exciton–polariton condensate array,” *Nature*, vol. 450, no. 7169, pp. 529–532, 2007.
- [17] D. Bajoni, P. Senellart, E. Wertz, I. Sagnes, A. Miard, A. Lemaître, and J. Bloch, “Polariton laser using single micropillar GaAs–GaAlAs semiconductor cavities,” *Phys. Rev. Lett.*, vol. 100, p. 047401, Jan 2008.
- [18] E. Cerda-Méndez, D. Krizhanovskii, M. Wouters, R. Bradley, K. Biermann, K. Guda, R. Hey, P. Santos, D. Sarkar, and M. Skolnick, “Polariton condensation in dynamic acoustic lattices,” *Physical review letters*, vol. 105, no. 11, p. 116402, 2010.
- [19] M. Abbarchi, A. Amo, V. Sala, D. Solnyshkov, H. Flayac, L. Ferrier, I. Sagnes, E. Galopin, A. Lemaître, G. Malpuech, *et al.*, “Macroscopic quantum self-trapping and josephson oscillations of exciton polaritons,” *Nature Physics*, vol. 9, no. 5, pp. 275–279, 2013.
- [20] T. Jacqmin, I. Carusotto, I. Sagnes, M. Abbarchi, D. Solnyshkov, G. Malpuech, E. Galopin, A. Lemaître, J. Bloch, and A. Amo, “Direct observation of dirac cones and a flatband in a honeycomb lattice for polaritons,” *Physical review letters*, vol. 112, no. 11, p. 116402, 2014.

- [21] N. G. Berloff, K. Kalinin, M. Silva, W. Langbein, and P. G. Lagoudakis, “Realizing the xy hamiltonian in polariton simulators,” *arXiv preprint arXiv:1607.06065*, 2016.
- [22] M. Milićević, T. Ozawa, P. Andreakou, I. Carusotto, T. Jacqmin, E. Galopin, A. Lemaitre, L. Le Gratiet, I. Sagnes, J. Bloch, *et al.*, “Edge states in polariton honeycomb lattices,” *2D Materials*, vol. 2, no. 3, p. 034012, 2015.
- [23] S. Demirchyan, I. Y. Chestnov, A. Alodjants, M. Glazov, and A. Kavokin, “Qubits based on polariton rabi oscillators,” *Physical review letters*, vol. 112, no. 19, p. 196403, 2014.
- [24] T. C. H. Liew and V. Savona, “Single photons from coupled quantum modes,” *Phys. Rev. Lett.*, vol. 104, p. 183601, May 2010.
- [25] J. P. Karr, A. Baas, R. Houdré, and E. Giacobino, “Squeezing in semiconductor microcavities in the strong-coupling regime,” *Physical Review A*, vol. 69, no. 3, p. 031802, 2004.
- [26] T. Boulier, M. Bamba, A. Amo, C. Adrados, A. Lemaitre, E. Galopin, I. Sagnes, J. Bloch, C. Ciuti, E. Giacobino, and A. Bramati, “Polariton-generated intensity squeezing in semiconductor micropillars,” *Nature communications*, vol. 5, p. 3260, 2014.
- [27] J. Wiersig, C. Gies, F. Jahnke, M. Aßmann, T. Berstermann, M. Bayer, C. Kistner, S. Reitzenstein, C. Schneider, S. Höfling, *et al.*, “Direct observation of correlations between individual photon emission events of a microcavity laser,” *Nature*, vol. 460, no. 7252, pp. 245–249, 2009.
- [28] M. Aßmann, F. Veit, M. Bayer, M. van Der Poel, and J. M. Hvam, “Higher-order photon bunching in a semiconductor microcavity,” *Science*, vol. 325, no. 5938, pp. 297–300, 2009.
- [29] J. Schmutzler, T. Kazimierczuk, O. Bayraktar, M. Aßmann, M. Bayer, S. Brodbeck, M. Kamp, C. Schneider, and S. Höfling, “Influence of interactions with noncondensed particles on the coherence of a one-dimensional polariton condensate,” *Phys. Rev. B*, vol. 89, p. 115119, Mar 2014.
- [30] V. G. Sala, F. Marsault, M. Wouters, E. Galopin, I. Sagnes, A. Lemaître, J. Bloch, and A. Amo, “Stochastic precession of the polarization in a polariton laser,” *Phys. Rev. B*, vol. 93, p. 115313, Mar 2016.
- [31] M. Cardona and P. Yu, *Fundamentals of semiconductors*. Springer, 2005.

Bibliography

- [32] J. Singh, *Electronic and optoelectronic properties of semiconductor structures*. Cambridge University Press, 2007.
- [33] T. Kazimierczuk, D. Fröhlich, S. Scheel, H. Stolz, and M. Bayer, “Giant rydberg excitons in the copper oxide Cu_2O ,” *Nature*, vol. 514, no. 7522, p. 343, 2014.
- [34] R. Cerna, *On Zero-Dimensional Exciton-Polaritons*. PhD thesis, EPFL, 2011.
- [35] M. C. Teich and B. Saleh, “Fundamentals of photonics,” *Canada, Wiley Interscience*, vol. 3, 1991.
- [36] O. Svelto and D. C. Hanna, *Principles of lasers*, vol. 4. Springer, 1998.
- [37] V. Savona, C. Piermarocchi, A. Quattropani, P. Schwendimann, and F. Tassone, “Optical properties of microcavity polaritons,” *Phase transitions*, vol. 68, no. 1, pp. 169–279, 1999.
- [38] G. Grosso, *Hydrodynamics and nonlinear phenomena in polariton fluids*. PhD thesis, EPFL, 2014.
- [39] V. Savona, F. Tassone, C. Piermarocchi, A. Quattropani, and P. Schwendimann, “Theory of polariton photoluminescence in arbitrary semiconductor microcavity structures,” *Physical Review B*, vol. 53, no. 19, p. 13051, 1996.
- [40] S. Bose, “Planck’s law and light quantum hypothesis,” *Z. Phys*, vol. 26, no. 1, p. 178, 1924.
- [41] A. Einstein, *Quantentheorie des einatomigen idealen Gases*. Akademie der Wissenschaften, in Kommission bei W. de Gruyter, 1924.
- [42] L. Pitaevskii and S. Stringari, *Bose-Einstein condensation and superfluidity*, vol. 164. Oxford University Press, 2016.
- [43] M. H. Anderson, J. R. Ensher, M. R. Matthews, C. E. Wieman, and E. A. Cornell, “Observation of bose-einstein condensation in a dilute atomic vapor,” *science*, vol. 269, no. 5221, p. 198, 1995.
- [44] K. B. Davis, M. O. Mewes, M. R. Andrews, N. J. van Druten, D. S. Durfee, D. M. Kurn, and W. Ketterle, “Bose-einstein condensation in a gas of sodium atoms,” *Phys. Rev. Lett.*, vol. 75, pp. 3969–3973, Nov 1995.
- [45] J. Kasprzak, M. Richard, S. Kundermann, A. Baas, P. Jeambrun, J. Keeling, F. Marchetti, M. Szymańska, R. Andre, J. Staehli, V. Savona, P. B. Littlewood, B. Deveaud, and L. S.

- Dang, “Bose-Einstein condensation of exciton polaritons,” *Nature*, vol. 443, no. 7110, pp. 409–414, 2006.
- [46] R. Balili, V. Hartwell, D. Snoke, L. Pfeiffer, and K. West, “Bose–Einstein condensation of microcavity polaritons in a trap,” *Science*, vol. 316, no. 5827, pp. 1007–1010, 2007.
- [47] J. Baumberg, A. Kavokin, S. Christopoulos, A. Grundy, R. Butté, G. Christmann, D. Solnyshkov, G. Malpuech, G. B. H. von Högersthal, E. Feltin, *et al.*, “Spontaneous polarization buildup in a room-temperature polariton laser,” *Physical review letters*, vol. 101, no. 13, p. 136409, 2008.
- [48] S. Kéna-Cohen and S. Forrest, “Room-temperature polariton lasing in an organic single-crystal microcavity,” *Nature Photonics*, vol. 4, no. 6, pp. 371–375, 2010.
- [49] J. D. Plumhof, T. Stöferle, L. Mai, U. Scherf, and R. F. Mahrt, “Room-temperature bose-einstein condensation of cavity exciton-polaritons in a polymer,” *Nature materials*, vol. 13, no. 3, p. 247, 2014.
- [50] K. Daskalakis, S. Maier, R. Murray, and S. Kéna-Cohen, “Nonlinear interactions in an organic polariton condensate,” *Nature materials*, vol. 13, no. 3, p. 271, 2014.
- [51] H. Deng, H. Haug, and Y. Yamamoto, “Exciton-polariton bose-einstein condensation,” *Reviews of Modern Physics*, vol. 82, no. 2, p. 1489, 2010.
- [52] Y. Sun, P. Wen, Y. Yoon, G. Liu, M. Steger, L. N. Pfeiffer, K. West, D. W. Snoke, and K. A. Nelson, “Bose-einstein condensation of long-lifetime polaritons in thermal equilibrium,” *Physical review letters*, vol. 118, no. 1, p. 016602, 2017.
- [53] B. Deveaud-Plédran, “On the condensation of polaritons,” *J. Opt. Soc. Am. B*, vol. 29, pp. A138–A145, Feb 2012.
- [54] L. Ferrier, E. Wertz, R. Johne, D. D. Solnyshkov, P. Senellart, I. Sagnes, A. Lemaître, G. Malpuech, and J. Bloch, “Interactions in confined polariton condensates,” *Physical Review Letters*, vol. 106, no. 12, p. 126401, 2011.
- [55] K. G. Lagoudakis, B. Pietka, M. Wouters, R. André, and B. Deveaud-Plédran, “Coherent oscillations in an exciton-polariton Josephson junction,” *Phys. Rev. Lett.*, vol. 105, p. 120403, Sep 2010.
- [56] M. Wouters and I. Carusotto, “Excitations in a nonequilibrium bose-einstein condensate of exciton polaritons,” *Physical review letters*, vol. 99, no. 14, p. 140402, 2007.

Bibliography

- [57] M. Wouters, I. Carusotto, and C. Ciuti, “Spatial and spectral shape of inhomogeneous nonequilibrium exciton-polariton condensates,” *Physical Review B*, vol. 77, no. 11, p. 115340, 2008.
- [58] K. G. Lagoudakis, F. Manni, B. Pietka, M. Wouters, T. C. H. Liew, V. Savona, A. V. Kavokin, R. André, and B. Deveaud-Plédran, “Probing the dynamics of spontaneous quantum vortices in polariton superfluids,” *Phys. Rev. Lett.*, vol. 106, p. 115301, Mar 2011.
- [59] M. Fox, *Quantum optics: an introduction*, vol. 15. OUP Oxford, 2006.
- [60] C. Gerry and P. Knight, *Introductory Quantum Optics*. Cambridge University Press, 2005.
- [61] M. Orszag, *Quantum optics: including noise reduction, trapped ions, quantum trajectories, and decoherence*. Springer, 2016.
- [62] D. F. Walls and G. J. Milburn, *Quantum optics*. Springer Science & Business Media, 2007.
- [63] R. J. Glauber, “The quantum theory of optical coherence,” *Phys. Rev.*, vol. 130, pp. 2529–2539, Jun 1963.
- [64] R. Hanbury Brown and R. Twiss, “Correlation between photons in two coherent beams of light,” *Nature*, vol. 177, pp. 27–32, 1956.
- [65] N. Gisin, G. Ribordy, W. Tittel, and H. Zbinden, “Quantum cryptography,” *Rev. Mod. Phys.*, vol. 74, pp. 145–195, Mar 2002.
- [66] J. L. O’Brien, “Optical quantum computing,” *Science*, vol. 318, no. 5856, pp. 1567–1570, 2007.
- [67] J. Gea-Banacloche and G. Leuchs, “Squeezed states for interferometric gravitational-wave detectors,” *Journal of Modern Optics*, vol. 34, no. 6-7, pp. 793–811, 1987.
- [68] C. Kurtsiefer, S. Mayer, P. Zarda, and H. Weinfurter, “Stable solid-state source of single photons,” *Phys. Rev. Lett.*, vol. 85, pp. 290–293, Jul 2000.
- [69] A. Imamoglu, H. Schmidt, G. Woods, and M. Deutsch, “Strongly interacting photons in a nonlinear cavity,” *Physical Review Letters*, vol. 79, no. 8, p. 1467, 1997.
- [70] K. M. Birnbaum, A. Boca, R. Miller, A. D. Boozer, T. E. Northup, and H. J. Kimble, “Photon blockade in an optical cavity with one trapped atom,” *Nature*, vol. 436, no. 7047, pp. 87–90, 2005.

- [71] T. Pittman, B. Jacobs, and J. Franson, “Heralding single photons from pulsed parametric down-conversion,” *Optics communications*, vol. 246, no. 4, pp. 545–550, 2005.
- [72] L. S. Collaboration *et al.*, “A gravitational wave observatory operating beyond the quantum shot-noise limit,” *Nature Physics*, vol. 7, no. 12, pp. 962–965, 2011.
- [73] H.-A. Bachor, T. C. Ralph, S. Lucia, and T. C. Ralph, *A guide to experiments in quantum optics*, vol. 1. wiley-vch Weinheim, 2004.
- [74] M. Bamba, A. Imamoğlu, I. Carusotto, and C. Ciuti, “Origin of strong photon antibunching in weakly nonlinear photonic molecules,” *Physical Review A*, vol. 83, no. 2, p. 021802, 2011.
- [75] S. Ferretti, L. C. Andreani, H. E. Türeci, and D. Gerace, “Photon correlations in a two-site nonlinear cavity system under coherent drive and dissipation,” *Phys. Rev. A*, vol. 82, p. 013841, Jul 2010.
- [76] S. Ferretti, V. Savona, and D. Gerace, “Optimal antibunching in passive photonic devices based on coupled nonlinear resonators,” *New Journal of Physics*, vol. 15, no. 2, p. 025012, 2013.
- [77] H. Flayac and V. Savona, “Input-output theory of the unconventional photon blockade,” *Phys. Rev. A*, vol. 88, p. 033836, Sep 2013.
- [78] M. Bamba and C. Ciuti, “Counter-polarized single-photon generation from the auxiliary cavity of a weakly nonlinear photonic molecule,” *Applied Physics Letters*, vol. 99, no. 17, p. 171111, 2011.
- [79] X.-W. Xu and Y.-J. Li, “Antibunching photons in a cavity coupled to an optomechanical system,” *Journal of Physics B: Atomic, Molecular and Optical Physics*, vol. 46, no. 3, p. 035502, 2013.
- [80] H. Flayac, D. Gerace, and V. Savona, “An all-silicon single-photon source by unconventional photon blockade,” *Scientific reports*, vol. 5, 2015.
- [81] M.-A. Lemonde, N. Didier, and A. A. Clerk, “Antibunching and unconventional photon blockade with gaussian squeezed states,” *Physical Review A*, vol. 90, no. 6, p. 063824, 2014.

Bibliography

- [82] M. Richard, J. Kasprzak, R. Romestain, R. André, and L. S. Dang, “Spontaneous coherent phase transition of polaritons in CdTe microcavities,” *Phys. Rev. Lett.*, vol. 94, p. 187401, May 2005.
- [83] A. Baas, K. G. Lagoudakis, M. Richard, R. André, L. S. Dang, and B. Deveaud-Plédran, “Synchronized and desynchronized phases of exciton-polariton condensates in the presence of disorder,” *Phys. Rev. Lett.*, vol. 100, p. 170401, Apr 2008.
- [84] F. Manni, K. Lagoudakis, R. André, M. Wouters, and B. Deveaud, “Penrose-onsager criterion validation in a one-dimensional polariton condensate,” *Physical review letters*, vol. 109, no. 15, p. 150409, 2012.
- [85] P. Lugan, D. Sarchi, and V. Savona, “Theory of trapped polaritons in patterned microcavities,” *physica status solidi (c)*, vol. 3, no. 7, pp. 2428–2431, 2006.
- [86] F. Manni, *Coherence and topological defects in exciton-polariton condensates*. PhD thesis, EPFL, 2013.
- [87] M. Wehner, M. Ulm, and M. Wegener, “Scanning interferometer stabilized by use of pancharatnam’s phase,” *Optics letters*, vol. 22, no. 19, pp. 1455–1457, 1997.
- [88] K. Lagoudakis, *On the Physics of Exciton-Polariton Condensates*. PhD thesis, EPFL, 2010.
- [89] G. Nardin, K. G. Lagoudakis, M. Wouters, M. Richard, A. Baas, R. André, L. S. Dang, B. Pietka, and B. Deveaud-Plédran, “Dynamics of long-range ordering in an exciton-polariton condensate,” *Phys. Rev. Lett.*, vol. 103, p. 256402, Dec 2009.
- [90] D. N. Krizhanovskii, K. G. Lagoudakis, M. Wouters, B. Pietka, R. A. Bradley, K. Guda, D. M. Whittaker, M. S. Skolnick, B. Deveaud-Plédran, M. Richard, R. André, and L. S. Dang, “Coexisting nonequilibrium condensates with long-range spatial coherence in semiconductor microcavities,” *Phys. Rev. B*, vol. 80, p. 045317, Jul 2009.
- [91] J. Kasprzak, M. Richard, A. Baas, B. Deveaud, R. André, J.-P. Poizat, and L. S. Dang, “Second-order time correlations within a polariton Bose-Einstein condensate in a cdte microcavity,” *Phys. Rev. Lett.*, vol. 100, p. 067402, Feb 2008.
- [92] A. P. D. Love, D. N. Krizhanovskii, D. M. Whittaker, R. Boucheikioua, D. Sanvitto, S. Al Rizeiqi, R. Bradley, M. S. Skolnick, P. R. Eastham, R. André, *et al.*, “Intrinsic decoherence mechanisms in the microcavity polariton condensate,” *Phys. Rev. Lett.*, vol. 101, no. 6, p. 067404, 2008.

- [93] T. Horikiri, P. Schwendimann, A. Quattropani, S. Höfling, A. Forchel, and Y. Yamamoto, “Higher order coherence of exciton-polariton condensates,” *Physical Review B*, vol. 81, no. 3, p. 033307, 2010.
- [94] M. Steger, G. Liu, B. Nelsen, C. Gautham, D. W. Snoke, R. Balili, L. Pfeiffer, and K. West, “Long-range ballistic motion and coherent flow of long-lifetime polaritons,” *Phys. Rev. B*, vol. 88, p. 235314, Dec 2013.
- [95] M. Aßmann, F. Veit, M. Bayer, C. Gies, F. Jahnke, S. Reitzenstein, S. Höfling, L. Worschech, and A. Forchel, “Ultrafast tracking of second-order photon correlations in the emission of quantum-dot microresonator lasers,” *Phys. Rev. B*, vol. 81, no. 16, p. 165314, 2010.
- [96] M. Aßmann, F. Veit, J.-S. Tempel, T. Berstermann, H. Stolz, M. van der Poel, J. M. Hvam, and M. Bayer, “Measuring the dynamics of second-order photon correlation functions inside a pulse with picosecond time resolution,” *Optics Express*, vol. 18, no. 19, pp. 20229–20241, 2010.
- [97] J. J. Baumberg, P. G. Savvidis, R. M. Stevenson, A. I. Tartakovskii, M. S. Skolnick, D. M. Whittaker, and J. S. Roberts, “Parametric oscillation in a vertical microcavity: A polariton condensate or micro-optical parametric oscillation,” *Phys. Rev. B*, vol. 62, pp. R16247–R16250, Dec 2000.
- [98] P. G. Savvidis, J. J. Baumberg, R. M. Stevenson, M. S. Skolnick, D. M. Whittaker, and J. S. Roberts, “Angle-resonant stimulated polariton amplifier,” *Phys. Rev. Lett.*, vol. 84, pp. 1547–1550, Feb 2000.
- [99] V. V. Belykh, N. N. Sibeldin, V. D. Kulakovskii, M. M. Glazov, M. A. Semina, C. Schneider, S. Höfling, M. Kamp, and A. Forchel, “Coherence expansion and polariton condensate formation in a semiconductor microcavity,” *Phys. Rev. Lett.*, vol. 110, p. 137402, Mar 2013.
- [100] F. Manni, K. Lagoudakis, T. H. Liew, R. André, V. Savona, and B. Deveaud, “Dissociation dynamics of singly charged vortices into half-quantum vortex pairs,” *Nature communications*, vol. 3, p. 1309, 2012.
- [101] Y. Sun, P. Wen, Y. Yoon, G. Liu, M. Steger, L. N. Pfeiffer, K. West, D. W. Snoke, and K. A. Nelson, “Bose-einstein condensation of long-lifetime polaritons in thermal equilibrium,” *Phys. Rev. Lett.*, vol. 118, p. 016602, Jan 2017.

Bibliography

- [102] E. del Valle, D. Sanvitto, A. Amo, F. P. Laussy, R. André, C. Tejedor, and L. Viña, “Dynamics of the formation and decay of coherence in a polariton condensate,” *Phys. Rev. Lett.*, vol. 103, p. 096404, Aug 2009.
- [103] L. Kłopotowski, M. Martín, A. Amo, L. Viña, I. Shelykh, M. Glazov, G. Malpuech, A. Kavokin, and R. André, “Optical anisotropy and pinning of the linear polarization of light in semiconductor microcavities,” *Solid state communications*, vol. 139, no. 10, pp. 511–515, 2006.
- [104] J. Kasprzak, R. André, L. S. Dang, I. A. Shelykh, A. V. Kavokin, Y. G. Rubo, K. V. Kavokin, and G. Malpuech, “Build up and pinning of linear polarization in the bose condensates of exciton polaritons,” *Phys. Rev. B*, vol. 75, p. 045326, Jan 2007.
- [105] M. De Giorgi, D. Ballarini, P. Cazzato, G. Deligeorgis, S. I. Tsintzos, Z. Hatzopoulos, P. G. Savvidis, G. Gigli, F. P. Laussy, and D. Sanvitto, “Relaxation oscillations in the formation of a polariton condensate,” *Phys. Rev. Lett.*, vol. 112, p. 113602, Mar 2014.
- [106] N. D. Vy, H. T. Cao, D. B. T. Thoai, and H. Haug, “Time dependence of the ground-state population statistics of condensed microcavity polaritons,” *Phys. Rev. B*, vol. 80, p. 195306, Nov 2009.
- [107] A. F. Adiyatullin, M. D. Anderson, P. V. Busi, H. Abbaspour, R. André, M. T. Portella-Oberli, and B. Deveaud, “Temporally resolved second-order photon correlations of exciton-polariton bose-einstein condensate formation,” *Applied Physics Letters*, vol. 107, no. 22, p. 221107, 2015.
- [108] A. Baas, J. P. Karr, H. Eleuch, and E. Giacobino, “Optical bistability in semiconductor microcavities,” *Physical Review A*, vol. 69, no. 2, p. 023809, 2004.
- [109] D. Bajoni, E. Semenova, A. Lemaître, S. Bouchoule, E. Wertz, P. Senellart, S. Barbay, R. Kuszelewicz, and J. Bloch, “Optical bistability in a gaas-based polariton diode,” *Physical review letters*, vol. 101, no. 26, p. 266402, 2008.
- [110] G. Nardin, G. Grosso, Y. Léger, B. Pi, F. Morier-Genoud, B. Deveaud-Plédran, *et al.*, “Hydrodynamic nucleation of quantized vortex pairs in a polariton quantum fluid,” *Nature Physics*, vol. 7, no. 8, p. 635, 2011.
- [111] L. Dominici, G. Dagvadorj, J. M. Fellows, D. Ballarini, M. De Giorgi, F. M. Marchetti, B. Piccirillo, L. Marrucci, A. Bramati, G. Gigli, *et al.*, “Vortex and half-vortex dynamics in a nonlinear spinor quantum fluid,” *Science advances*, vol. 1, no. 11, p. e1500807, 2015.

- [112] B. D. Josephson, "Possible new effects in superconductive tunnelling," *Physics letters*, vol. 1, no. 7, pp. 251–253, 1962.
- [113] P. W. Anderson and J. Rowell, "Probable observation of the josephson superconducting tunneling effect," *Physical Review Letters*, vol. 10, no. 6, p. 230, 1963.
- [114] A. Barone and G. Paterno, *Physics and applications of the Josephson effect*. John Wiley and sons, 1982.
- [115] R. Gati and M. Oberthaler, "A bosonic josephson junction," *Journal of Physics B: Atomic, Molecular and Optical Physics*, vol. 40, no. 10, p. R61, 2007.
- [116] S. V. Pereverzev, A. Loshak, S. Backhaus, J. Davis, and R. Packard, "Quantum oscillations between two weakly coupled reservoirs of superfluid ^3He ," *Nature*, vol. 388, no. 6641, pp. 449–451, 1997.
- [117] J. C. Davis and R. E. Packard, "Superfluid ^3He josephson weak links," *Rev. Mod. Phys.*, vol. 74, pp. 741–773, Jul 2002.
- [118] M. Andrews, C. Townsend, H.-J. Miesner, D. Durfee, D. Kurn, and W. Ketterle, "Observation of interference between two bose condensates," *Science*, vol. 275, no. 5300, pp. 637–641, 1997.
- [119] F. Cataliotti, S. Burger, C. Fort, P. Maddaloni, F. Minardi, A. Trombettoni, A. Smerzi, and M. Inguscio, "Josephson junction arrays with bose-einstein condensates," *Science*, vol. 293, no. 5531, pp. 843–846, 2001.
- [120] M. Albiez, R. Gati, J. Fölling, S. Hunsmann, M. Cristiani, and M. K. Oberthaler, "Direct observation of tunneling and nonlinear self-trapping in a single bosonic josephson junction," *Phys. Rev. Lett.*, vol. 95, p. 010402, Jun 2005.
- [121] S. Levy, E. Lahoud, I. Shomroni, and J. Steinhauer, "The ac and dc josephson effects in a bose-einstein condensate," *Nature*, vol. 449, no. 7162, pp. 579–583, 2007.
- [122] J. Esteve, C. Gross, A. Weller, S. Giovanazzi, and M. Oberthaler, "Squeezing and entanglement in a bose-einstein condensate," *Nature*, vol. 455, no. 7217, pp. 1216–1219, 2008.
- [123] M. Kitagawa and M. Ueda, "Squeezed spin states," *Phys. Rev. A*, vol. 47, pp. 5138–5143, Jun 1993.

Bibliography

- [124] C. Gross, “Spin squeezing, entanglement and quantum metrology with bose–einstein condensates,” *Journal of Physics B: Atomic, Molecular and Optical Physics*, vol. 45, no. 10, p. 103001, 2012.
- [125] G. J. Milburn, J. Corney, E. M. Wright, and D. F. Walls, “Quantum dynamics of an atomic bose-einstein condensate in a double-well potential,” *Phys. Rev. A*, vol. 55, pp. 4318–4324, Jun 1997.
- [126] A. Smerzi, S. Fantoni, S. Giovanazzi, and S. R. Shenoy, “Quantum coherent atomic tunneling between two trapped bose-einstein condensates,” *Phys. Rev. Lett.*, vol. 79, pp. 4950–4953, Dec 1997.
- [127] S. Raghavan, A. Smerzi, S. Fantoni, and S. R. Shenoy, “Coherent oscillations between two weakly coupled bose-einstein condensates: Josephson effects, π oscillations, and macroscopic quantum self-trapping,” *Phys. Rev. A*, vol. 59, pp. 620–633, Jan 1999.
- [128] S. Raghavan, A. Smerzi, and V. M. Kenkre, “Transitions in coherent oscillations between two trapped bose-einstein condensates,” *Phys. Rev. A*, vol. 60, pp. R1787–R1790, Sep 1999.
- [129] I. Marino, S. Raghavan, S. Fantoni, S. R. Shenoy, and A. Smerzi, “Bose-condensate tunneling dynamics: Momentum-shortened pendulum with damping,” *Phys. Rev. A*, vol. 60, pp. 487–493, Jul 1999.
- [130] D. Bajoni, P. Senellart, E. Wertz, I. Sagnes, A. Miard, A. Lemaître, and J. Bloch, “Polariton laser using single micropillar GaAs–GaAlAs semiconductor cavities,” *Phys. Rev. Lett.*, vol. 100, p. 047401, Jan 2008.
- [131] H. Flayac and V. Savona, “Nonclassical statistics from a polaritonic josephson junction,” *Phys. Rev. A*, vol. 95, p. 043838, Apr 2017.
- [132] N. B. Grosse, T. Symul, M. Stobińska, T. C. Ralph, and P. K. Lam, “Measuring photon antibunching from continuous variable sideband squeezing,” *Physical review letters*, vol. 98, no. 15, p. 153603, 2007.
- [133] J. Raftery, D. Sadri, S. Schmidt, H. E. Türeci, and A. A. Houck, “Observation of a dissipation-induced classical to quantum transition,” *Physical Review X*, vol. 4, no. 3, p. 031043, 2014.

- [134] A. F. Adiyatullin, M. D. Anderson, H. Flayac, M. T. Portella-Oberli, F. Jabeen, C. Ouellet-Plamondon, G. C. Sallen, and B. Deveaud, “Periodic squeezing in a polariton josephson junction,” *arXiv preprint arXiv:1612.06906*, 2016.
- [135] A. I. Lvovsky and M. G. Raymer, “Continuous-variable optical quantum-state tomography,” *Reviews of Modern Physics*, vol. 81, no. 1, p. 299, 2009.
- [136] W. Casteels, R. Rota, F. Storme, and C. Ciuti, “Probing photon correlations in the dark sites of geometrically frustrated cavity lattices,” *Phys. Rev. A*, vol. 93, p. 043833, Apr 2016.
- [137] I. Carusotto, D. Gerace, H. E. Tureci, S. De Liberato, C. Ciuti, and A. Imamoglu, “Fermionized photons in an array of driven dissipative nonlinear cavities,” *Phys. Rev. Lett.*, vol. 103, p. 033601, Jul 2009.
- [138] S. Schmidt, “Frustrated polaritons,” *Physica Scripta*, vol. 91, no. 7, p. 073006, 2016.



Acknowledgements

This thesis would have not been written without the support of many people who accompanied me during my PhD. First of all, I am sincerely grateful to my supervisor Benoît Deveaud. I really appreciated the strong coupling between the freedom he gives in the lab, and prudent and profound discussions we had on our meetings. This gave me a unique experience of passing numerous ups and downs, and has taught that great freedom always comes with great responsibility. I also deeply thank Benoît for his readiness to discuss and share his knowledge, for his constant motivation, and for the fascinating atmosphere in the group he always created.

I am immensely indebted to my co-supervisor Marcia Portella-Oberli. Her great care to the details has taught me how one can look at the same work from absolutely different points of view. I deeply appreciate her patience and assistance she provided when showing me various aspects of the polariton research. It has been a unforgettable experience to work with two such brilliant supervisors.

My sincere appreciation goes to Prof. Manfred Bayer, Prof. Alberto Bramati, and Prof. Vincenzo Savona who agreed to be the experts of my jury, and to Prof. Marco Grioni for being a president of it. It has been a great honor for me to have their evaluation and comments on the work I have done.

I deeply thank Mitchell Anderson for the great time we had together. Making it through all the lab adventures and hanging out afterward was really a pleasure for me. Moreover, he has shown me that you have to believe in yourself to do the impossible. I have greatly appreciated the collaboration with Hugo Flayac, who encouraged and patiently guided me through the debris of the quantum simulations. Besides being a great theoretician, he always kept live interest to the details of our work and created a lively mood during our numerous conversations.

Acknowledgements

I am deeply grateful to Fauzia Jabeen for her bright enthusiasm in work, willingness to discuss, and ability to create such a friendly atmosphere in our group. I really appreciated lively debates with Hadis Abbaspour who shared with me her joy about the quantum optics. I am grateful to Claud ric Ouellet-Plamondon for the unforgettable clean room experience and vivid discussions. A sincere thanks goes to Gw nol  Jacopin for passing his knowledge, his readiness to help with the equipment, and of course for chatting about the forthcoming races. I am grateful to Francesco Manni and Konstantinos Lagoudakis for opening the doors to the world of polaritons and unveiling the secrets of our lab. It was a great pleasure to collaborate with Maxime Richard and look at the dawn over the sea of polaritons with his eyes. I also would like to thank Daniel Oberli and Christophe Galland for passing their experience and having numerous discussions with them.

I warmly thank to all the other members of LOEQ team: Gr gory Sallen, Fran ois Morier-Genoud, Liu Wei, Mahmoud Hezam, Mehran Shahmohammadi. Special thanks goes to my officemates: Gabriele Grosso, St phane Tr baol, Naotomo Takemura, Pierre Busi,  tienne Batori, Morteza Toupchi, and Santiago Tarrago. I really enjoyed being a part of such a great team.

The life of the whole our group would have been absolutely impossible without Claire-Lyse Rouiller. I am much indebted to her for help during my first as well as the later steps in EPFL, and for her encouragement of my advances in French. Many thanks to Nicolas Leiser and the team of the clean room for showing me the way in the world of nanofabrication, and Gilles Grandgean for his outstanding technical support.

The work I have done in the academia would have never been possible without the life outside of it. I wish to thank all my friends for making these years such an enjoyable and memorable time. My deepest gratitude goes to my family, and especially to my parents who gave me their wisdom and constantly support me in all my beginnings. Finally, my most sincere thanks go to Anna for being with me during this wonderful journey.

Albert Adiyatullin

Address: Route du Lac 22, Denges, 1026 Switzerland
Tel: +41 786 24 83 53
E-mail: albert.adiyatullin@epfl.ch
Date of birth: 30 December 1988

Research Experience

- 2013 – 2017 **École Polytechnique Fédérale de Lausanne** (Lausanne, Switzerland)
Doctoral Assistant
- Designed and assembled a novel streak-camera based setup for ultrafast photon correlation measurements.
 - Examined microcavity polariton statistics during their relaxation to a Bose-Einstein condensate.
 - Demonstrated generation of squeezed light from two coupled weakly nonlinear polariton modes.
 - Developed a protocol for chemical etching of ultrathin (6 nm) AlGaAs layers.
- 2011 – 2013 **Lebedev Physical Institute** (Moscow, Russia)
Research Intern
- Examined charge hopping between multiple quantum wells in ZnSe-based light emitters.
 - Evaluated role of high growth temperature on the material diffusion in ZnSe-based quantum wells.
 - Developed a high-power laser diode driver with an intensity stabilization.

Education

- 2013 – 2017 **École Polytechnique Fédérale de Lausanne**
PhD in Physics
- 2010 – 2012 **Moscow Institute of Physics and Technology**
M. Sc. in Applied Mathematics and Physics, GPA 5.0/5.0
- 2006 – 2010 B. Sc. in Applied Mathematics and Physics, GPA 4.8/5.0

Skills

- Experimental:** ultrafast optical spectroscopy, streak-cameras, optical interferometry, light statistics measurements, cryogenics, clean room semiconductor processing
- Software:** MATLAB, Mathematica, LabVIEW, Origin, Solidworks, Eagle CAD
- Teaching:**
- supervision of master student projects
 - academic teaching for bachelor students (lab works and seminars)
 - summer school teaching for intermediate and high school students
 - organizing competitions of high school students in Mathematics and Physics
 - organizing popular scientific events with EPFL Photonics Chapter

- Languages:**
- English (advanced)
 - French (intermediate)
 - German (intermediate)
 - Russian (native)

Publications

A. F. Adiyatullin, M. D. Anderson, H. Flayac, M. T. Portella-Oberli, F. Jabeen, C. Ouellet-Plamondon, G. Sallen, and B. Deveaud *“Periodic squeezing in a polariton Josephson junction”*, accepted to Nature Communications (preprint available on arXiv:1612:06906).

A. F. Adiyatullin, M. D. Anderson, P. V. Busi, H. Abbaspour, R. André, M. T. Portella-Oberli, and B. Deveaud *“Temporally resolved second-order photon correlations of exciton-polariton Bose-Einstein condensate formation”*, Appl. Phys. Lett. **107**, 221107 (2015).

S. V. Shevtsov, **A. F. Adiyatullin**, D. E. Sviridov, V. I. Kozlovsky, P. I. Kuznetsov, S. N. Nikolaev, and V. S. Krivobok *“Photoinduced charge redistribution and its influence on excitonic states in Zn(Cd)Se/ZnMgSSe/GaAs quantum-well heterostructures”*, Phys. Solid State **56**, 801 (2014).

A. F. Adiyatullin, S. V. Shevtsov, D. E. Sviridov, V. I. Kozlovsky, A. A. Pruchkina, P. I. Kuznetsov and V. S. Krivobok *“Effects of photoinduced charge redistribution on excitonic states in Zn(Cd)Se/ZnMgSSe quantum wells”*, J. Appl. Phys. **114**, 163524 (2013).

A. F. Adiyatullin, V. V. Belykh, V. I. Kozlovsky, V. S. Krivobok, V. P. Martovitsky, S. N. Nikolaev *“Effect of heteroboundary spreading on the properties of exciton states in Zn(Cd)Se/ZnMgSSe quantum wells”*, J. Exp. Theor. Phys. **115**, 885 (2012).

Conferences

- 2017 **18th International Conference on Physics of Light-Matter Coupling in Nanostructures (PLMCN-18)**
Oral presentation *“Periodic squeezing in a polariton Josephson junction”*.
Conference on Lasers and Electro-Optics/Europe and European Quantum Electronics Conference (CLEO/Europe – EQEC 2017)
Poster *“Periodic squeezing in a polariton Josephson junction”*.
- 2016 **8th International Conference on Spontaneous Coherence in Excitonic Systems (ICSCE-8)**
Oral presentation *“Second-order photon correlation dynamics in coupled polariton BECs”*.
- 2015 **14th International Conference on Optics of Excitons in Confined Systems (OECS-14)**
Oral presentation *“Dynamics of photon correlations in exciton-polariton BEC”*.
- 2013 **20th International Conference on Electronic Properties of Two-Dimensional Systems and 16th International Conference on Modulated Semiconductor Structures (EP2DS-20/MSS-16)**
Poster *“Properties of excitonic states in MOCVD-grown Zn(Cd)Se/ZnMgSSe quantum wells with spreaded heterointerfaces”*.

Awards

- 2012 **Award of Foundation of Assistance to Small Innovative Enterprises**
for a protocol of realization of strong light-matter coupling in ZnSe-based microcavities.
- 2011 **V. L. Ginzburg Award on the Lebedev Physical Institute senior student contest**
for the work on the spreading of heterointerfaces in ZnSe-based quantum wells.

